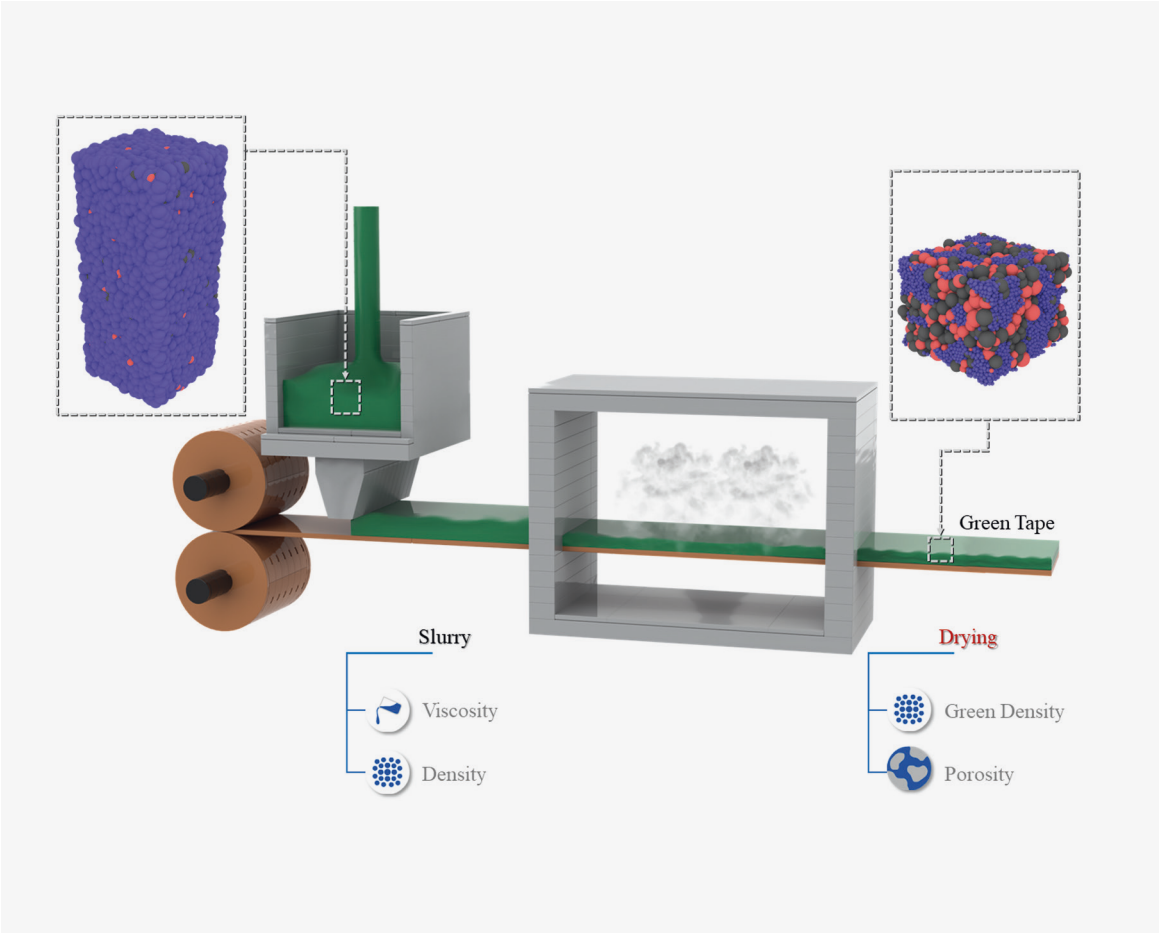

Machine Learning Guidance of Manufacturing Process of Solid Oxide Cells

Tan LE DINH

Energie & Umwelt / Energy & Environment
Band / Volume 704
ISBN 978-3-95806-904-6

Mitglied der Helmholtz-Gemeinschaft

JÜLICH
Forschungszentrum

Schriften des Forschungszentrums Jülich
Reihe Energie & Umwelt / Energy & Environment Band / Volume 704

Forschungszentrum Jülich GmbH
Institute of Energy Materials and Devices (IMD)
Werkstoffsynthese und Herstellungsverfahren (IMD-2)

Machine Learning Guidance of Manufacturing Process of Solid Oxide Cells

Tan LE DINH

Schriften des Forschungszentrums Jülich
Reihe Energie & Umwelt / Energy & Environment Band / Volume 704

ISSN 1866-1793 ISBN 978-3-95806-904-6

Bibliografische Information der Deutschen Nationalbibliothek.
Die Deutsche Nationalbibliothek verzeichnet diese Publikation in der
Deutschen Nationalbibliografie; detaillierte Bibliografische Daten
sind im Internet über http://dnb.d-nb.de abrufbar.

Herausgeber und Vertrieb:	Forschungszentrum Jülich GmbH Zentralbibliothek, Verlag 52425 Jülich Tel.: +49 2461 61-5368 Fax: +49 2461 61-6103 zb-publikation@fz-juelich.de www.fz-juelich.de/zb
Umschlaggestaltung:	Grafische Medien, Forschungszentrum Jülich GmbH
Druck:	Grafische Medien, Forschungszentrum Jülich GmbH
Copyright:	Forschungszentrum Jülich 2026

Schriften des Forschungszentrums Jülich
Reihe Energie & Umwelt / Energy & Environment, Band / Volume 704

(Diss. Université de Picardie Jules Verne, 2026)

ISSN 1866-1793
ISBN 978-3-95806-904-6

Vollständig frei verfügbar über das Publikationsportal des Forschungszentrums Jülich (JuSER)
unter www.fz-juelich.de/zb/openaccess.

To my parents, whose endless
love and support encouraged me
throughout this journey.

Abstract

Solid Oxide Cells (SOCs) are promising energy conversion devices with applications in both electricity generation and chemical fuel production. Fuel Electrode-Supported Cells (FESCs) particularly offer a robust architecture, but their performance and reliability are heavily dependent on the manufacturing process of a porous substrate material. Traditional manufacturing parameter optimisation primarily relies on trial-and-error experimental methods, which are resource-intensive, time-consuming, and difficult to scale for industrial production.

This PhD dissertation addresses these challenges by combining physics-based and data-driven modelling to link manufacturing parameters, microstructure, and physical properties of the fuel-electrode substrate. These novel approaches are developed to investigate how the manufacturing parameters affect the substrate microstructure, offering the digital tools to optimise the fabrication process of SOCs. Specifically, a coarse-grained physics-based modelling framework was developed to simulate the slurry and dried microstructures of fuel-electrode substrates for the tape casting and drying stages of fuel cell substrate materials. The microstructures generated by this model provide digital representations of the coarse substrate material, which can be used as input for multi-scale simulation methods.

Concurrently, the thesis focuses on applying Machine Learning (ML) techniques to optimise SOC manufacturing processes. By integrating advanced data collection through electronic laboratory notebooks and on-site characterisation, ML models have been trained to predict the substrate properties at each manufacturing stage. This data-driven approach helps to identify fundamental relationships between key manufacturing parameters and substrate properties, enabling the optimisation of the manufacturing routes for achieving target characteristics of the fuel-electrode substrate.

These physics-based and data-driven strategies form a complementary framework, bridging experimental production and predictive simulation. The contribution of this research lies in providing novel modelling tools, integrating experimental, numerical and data-driven methods, and supporting the systematic, reproducible, and energy-efficient scaling up of SOC production.

Résumé

Les Cellules à Oxyde Solide (SOC) constituent des dispositifs prometteurs de conversion d'énergie, avec des applications à la fois dans la production d'électricité et la génération de carburants chimiques. Les Cellules à Électrode de Combustible Supportée (FESC) offrent une architecture particulièrement robuste, mais leurs performances et leur fiabilité dépendent fortement du procédé de fabrication du matériau poreux constituant le substrat. L'optimisation traditionnelle des paramètres de fabrication repose principalement sur des méthodes expérimentales empiriques, lesquelles sont coûteuses en ressources, chronophages et difficiles à adapter à une production industrielle.

Cette thèse de doctorat s'attaque à ces défis en combinant des modèles fondés sur la physique et fondés sur les données, afin d'établir le lien entre les paramètres de fabrication, la microstructure et les propriétés physiques du substrat de l'électrode à combustible. Ces approches novatrices ont été développées pour étudier l'influence des paramètres de fabrication sur la microstructure du substrat, et proposer des outils numériques destinés à optimiser le procédé de fabrication des SOC. Plus précisément, un cadre de modélisation mésoscopique fondé sur la physique a été élaboré pour simuler les microstructures du lisier et du substrat séché des électrodes à combustible durant les étapes de coulée sur bande et de séchage. Les microstructures générées par ce modèle offrent une représentation numérique du matériau de substrat grossier, pouvant servir d'entrée à des méthodes de simulation multi-échelles.

Parallèlement, le thèse se concentre sur l'application des techniques de Machine Learning (ML) pour optimiser les procédés de fabrication des SOC. En intégrant une collecte de données avancée via des carnets de laboratoire électroniques et des caractérisations in situ, des modèles de ML ont été entraînés pour prédire les propriétés du substrat à chaque étape de la fabrication. Cette approche fondée sur les données permet d'identifier les relations fondamentales entre les principaux paramètres de fabrication et les propriétés du substrat, facilitant ainsi l'optimisation des itinéraires de fabrication pour atteindre les caractéristiques cibles du substrat de l'électrode à combustible.

Ces approches fondées sur la physique et sur les données forment un cadre complémentaire, reliant la production expérimentale et la simulation prédictive. La contribution de cette recherche réside dans le développement d'outils de modélisation novateurs, intégrant des méthodes expérimentales, numériques et axées sur les données, afin de soutenir une montée en échelle systématique, reproductible et écoénergétique de la production des SOC.

Zusammenfassung

Festoxidzellen (SOCs) sind vielversprechende Energieumwandler, die sowohl in der Stromerzeugung als auch in der chemischen Brennstoffproduktion eingesetzt werden können. Brennstoffelektroden-gestützte Zellen (FESCs) bieten insbesondere eine robuste Architektur, aber ihre Leistung und Zuverlässigkeit hängen stark vom Herstellungsprozess eines porösen Substratmaterials ab. Die traditionelle Optimierung der Herstellungsparameter stützt sich in erster Linie auf experimentelle Trial-and-Error-Methoden, die ressourcenintensiv, zeitaufwändig und für die industrielle Produktion schwer skalierbar sind.

Diese Doktorarbeit befasst sich mit diesen Herausforderungen, indem sie physikalisch basierte und datengesteuerte Modellierungen kombiniert, um Fertigungsparameter, Mikrostruktur und physikalische Eigenschaften des Brennstoffelektrodensubstrats miteinander zu verknüpfen. Diese neuartigen Ansätze wurden entwickelt, um zu untersuchen, wie sich die Fertigungsparameter auf die Mikrostruktur des Substrats auswirken, und um digitale Werkzeuge zur Optimierung des Herstellungsprozesses von SOCs bereitzustellen. Insbesondere wurde ein grobkörniges, physikalisch basierter Modellierungsrahmen entwickelt, um die Schlicker- und getrockneten Mikrostrukturen von Brennstoffzellen-Elektrodensubstraten für die Bandguss- und Trocknungsphasen von Brennstoffzellen-Substratmaterialien zu simulieren. Die durch dieses Modell erzeugten Mikrostrukturen liefern digitale Darstellungen des groben Substratmaterials, die als Input für multiskalige Simulationsmethoden verwendet werden können.

Gleichzeitig konzentriert sich die Dissertation auf die Anwendung von Techniken des maschinellen Lernens (ML) zur Optimierung von SOC-Fertigungsprozessen. Durch die Integration fortschrittlicher Datenerfassung mittels elektronischer Laborbücher und Charakterisierung vor Ort wurden ML-Modelle trainiert, um die Substrateigenschaften in jeder Fertigungsphase vorherzusagen. Dieser datengesteuerte Ansatz hilft dabei, grundlegende Zusammenhänge zwischen wichtigen Fertigungsparametern und Substrateigenschaften zu identifizieren, wodurch die Fertigungswege optimiert werden können, um die Zielcharakteristika des Brennstoffelektrodensubstrats zu erreichen.

Diese physikalisch basierten und datengesteuerten Strategien bilden einen komplementären Rahmen, der eine Brücke zwischen experimenteller Produktion und prädiktiver Simulation schlägt. Der Beitrag dieser Forschung liegt in der Bereitstellung neuartiger Modellierungswerkzeuge, der Integration experimenteller, numerischer und datengesteuerter Methoden sowie der Unterstützung einer systematischen, reproduzierbaren und energieeffizienten Skalierung der SOC-Produktion.

Acknowledgements

I wish to express my sincere gratitude to the Université de Picardie Jules Verne (UPJV), Laboratoire de Réactivité et de Chimie des Solides (LRCS), and the Forschungszentrum Jülich GmbH, Institute of Energy Materials and Devices (IMD) – Materials Synthesis and Processing (IMD-2), for providing me with the opportunity and excellent research facilities that made this PhD research possible. I also gratefully acknowledge the financial support from Région Hauts-de-France (France) and Bundesministerium für Wirtschaft und Energie – Project No. 03EI3085A, ML4SOC (Germany).

First and foremost, I would like to express my deepest gratitude to my supervisors, Prof. Dr. Alejandro A. Franco at LRCS (France) and Prof. Dr. Olivier Guillon at IMD-2 (Germany), for their excellent supervision, invaluable guidance, inspiring scientific vision, and unlimited support during my PhD journey. Their expertise and encouragement have been essential to the success of this thesis and to my personal and professional development. I am especially thankful for their trust and for giving me the opportunity to work within such dynamic and interdisciplinary research teams. I have learned not only how to conduct rigorous and impactful research but also how to approach science with openness and creativity.

I am also profoundly grateful to Priv.-Doz. Dr. Hartmut Schlenz, my advisor at IMD-2, for his close supervision, constant guidance, insightful discussions, and unwavering support throughout my PhD journey. His patience, scientific insight, attention to detail, and constructive advice have greatly shaped my research and made this journey truly rewarding. I am deeply thankful for the countless hours he devoted to guiding me and for his steady encouragement during challenging times. Vielen Dank!

I would like to extend my heartfelt thanks to Hon.-Prof. Dr.-Ing. Norbert H. Menzler for his fruitful collaboration, valuable discussions, and the opportunity to publish our work together. His deep knowledge, practical experience and kind guidance have been of great benefit to the quality and depth of my work.

My warmest appreciation goes to all my colleagues and friends at LRCS and IMD-2 for their support, inspiring conversations, and the enjoyable working atmosphere. I would like to acknowledge the technical and administrative staff of both LRCS and IMD-2 for their assistance and professionalism, which greatly facilitated my research. I am also thankful to everyone who contributed, directly or indirectly, to this work and who made my time in France and Germany truly rewarding.

Finally, I owe my deepest love and gratitude to my parents and my two younger brothers for their endless support, patience, encouragement and love. Their constant belief in me has been my source of motivation and strength during this entire journey.

Contents

List of Figures

List of Tables

List of Abbreviations

1D	One-dimensional
3D	Three-dimensional
AI	Artificial Intelligence
BDPD	Binder Dispersant Plasticiser Domain
CGMD	Coarse-Grained Molecular Dynamics
CNN	Convolutional Neural Network
CTE	Coefficient of Thermal Expansion
DEM	Discrete Element Method
DL	Deep Learning
ELN	Electronic Laboratory Notebook
ESC	Electrolyte-Supported Cell
FESC	Fuel Electrode-Supported Cell
FF	Force Field
GH	Granular Hertzian
LJ	Lennard-Jones
ML	Machine Learning
MSC	Metal-Supported Cell
PtX	Power-to-X
PSD	Particle Size Distribution
RDF	Radial Distribution Function
SC	Solid Content
SOC	Solid Oxide Cell
SOEC	Solid Oxide Electrolysis Cell
SOFC	Solid Oxide Fuel Cell

1 Introduction

Global energy systems are undergoing a fundamental shift toward sustainable energy systems, driven by the urgency to mitigate climate change, prevent environmental degradation, and ensure long-term energy security [1, 2]. Figure 1.1 shows the rapidly growing demand for energy resources and the excessive consumption of fossil fuels such as oil, coal, and natural gas in recent decades. This has driven alarming energy and environmental issues, including resource depletion, global warming, and ecological degradation (e.g., ocean acidification and air pollution) [3]. Within the renewable energy landscape, wind and solar power hold a significant share of the market because of their abundance and zero greenhouse gas emissions. In the European Union, expanding the contribution of these clean energy sources is regarded as a cornerstone for meeting the target of reducing net greenhouse gas emissions by at least 55% by 2030 and achieving climate neutrality by 2050 [4]. However, the integration of solar and wind power into the energy grid still faces ongoing problems. Since the generation of solar and wind power varies with daily cycles and weather conditions, the energy production from the wind/solar power plant is typically unstable and variable [5]. To maintain grid stability and reliability, a substantial fraction of generated renewable power is curtailed due to the inherent imbalance between energy generation and consumption [6, 7, 8]. This has led to growing interest in strategies for capturing and converting surplus energy. Power-to-X (PtX) technology is a flexible energy conversion and storage solution in this context. The PtX (X can refer to chemical, fuel, hydrogen, food, heat, etc.) provides a pathway to convert surplus renewable electricity into storable energy carriers, thereby maintaining a stable renewable energy supply. Hydrogen, a versatile and abundant energy carrier, is regarded as not only a foundation element of PtX applications but also a major step in phasing out fossil fuels. Hydrogen technologies particularly have a pivotal role to play in the transition from fossil fuels to renewable energy, essential for realising net-zero and sustainable development plans [9, 10].

Solid Oxide Cells (SOCs) are a key technology for flexible energy conversion, operating as either Solid Oxide Fuel Cells (SOFCs) to produce electricity from hydrogen (or

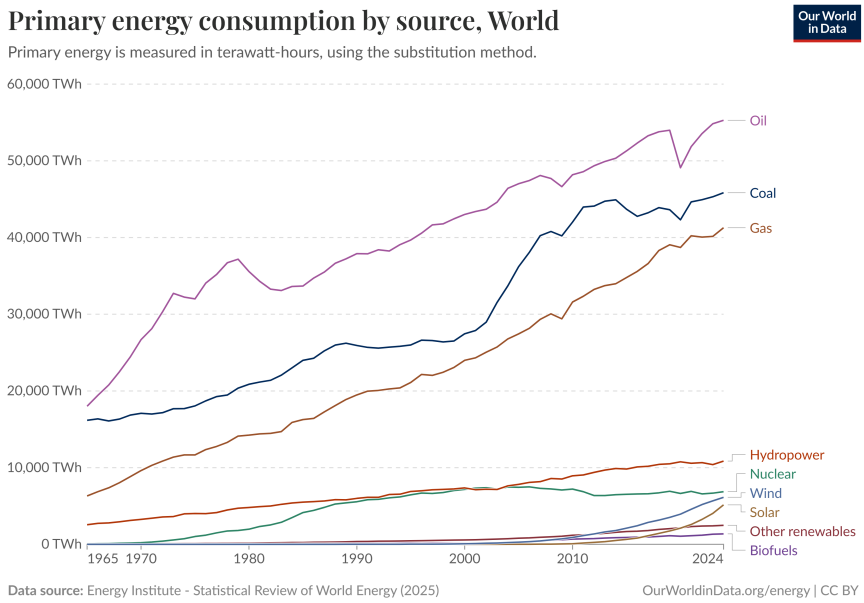

Figure 1.1. Global primary energy consumption by source from 1965 to 2024. Data is measured in terawatt-hours (TWh). Source: Our World in Data; Energy Institute - Statistical Review of World Energy (2025) [11].

other alternative fuels) or Solid Oxide Electrolysis Cells (SOECs) to convert electrical energy into chemical fuel within the PtX schemes. In particular, Fuel Electrode-Supported Cells (FESCs) are widely studied as a promising configuration. By utilising a mechanically robust fuel electrode as the supporting layer, FESC design can achieve a thinner electrolyte thickness [12], thus lowering ohmic losses while maintaining high structural stability. The properties of a fuel-electrode substrate, namely density, porosity, mechanical strength and microstructural homogeneity are crucial for FESCs to operate properly. These properties critically depend upon the manufacturing process.

The production of fuel-electrode substrates is essentially a multi-stage process, typically involving tape casting and drying, sintering, and reduction steps. These stages are highly interdependent, with the output of one directly shaping the next step. Within each stage itself, process conditions have impacts on the properties as well as the microstructure evolution of the substrates. For instance, slurry formulation and tape-casting parameters govern thickness uniformity and density of the tape after drying, while sintering determines pore distribution and mechanical stability. Conventionally, optimising these manufacturing parameters relies heavily upon empirical trial-and-error approaches. This is resource-intensive and time-consuming, thus challenging to scale from laboratory to industrial production. To address these

challenges, physics-based and data-driven machine learning surrogate approaches are essential to efficiently predict material properties, enabling fabrication optimisation of the fuel-electrode substrates.

SOC modelling is inherently complex owing to the multiscale interaction between the physical and chemical processes. The modelling complexity depends upon the targeted application, requiring model parameter calibration to fit each specific simulated context. Physics-based models such as finite element method, finite volume method, and discontinuous Galerkin method have been widely applied to study system-level behaviour, allowing the prediction of key indicators, including thermal stresses, power output, and mechanical stability under operational conditions [13]. Despite their strengths, such models rely on simplifying assumptions, idealised conditions, and material parameters that are difficult to measure or uncertain at the microstructural level [14]. Furthermore, the physics-based models are computationally demanding, particularly when extended to large-scale or multiphysics systems [15, 16].

Alternatively, Machine Learning (ML) is a subset of Artificial Intelligence (AI) that empowers complex systems to learn from the process data in order to make predictions without being explicitly programmed. Leveraging techniques such as Deep Learning (DL), the data-driven approaches have become powerful tools to reshape multiple industrial sectors worldwide. In the context of SOC manufacturing, data-driven ML can quickly and accurately predict material properties of target component layers without understanding detailed physical/chemical laws by learning from relevant experimental process datasets. This allows manufacturing systems of SOC components to automatically learn and improve from experience. Although data-driven models are often constrained by data quality and availability, and lack the interpretability required for deriving mechanistic insights [17, 18, 19], they are a significant complement to physics-based models. These complementary strengths and weaknesses have motivated growing interest in hybrid frameworks that combine physics-based modelling with ML modelling [20, 21, 22, 23].

Within the ARTISTIC research initiative and linked projects, led by Prof. Dr. Alejandro A. Franco at Université de Picardie Jules Verne, a multiscale modelling platform encompassing physics-based simulation, AI and pilot-line manufacturing experiments has been developed to link the fabrication process of the lithium-ion, sodium-ion and solid-state battery electrode, electrode microstructure and electrochemical performance [24, 25, 26]. Although originally conceived for the battery domain, the methodologies and digital tools developed within the ARTISTIC project are highly adaptable and provide a transferable framework for other energy technologies, including SOCs. The application of these approaches to SOC manufacturing can provide deeper insight into the interplay between materials, processes, and performance, thereby guiding optimisation in a more systematic and predictive manner.

Building upon data-driven ML approaches, the ML4SOC project, funded by the Federal Ministry of Economic Affairs and Energy of Germany, has been launched under Prof. Dr. Olivier Guillon at Forschungszentrum Jülich GmbH (FZJ), Institute of Energy Materials and Devices (IMD) – Materials Synthesis and Processing (IMD-2). This project is dedicated to applying ML to the design, optimisation, and predictive

modelling of SOCs. Specifically, the ML4SOC project targets the integration of ML into the manufacturing of SOCs by means of tape casting, with the substrate of the FESCs as the first hands-on component. By combining advanced experimental data acquisition using an Electronic Laboratory Notebook (ELN) and *in-situ* characterisation, the ML4SOC project aims to establish robust ML models capable of identifying optimal process parameters, reducing overall energy consumption (especially during either drying or sintering), and supporting reproducibility in large-scale production of SOC technologies.

The present dissertation is situated at the intersection of the ARTISTIC research initiative and its linked projects, as well as ML4SOC project in collaboration between UPJV (France) and IMD-2, FZJ (Germany). While the ARTISTIC framework adaptation to SOC manufacturing provides the conceptual and computational approach for linking manufacturing and the dried microstructure of the substrate after tape casting and drying by coupling physics-based modelling and ML/DL, the ML4SOC project offers a comprehensive data-based approach using a fully experimental dataset to build ML modelling for SOC manufacturing from tape casting and drying to the sintering and reduction stage. The approaches in these two projects complement each other, enabling a deeper understanding of the FESC substrate production. By combining these complementary approaches, the main goal of this thesis is to bridge experimental observations, particle packing of the substrate microstructure after drying, and predictive modelling, ultimately contributing to the scalable and reproducible fabrication of SOC materials. There are two primary aspects to the research objective of this work:

- Develop coarse-grained physics-based modelling, within the ARTISTIC framework, for the tape casting and drying of fuel-electrode supports using a Discrete Element Method (DEM). Unlike stochastic microstructure generation, the DEM approach accounts for particle-scale physical interactions, yielding microstructures with direct physical relevance. Thus, this model provides a digital representation of the green microstructure that can serve as meaningful inputs for subsequent continuous models (e.g., phase-field) instead of only using stochastic microstructures as inputs.

- Leverage ML to exploit experimental datasets, within the ML4SOC project, to capture complex relationships between manufacturing parameters (including those difficult to investigate by using physics-based models, such as humidity or exhaust air volume flow rate, among others) and substrate properties across tape casting and drying, sintering, and reduction stages. This enables us to identify optimal manufacturing parameters from experimental datasets, reducing reliance on empirical trial-and-error.

The following chapters outline the studies conducted in this thesis. Chapter 2 provides the fundamental background on SOCs, including operating principles, materials, designs and manufacturing. Chapter 3 presents coarse-grained physics-based modelling for the tape casting and drying of the fuel-electrode substrate in FESCs. Chapter 4 introduces a hybrid modelling framework by integrating DL and DEM to

accelerate slurry simulation in the tape casting of the fuel-electrode substrate. Chapter 5 discusses the data-driven ML approach to predict the physical properties of the substrate throughout various fabrication stages, encompassing tape casting and drying, sintering, and reduction stages. Finally, Chapter 6 summarises the overall conclusions of the dissertation and gives an outlook.

2

Fundamental aspects of solid oxide cells: From materials to manufacturing

This chapter is devoted to a brief introduction of solid oxide cells. It introduces their operating principles, the materials typically used for each functional layer, common design configurations, and the fabrication route of fuel-electrode-supported cells. This overview establishes a basis for understanding SOC technology and its underlying scientific and engineering aspects.

2.1 Solid Oxide Cells

Solid Oxide Cells (SOCs) are electrochemical energy conversion devices capable of operating in two distinct modes within a single unit. In fuel cell mode (SOFCs), SOCs directly convert the chemical energy of fuels such as hydrogen, methane, or biogas into electricity and heat through an electrochemical reaction between hydrogen and oxygen, resulting in the formation of water. This fundamental reaction, commonly known as the Knallgas reaction, is highly exothermic and central to energy conversion in SOFCs. Conversely, in electrolyser mode (SOECs), SOCs function in reverse, producing hydrogen and oxygen by splitting water. Depending upon the electrolyte material, SOCs typically operate at high temperatures ranging from $650°C$ to $900°C$ [27, 28, 29, 30], and at intermediate temperatures of $\sim 400°C$ to $600°C$ for proton-conducting electrolytes [29, 30, 31, 32]. In this thesis, I focus exclusively on oxygen-ion conducting SOCs, which represent the conventional design for high-temperature operation and are most relevant to current manufacturing approaches. The fundamental working principles of solid oxide cells operating in fuel cell mode and electrolysis mode are illustrated in Figure 2.1. Figure 2.1(a) shows the operation of the SOFC where chemical

energy is converted into electricity, while Figure 2.1(b) depicts the SOEC process, which uses electrical energy to produce hydrogen and oxygen through water splitting.

The SOC generally consists of a dense solid-state oxygen-ion-conducting electrolyte sandwiched between two porous electrodes: a fuel electrode (anode) and an air electrode (cathode). Regarding SOFCs, the electrochemical oxidation of fuel gas, including primarily hydrogen, but potentially also carbon monoxide, methane, etc., occurs at the fuel electrode in the presence of oxygen ions transported through the electrolyte[1] from the air electrode, forming water (H_2O) and possibly Carbon dioxide (CO_2). The liberated electrons pass via an external circuit to reach the air electrode where they reduce oxygen gas to oxide ions under the effect of the air electrode material catalyst. The movement of the electron flowing over the external circuit produces electrical energy.

The half-reaction happening at fuel electrode is written as

$$\mathrm{H_2 + O^{2-} \longrightarrow H_2O + 2\,e^-} \tag{2.1}$$

The half-reaction at the air electrode is expressed as

$$\mathrm{\frac{1}{2}\,O_2 + 2\,e^- \longrightarrow O^{2-}} \tag{2.2}$$

Hence, the overall electrochemical reaction obtained by combining the half-reactions at both electrodes is given by

$$\mathrm{H_2 + \frac{1}{2}\,O_2 \longrightarrow H_2O} \tag{2.3}$$

In the case of using biogas or methane as the fuel gas, reforming reactions generate H2 and CO, which subsequently undergo the electrochemical half-reactions at the fuel electrode as follows: In the case of the use of biogas or methane as the fuel gas, the half-reaction at the fuel electrode is presented as follows:

$$\mathrm{CH_4 + 4\,O^{2-} \longrightarrow CO_2 + 2\,H_2O + 8\,e^-} \tag{2.4}$$
$$\mathrm{CH_4 + H_2O \longrightarrow CO + 3\,H_2} \tag{2.5}$$
$$\mathrm{CO + O^{2-} \longrightarrow CO_2 + 2\,e^-} \tag{2.6}$$
$$\mathrm{H_2 + O^{2-} \longrightarrow H_2O + 2\,e^-} \tag{2.7}$$

The overall electrochemical reaction for methane (or methane-rich biogas) can be represented as

$$\mathrm{CH_4 + 2\,O_2 \longrightarrow CO_2 + 2\,H_2O} \tag{2.8}$$

[1]Due to the higher oxygen partial pressure at the air electrode side, the O^{2-} ions will transport through the electrolyte and reach the fuel electrode, once the external circuit is closed. For hydrocarbon fuels such as methane, reforming reactions typically generate H2 and CO, which subsequently undergo electrochemical oxidation at the fuel electrode.

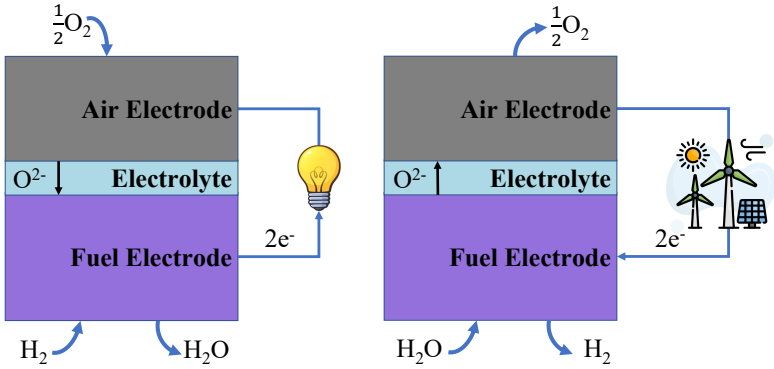

(a) *Solid oxide fuel cells* **(b)** *Solid oxide electrolysis cells*

Figure 2.1. Schematic diagram of (a) Solid oxide fuel cells and (b) Solid oxide electrolysis cells based upon an oxygen ion conductor using H_2 as fuel gas.

During SOEC operation, water molecules are reduced at the fuel electrode (cathode) by incoming electrons to form hydrogen gas and oxide ions. This electrochemical reaction is expressed as

$$H_2O + 2\,e^- \longrightarrow H_2 + O^{2-} \tag{2.9}$$

The oxide ions are transported through the oxygen-ion conducting electrolyte to the air electrode (anode), where they are oxidised to release oxygen gas and electrons:

$$O^{2-} \longrightarrow \frac{1}{2}\,O_2 + 2\,e^- \tag{2.10}$$

Thus, the overall electrolysis reaction can be summarised as follows:

$$H_2O \longrightarrow H_2 + \frac{1}{2}\,O_2 \tag{2.11}$$

A unit composed of the fuel electrode, the electrolyte, and the air electrode is commonly referred to as a cell. During operation, a single cell typically produces a voltage of less than $1\mathrm{V}$ [33, 34]. This output voltage is relatively low for even the smallest application; for instance, a mobile phone generally requires around $5\mathrm{V}$. Thus, the output voltage from a single cell is not sufficient for practical application. In order to produce the necessary power, multiple cells must be connected either in series to increase the amount of voltage or in parallel to deliver a higher current, depending upon the need. This connection is made using another component known as an interconnect, which links individual cells together to form a stack. In this configuration, the overall voltage increases to a level that is suitable for real-world use. Figure 2.2 shows the arrangement of the fundamental components of a plannar SOC stack. The next section offers a brief overview of the main components of the

SOFC, along with their material requirements, to establish the scientific background and introduce the key concepts relevant to this study.

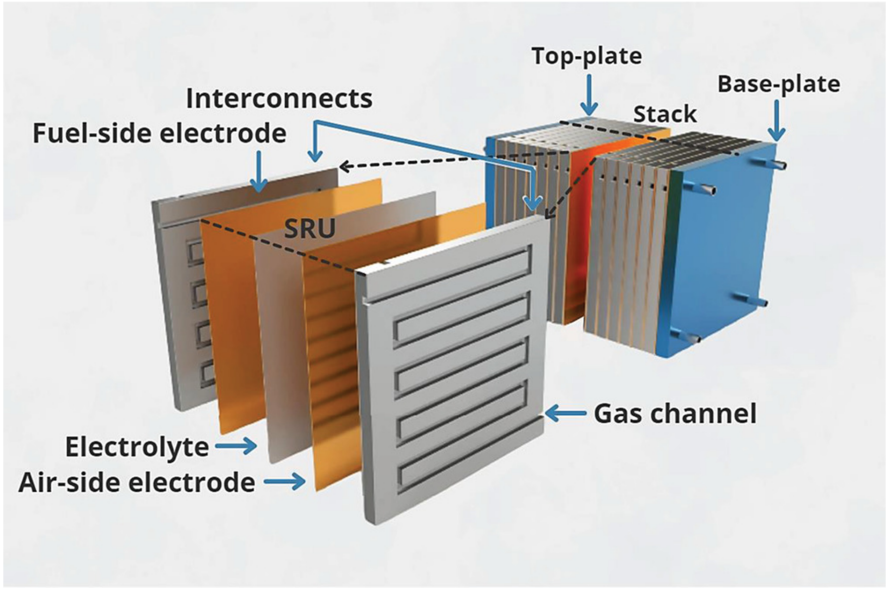

Figure 2.2. Functional core components and configuration of a planar SOC stack (SRU: single repeating unit) [35].

2.2 Materials for SOCs

All components in the SOC device are fabricated from the solid-state materials, typically including alloys, ceramics, or cermets[2]. It is worth mentioning that the materials used for each component of the SOC must be compatible with one another in terms of physical, chemical and thermal properties, particularly under the high-temperature conditions at which SOCs operate.

2.2.1 Oxygen-ion-conducting electrolyte

The electrolyte must meet the key requirements, including gas tightness, chemical stability under both reducing and oxidising conditions, high ionic conductivity, and negligible electronic conductivity[3]. Various oxygen ion-conducting ceramics have been

[2]Cermets are composite materials made of ceramic and metal materials, combining the hardness of ceramics with the toughness of metals.

[3]Electrolyte should not demonstrate electron conduction to avoid an internal short circuit in the cell system.

developed for this purpose, such as Yttria-Stabilised Zirconia (YSZ), doped cerium oxide, and doped bismuth oxide [33]. Among these, YSZ is the most commonly used material for the electrolyte in SOCs due to its thermal stability and high ionic conductivity resulting from a high number of oxygen vacancies. In particular, YSZ with 3 or 8 mol% yttria (3YSZ or 8YSZ) is typically used as a thin film in supported cells, illustrating stable performance within the temperature range of 700°C to 900°C [36].

2.2.2 Fuel electrode

On the fuel-side functional layer, water is reduced during electrolysis, whereas hydrogen is oxidised electrochemically in fuel cell operation. Therefore, the fuel-electrode material must be chemically and thermally stable, and exhibit high electronic and ionic conductivity, along with a fine and porous structure for gas diffusion of educts and products [36, 37]. Nickel (Ni) is commonly utilised in almost all commercially available SOC devices as catalytic active phase. Nevertheless, its high Coefficient of Thermal Expansion (CTE) against that of YSZ electrolyte limits its use as a standalone material. To overcome this, Ni is typically combined with YSZ to form a composite. Addition of YSZ into porous Ni not only improves ionic conductivity but also enhances thermal compatibility with the electrolyte [38, 39, 40]. Currently, porous Ni/YSZ cermet is widely used as the fuel electrode material because of its excellent electronic conductivity and catalytic activity. However, the long-term operation of SOCs at high temperatures leads to Ni particle coarsening, reducing the triple-phase boundaries essential for electrochemical reactions [41]. Furthermore, the Ni/YSZ fuel electrode is prone to carbon deposition [42, 43] and sulfur poisoning [44, 45] when using hydrocarbons as fuel gases. This causes significant performance loss. To address these, alternative fuel-electrode materials (e.g. Ni/GDC or Ni/ScYSZ cermets) [45, 46] have been investigated to improve tolerance against carbon deposition and sulfur poisoning, respectively.

2.2.3 Air electrode

The air-electrode material must show a porous microstructure to ensure air diffusion, electronic and ionic conductivity, and chemical stability. Furthermore, the air electrode should also exhibit strong catalytic activity for oxygen splitting during SOFC operation and O^{2-} ion recombination during SOEC operation [47]. For mechanical compatibility, CTE should be adapted to that of adjacent electrolyte layer. The most commonly used materials for the air electrode are ceramic-based mixed ionic and electronic conducting perovskites. These materials share the general perovskite formula ABO_3, with well-known examples including LSCF (La, Sr, Co, Fe) and LSC (La, Sr, Co) [48, 33, 47, 49, 50]. In addition, lanthanum strontium manganite (LSM), which is primarily an electronic conductor, has also been employed in combination with electrolytes such as YSZ for air electrode applications [33].

2.2.4 Interconnects

Interconnects or bipolar plates function both as the electrical connection between adjacent cells and a physical barrier separating the reducing and oxidising atmospheres. To fulfil these requirements, the interconnect material must remain stable in dual environments at high temperatures and provide high electronic conductivity to reduce ohmic losses. Chromium-based ferritic steels, e.g., Crofer 22 APU, are the standard choice due to their favourable conductivity and thermal expansion compatibility with the cell [51]. In order to avoid chromium evaporation, the interconnects are commonly protected with manganese oxide coatings containing dopants such as Co or Fe [52, 53].

2.3 SOC designs

There are three principal SOC designs based upon their mechanical support layer, known as the substrate: Fuel Electrode-Supported Cells (FESCs), Metal-Supported Cells (MSCs), and Electrolyte-Supported Cells (ESCs). In FESCs, the porous substrate is generally fabricated from the same material as the fuel electrode. MSCs use the metallic substrate, while ESCs achieve mechanical stability through the electrolyte itself.

All SOC configurations include the fundamental functional layers, namely the electrolyte, the fuel and air electrodes. In certain cases, diffusion barrier layers are incorporated to prevent the formation of undesired secondary phases, depending upon the selected materials. Planar, tubular and rolled cell geometries have been implemented in various SOC designs [54, 55]. Figure 2.3 provides a schematic overview of the different planar designs.

Both FESCs and MSCs benefit from thin electrolytes, which lower ohmic resistance and thereby enable high power densities, making them particularly attractive for stationary power generation. The resulting lower operating temperatures mitigate materials degradation, extend cell lifetime, reduce corrosion of the ancillary reactant delivery equipment, and lower system costs, enhancing overall system durability and reliability [56, 57, 58, 59, 60, 61]. However, their fabrication poses challenges, particularly with respect to integrating alternative fuel electrode materials, since achieving a gas-tight electrolyte requires sintering at elevated temperatures. The combined structure of substrate, fuel electrode, and electrolyte is commonly referred to as a Half-Cell (HC). During high-temperature sintering of the HC, interdiffusion at interfaces as well as constrained sintering phenomena occur between the different constituent materials.

For ESCs, the electrolyte must be of sufficient thickness to provide mechanical stability but can be processed as a single layer. This characteristic renders ESCs more suitable for investigating novel fuel electrode materials, as they can be fabricated at comparatively lower sintering temperatures. Table 2.1 gives information about the materials and layer thicknesses conventionally used in SOC fabrication.

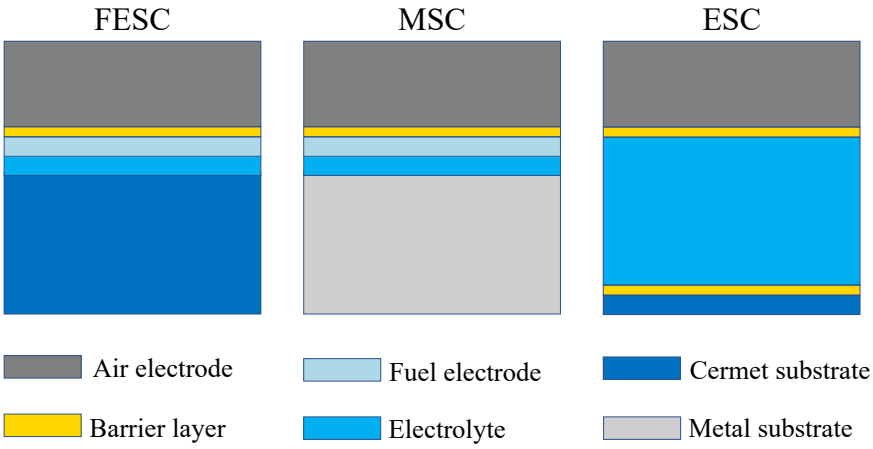

Figure 2.3. A schematic representation showing three prevalent SOC design types (not reflecting actual dimensions).

Table 2.1. Commonly used SOFC materials and layer thicknesses applied by IMD-2.

Layer	Material	Thickness (µm)
Substrate	Ni-$Y_{0.148}Zr_{0.852}O_{1.926}$	~ 300
Fuel electrode	Ni-$Y_{0.148}Zr_{0.852}O_{1.926}$	~ 7
	Ni-$Gd_{0.1}Ce_{0.9}O_{2-\delta}$	~ 15
Electrolyte	$Y_{0.148}Zr_{0.852}O_{1.926}$	~ 10
Barrier layer	$Gd_{0.1}Ce_{0.9}O_{2-\delta}$	~ 6
Steam electrode	$La_{0.58}Sr_{0.4}Co_{0.2}Fe_{0.8}O_{3-\delta}$	~ 30
	$La_{0.58}Sr_{0.4}CoO_{3-\delta}$	

2.4 Production of FESCs

The full cell fabrication of a planar design of FESCs has been developed from the conventional fuel-electrode supported half-cell manufacturing process at Forschungszentrum Jülich GmbH [53, 62]. FESCs typically consist of a thick (250–500 µm) Ni/8YSZ support with a coarse microstructure on the fuel side, a thin ($\sim$ 10 µm), fine-grained Ni/8YSZ fuel electrode, a dense and gas-tight 8YSZ electrolyte of similar thickness, a gadolinium-doped ceria (GDC) barrier layer ($\sim$ 5 µm), and an LSC(F) air electrode with a thickness of about 50 µm. In most cases, the support is produced by tape casting, while the subsequent functional layers are deposited by screen printing. Alternatively,

the support, fuel electrode, and electrolyte may be co-cast in a green-in-green process or cast individually and later laminated [63]. The number of required sintering steps largely depends upon the selected half-cell fabrication route. At a minimum, three sintering steps are necessary (for the half-cell, barrier, and air electrode), but this number may increase to five if the support and fuel electrode are sintered separately [47]. The typical manufacturing procedure of the full cell using tape casting, screen printing, and four sintering steps is illustrated in Figure 2.4.

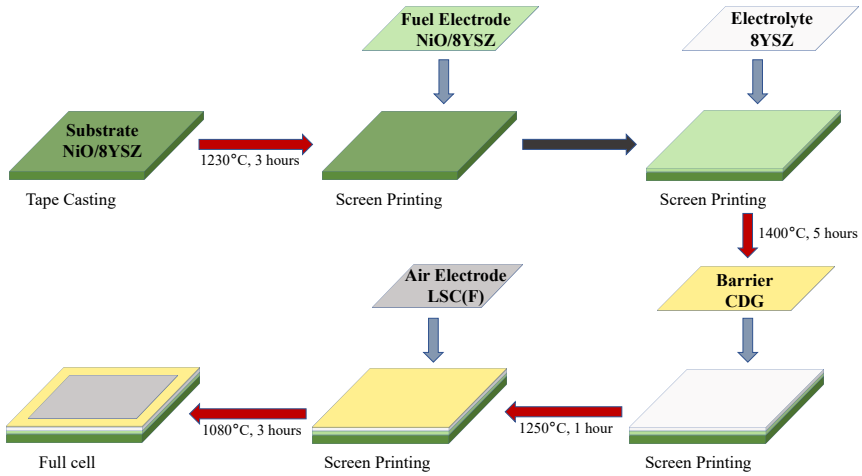

Figure 2.4. Manufacturing process of the fuel-electrode supported SOCs.

3

Coarse-grained physics-based modelling for tape casting of fuel-electrode supports

This chapter presents a modelling framework to simulate the tape casting and drying process of the fuel-electrode supports. To ensure clarity for readers less familiar with modelling approaches, it is useful to distinguish between key concepts of models, modelling, and simulation. A model is a mathematical, physical, or logical representation of a real-world system, phenomenon, or process but not the "real thing" itself. Modelling is the process of producing a model of an original system to analyse solutions and describe the system. Simulation is the use of a model to inspect the behaviour and performance of an actual or hypothetical system. In the simulation, models can be used to examine existing or proposed characteristics of a system [64, 65]. With the rapid advancement of computers, computer simulations have become tremendously powerful tools for investigating phenomena that are too complex to handle analytically [66, 67]. These simulations are software-implemented approximations of mathematical models. A combination of both modelling and simulation is beneficial, particularly starting with modelling to build an understanding of the system, and then using simulation to explore its dynamics and validate the model. It is essential to bear in mind that models, especially those integrating theories and scientific laws, remain approximations of real-world entities. While models frequently show only a partial view of the entire system, they may aid in clarifying specific systematic characteristics. Accordingly, the limitations of a model, including predefined variables and underlying assumptions, must always be considered [68]. As a result, questions regarding the accuracy of the imitation naturally arise, and these are always a concern in computational studies. Addressing these concerns relies on two complementary procedures: verification and validation, which are sometimes both referred to under the umbrella term "validation" [69]. Verification ensures that the computerised

model is correctly implemented, considering both the assumptions and computational procedures, while validation involves comparing simulation results with experimental measurements under defined conditions [70]. In the realme of electrochemical power generation devices, experiments and modelling are frequently combined, ensuring that modelling approaches are suitable for the intended purpose. This conceptual background provides the foundation for the manuscript included in this chapter.

This chapter is the subject of a publication entitled *Coarse-grained physics-based modelling for tape casting of fuel-electrode supports in Solid Oxide Cells*. The original work, contributed by Tan Le-Dinh, Mohammed Alabdali, Franco M. Zanotto, Hartmut Schlenz, Norbert H. Menzler, Olivier Guillon, and Alejandro A. Franco, has been published in the *Journal of Power Sources*, 662 (2026) 238655 (doi:10.1016/j.jpowsour.2025.238655). Minor adaptations have been made to integrate the material coherently into the structure of this thesis.

3.1 Introduction

In FESCs, the fuel-electrode support or substrate must exhibit sufficient mechanical strength of the cell. Moreover, the functions of the support are also electrical connection and gas permeability for educts and products. This results in the major requirements of the fuel-electrode support: high electrical conductivity for electronic conduction and a sufficiently open porous network for gas transport. NiO/YSZ cermets were widely selected as the porous fuel-electrode substrates, as they were reduced to Ni/YSZ cermets in the presence of the fuel during cell start-up, contributing to both sufficient mechanical stability and high electrical conductivity. One of the promising low-cost methods widely used to fabricate the fuel-electrode substrate is the tape-casting method [71, 72]. Tape casting is a well-known technique for the formation of thin-flat-ceramic sheets [73, 74]. The mass production of green tape using this promising process demands casting slurry preparation, including powders, binders, plasticisers, and dispersants [75, 76].

In the tape-casting process, the mechanical and physical attributes of the green tapes are of the utmost importance in the subsequent processing and the final characteristics of the material [77]. In order to produce high-quality green tape, a trial-and-error procedure is often applied to ensure the most stable suspension and achieve the desired tape properties [78, 79, 80]. Nonetheless, this approach is costly, resulting in material wastage, product rejection, and significant time investment. Besides, understanding the evolution of the three-dimensional (3D) microstructure during the tape casting process is critical for investigating key phenomena such as agglomeration, sedimentation, and particle packing, which significantly impact the porosity and mechanical properties of the final support structure. Advanced visualisation techniques, including focused ion beam-scanning electron microscopy (FIB-SEM) [81, 82, 83] and X-ray computed tomography (XCT) [84, 85], are frequently utilised to examine the internal microstructure of the electrode. Despite their utility, these techniques can be time-consuming and pose challenges to fully differentiate between material phases.

Computational modelling has been used to understand the influence of electrode microstructure on electrochemical performance. Although most studies rely on stochastically generated electrode microstructures [86, 87, 88, 89], the manufacturing process plays a pivotal role in determining the morphology and electrochemical performance of the support in SOCs [90, 91, 92]. Thus, accounting for microstructural analysis with manufacturing parameters gives a comprehensive framework, providing deep insights into microstructural evolution.

In the context of the ARTISTIC research initiative [93], numerous physics-based numerical models were reported allowing the prediction of the 3D microstructure of battery electrodes as a function of manufacturing parameters [94, 95, 96, 97]. These models typically employ coarse-grained molecular dynamics or discrete element method (DEM) simulations for each step in the electrode manufacturing process chain. To the best of my knowledge, this powerful computational approach has yet to be considered in the case of SOC devices. In this study, a physics-based DEM approach is applied to model two stages of the tape-casting process of the fuel-electrode supports, namely the slurry phase and its drying. In the slurry phase, the DEM approach models the interaction between NiO, 8YSZ, and domains representing the solvent, the binder, the dispersant and the plasticiser (Binder Dispersant Plasticiser Domain—BDPD) to mimic the properties of the casting slurry. Subsequently, the experimentally validated simulated slurry is used as an input to simulate the drying stage by solvent removal of BDPD.

In this study, a 3D physics-based modelling framework is proposed to simulate the fabrication of fuel-electrode substrates in Ni-cermet planar FESCs. This framework characterises the green tape's microstructural features using the DEM approach, which operates efficiently with limited computational resources. As a proof of concept, the underlying theory and methodology are introduced, followed by an overview of the main results and model outlooks. Finally, the conclusions and perspectives are discussed.

3.2 Materials and methods

3.2.1 Slurry preparation

The most prevalent materials for the support in the state-of-the-art FESCs are Ni-YSZ cermets [98, 99, 100]. The NiO (Green Nickel Oxide) and 8YSZ (8 mol% yttria-stabilized zirconia) powders were utilised to attain a 57:43 NiO:8YSZ volume fraction [101]. The NiO and 8YSZ powder mixture, Ethanol and Methyl ethyl ketone solvents, binders, dispersants, plasticisers and grinding balls were mixed for 10 hours to form the most stable suspension of the slurry. The particle size distributions of both NiO and 8YSZ were not distinguishable in the prepared slurry and determined with d_{10} = 0.35–0.45 µm, d_{50} = 0.5–0.7 µm, and d_{90} = 0.8–1.0 µm. Table 3.1 lists all material components used for the slurry preparation.

Table 3.1. Materials used to prepare the casting slurry.

Material	Role in the slurry	Producer
NiO	Powder	G. Vogler B.V.
8YSZ	Powder	Imerys
Ethanol	Solvent	Merck
Methyl ethyl ketone	Solvent	Merck
Polyvinyl butyral B-98	Binder	Solutia Inc.
Solusolv S-2075	Plasticiser	Solutia Inc.
PEG400	Plasticiser	Merck
BYK 220 S	Dispersant	BYK

3.2.2 Slurry

This subsection delineates the challenges and assumptions inherent to the model, details the procedure for generating the initial structure, and elucidates the physics utilised to simulate the casting slurry, as well as the computational procedures established for characterising the slurry. A major challenge in constructing any 3D geometrical model of the slurry lies in the inconsistency in terms of scale among its chemical elements. Indeed, ceramic powders (e.g. NiO and 8YSZ) used in the slurry mixture are in the micrometre range, while solvents may be considered at the molecular scale level, and organic materials are in the nanoscale. Therefore, geometrical models would require a big simulation box (tens to hundreds of micrometres in length in terms of x, y, and z coordinates) to account for a statistically relevant number of ceramic powder particles, while simultaneously demanding nanoscale or even molecular resolution to capture the smaller slurry components. Such requirements render the simulations prohibitively expensive with current computational resources. Consequently, approximations are essential to seize key characteristics of the slurry microstructure while maintaining the computational cost manageable. In this chapter, a coarsening approach is deployed, as shown graphically in Figure 3.1. More specifically, secondary NiO and 8YSZ particles are explicitly taken into account, while BDPD particles incorporate solvent and organic materials in the slurry phase and represent organic aggregates in the drying phase. The current version of the model would not account for the primary NiO and 8YSZ particles that compose the corresponding secondary particles. Additionally, all particles (e.g. NiO, 8YSZ, and BDPD) are modelled as spheres for simplicity.

The assumptions bring about the following consequences:

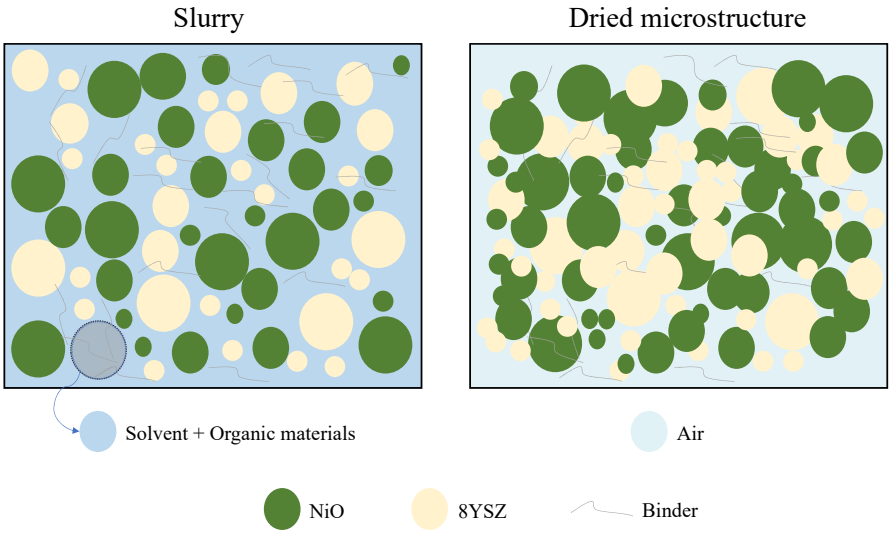

Figure 3.1. Coarsening approach schematic for the fuel-electrode substrate model. The secondary NiO and 8YSZ particles are explicitly described, whereas the BDPD particles account for solvent and organic materials in the slurry phase and for organic materials in the drying phase.

- This model is applicable to powder particles (e.g. NiO and 8YSZ) that can be approximated as spherical.
- In practice, the BDPD phase exhibits strong deviations from spherical morphology because of its high deformability, necessitating proper processing of this phase to fit the model.

The first consequence confines the types of powder particles simulated using this model. In fact, this technique might be improved by using combinations of smaller spherical particles to simulate complex real particle shapes derived from X-ray tomography data. The approach was adopted in the case of lithium-ion batteries and solid-state batteries. However, it showed limitations pertaining to computational cost, especially performing the simulated viscosity was challenging [102, 103]. Another consequence is quite important for model calibration, when examining a balance between computational cost and model fit to experimental values.

Once the model approximations are defined, the manufacturing parameters are required as input for the computational model. The manufacturing parameters are defined as the parameters associated with the experimental process, for instance, the slurry Solid Content (SC) and the Particle Size Distribution (PSD) of the material (e.g., NiO and 8SYZ). The manufacturing parameters are, as per the experimental conditions, assumed to be constant; for example, SC is constant along the simulation.

DEM is a computational simulation technique used to model the dynamic behaviour of complex particulate systems such as powders and granular materials by numerically solving Newton's equation of motion for a collection of particles in a simulated system [104, 105, 106, 107]. The simulation begins with the stochastic generation of initial particle positions within a predefined box, where BDPD particles are enlarged and their density reduced to represent the solvent. The initialisation also includes assigning velocities and forces to each particle. These initial conditions can be based upon experimental data, previous simulations, or theoretical calculations. To describe the interactions between a pair of particles, Force Fields (FFs) are employed. A combination of Lennard-Jones (LJ) and Granular Hertzian (GH) FFs is adopted to resemble the physicochemical characteristics of the casting slurry (Figure 3.2). The LJ FF (LJFF) is used to imitate attractive–repulsive non-bonded interactions between particles, while the GH FF (GHFF) accounts for particle–particle contact mechanics of the system, and thus mimics the real world-behaviour of granular materials such as casting slurry. The forces acting upon each particle are calculated based upon their positions by using these FFs. Newton's second law of motion is then used to update the positions and velocities of the particles in the system. The equations of motion are numerically integrated over a small time step so as to calculate the new positions and velocities of the particles based upon the current positions, velocities, and forces. The integration step is performed until the system reaches equilibrium, with each time advancing the system's state by a small time interval. The smaller the time step, the more accurate the simulation, however, it also increases the computational cost. To avoid particle overlap, all particles are randomly placed within a sufficiently large simulation box at the start. A constant temperature and constant pressure (NPT ensemble) are applied for the slurry-phase simulation at 300 K and 1 bar until the system is equilibrated. In this work, LAMMPS [108, 109], an open-source molecular dynamics programme, is employed for all simulations with Periodic Boundary Conditions (PBCs) in all three directions (x, y, and z-axis). Since the coarsening approach is adopted to model the slurry phase, it has also been referred to as Coarse-Grained Molecular Dynamics (CGMD) in the literature [110]. Nonetheless, it should be emphasised that the present model targets particle-level interactions rather than molecular dynamics. Therefore, while the approach can be described using different terminologies (e.g. CGMD, Particle Dynamics, or DEM), the DEM terminology is consistently used here to emphasise that the simulations address the behaviour of ceramic powder particles at the particle scale.

Another important point to note is that BDPD particles create a continuous medium, in which particles are highly overlapped, that allows this strategy to effectively mimic the behaviour of viscous suspensions, such as the slurry. However, in order to achieve this, the FF parameters must be correctly tuned. Equations (3.1)-(3.3) provide the mathematical descriptions of the LJ and GH FFs.

The LJFF [111, 112] is derived from the LJ potential energy defined as follows:

$$V(r) = 4\epsilon \left[\left(\frac{\sigma}{r} \right)^{12} - \left(\frac{\sigma}{r} \right)^{6} \right] \quad r < r_c, \tag{3.1}$$

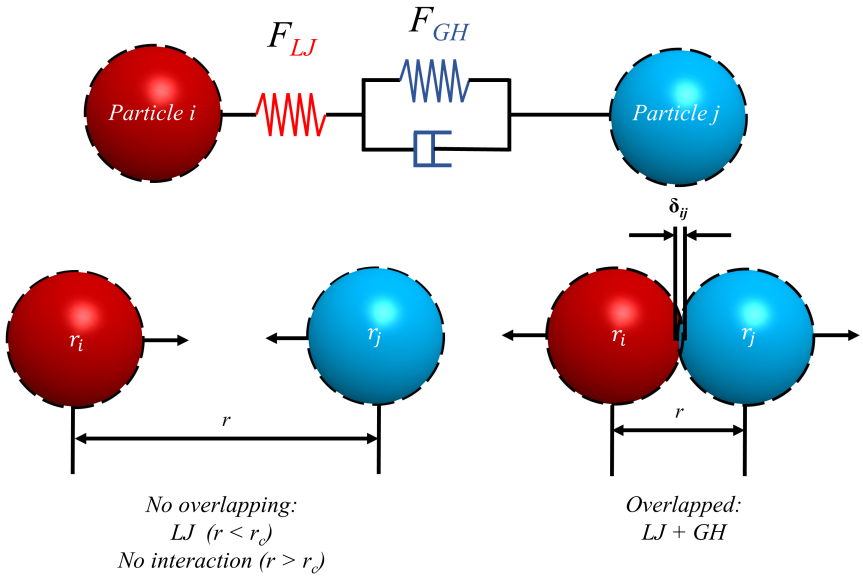

Figure 3.2. FFs working principle based upon LJ and GH interactions between two particles within the simulations.

$$F_{LJ}(r) = -\nabla V(r), \tag{3.2}$$

where ϵ is the well depth that measures the strength of the attraction between the two particles, σ represents the minimum distance to which two nonbonding particles may approach each other since it corresponds to the distance at which the inter-particle potential between the two particles becomes zero, r_c is the cut-off distance at which the particles stop interacting with one another, and r represents the distance between a pair of particles measured from the centre of one particle to the centre of the other particle (Figure 3.3).

The GHFF [114, 115] is defined as

$$F_{GH} = \sqrt{\delta}\sqrt{\frac{R_i R_j}{R_i + R_j}}\left[\left(k_n \delta n_{ij} - m_{\text{eff}}\gamma_n v_n\right) - \left(k_t \Delta s_t + m_{\text{eff}}\gamma_t v_t\right)\right], \tag{3.3}$$

where δ is the overlap distance, R_i and R_j are the radii of two interacting particles, k_n is the normal elastic constant, k_t is the tangential elastic constant, γ_n is the viscoelastic damping constant for normal interaction, γ_t is the viscoelastic damping constant for tangential interaction, v_n and v_t are the relative velocities of two interacting particles in terms of normal and tangential components, respectively. In addition, Δs_t is the tangential displacement vector between a pair of interacting particles, n_{ij} represents

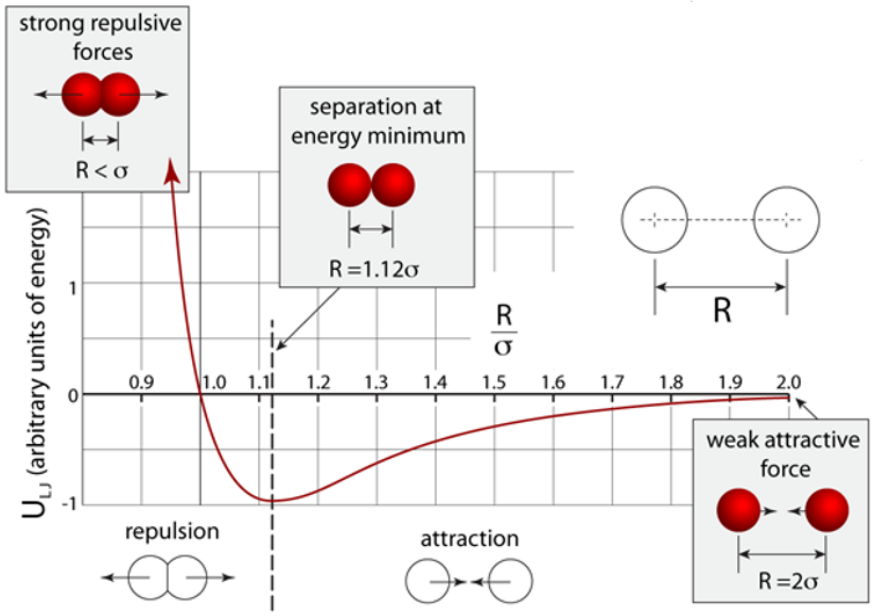

Figure 3.3. The LJ potential describes both the attraction and repulsion between particles [113].

the unit vector along the line linking the centres of the two interacting particles, and m_{eff} is the effective mass of both particles, expressed as

$$m_{\text{eff}} = \frac{m_i m_j}{m_i + m_j}, \tag{3.4}$$

where m_i and m_j are the mass of particle i and particle j, respectively.

It is clearly evident from equation (3.3) that F_{GH} will be equal to 0 for $\delta = 0$ (Figure 3.4). An appropriate proportion of overlap between interacting particles must thus be permitted so as to account for the GHFF. Another important parameter, the coefficient of friction (μ), determined by the highest ratio between the tangential and normal forces, is the last factor required for the simulation [115].

It should be noted that the LJFF in this study is an approximation to describing the interaction between particles, and the LJ was chosen because of its simplicity. Specifically, the LJ was used as an approach to control the distance and interaction forces among different particles. This adjustment of interparticle distances is critical to stabilise the particles in both the slurry and drying phases and to prepare a physically plausible particle packing for the GH contact model, which governs elastic and frictional forces once particles are in contact. By contrast, the GH contact model is directly derived from physical contact mechanics and represents the particle-level

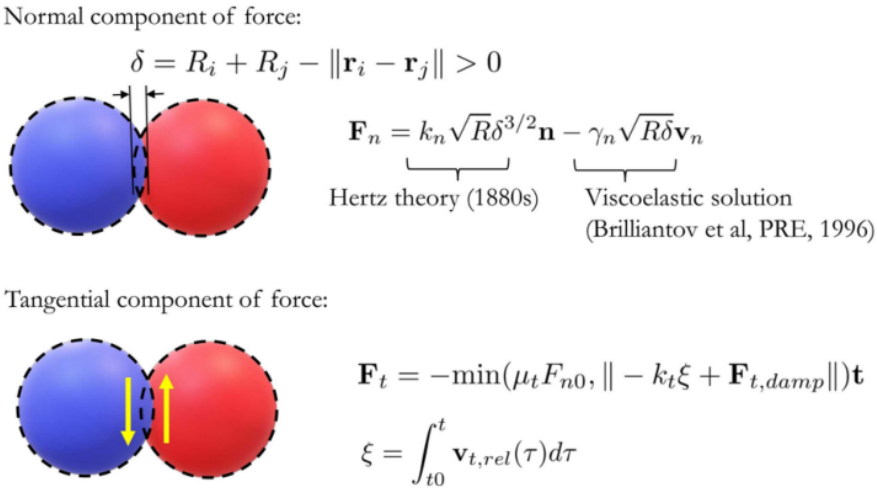

Figure 3.4. Schematic of the applied GH forces [116].

physics, ensuring suspension stability and particle packing after drying that are consistent with experimental observations. Therefore, these two FFs form the coarse-grained description, allowing the model to mimic the experimentally observed suspension behaviour, particle packing, and microstructural features of the fuel-electrode support. While the LJFF provides an effective means to mimic mesoscale cohesive interactions, the GHFF preserves rigorous particle-level physics, enabling the overall DEM framework to be considered physics-based in the coarse-grained modelling sense.

In the simulation, the particles are explicitly considered as distinct material kinds in the system, for example, NiO, 8YSZ, and BDPD, in which the BDPD particle is a type of an effective particle that represents solvents and organic materials in the casting slurry. Thus, the BDPD diameter and its density are also effective parameters that can be adjusted to optimise the FFs.

Figure 3.5 demonstrates not only the initial and final states of the slurry simulation with the particle interactions in compliance with the chosen FFs but also the equilibration of the initial simulation box to prevent overlapping of the particles through increasing the pressure until 1 bar to obtain the equilibrated slurry model. Some variables, such as particle overlap and velocity, are automatically calculated by LAMMPS, while all FF parameters must be calibrated to fit the experimental output descriptors by the operator. Specifically, the slurry phase is validated by comparing the experimental with the simulated density. Additionally, such DEM simulations should also display a calibration of the viscosity in the equilibration of the slurry. In fact, when a shear rate ($\dot{\gamma}$) is applied to the slurry, the slurry undergoes deformation, which gives rise to shear stress (τ). τ is determined by the force required to sustain the deformation divided by the slurry surface area. Viscosity is then defined as the ratio of τ to $\dot{\gamma}$ (Figure

3.6). This set-up closely reflects the experimental configuration used to measure slurry viscosity, making it well-suited for comparing experimental and simulated results.

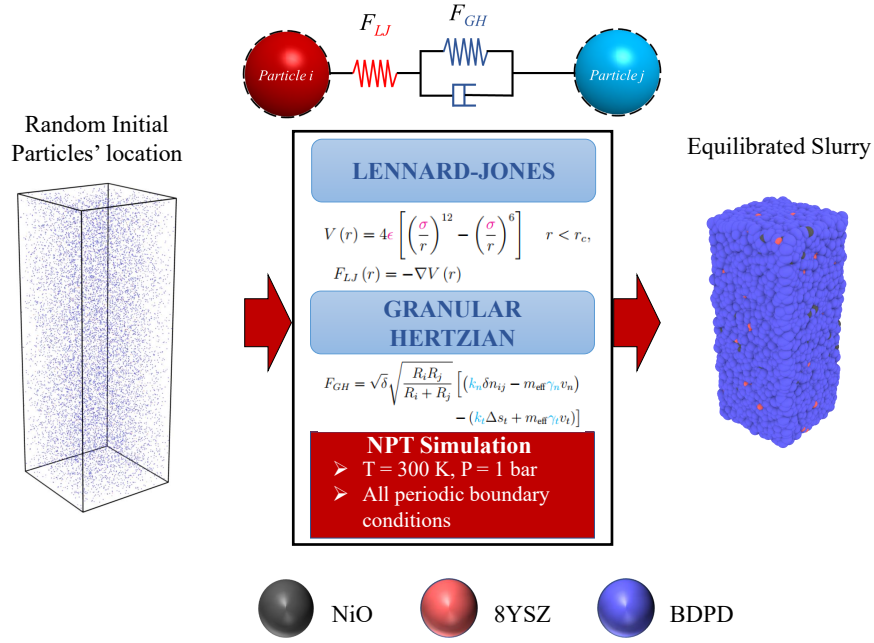

Figure 3.5. Diagram of the simulation and configuration of the slurry model. The initial random structure is shown on the left-hand side, where the number of NiO, 8YSZ, and BDPD particles are defined as a function of the mass, weight fractions, material density, and PSD. Centre, application of LJ and GH FF in all PBCs to obtain the equilibrated structure at 300 K and 1 bar, where the highlighted terms in the LJ and GH formulae indicate the parameters tuned. An example of the equilibrated slurry is shown on the right-hand side. Adapted from Prof. Dr. Alejandro A. Franco's lecture series at Université de Picardie Jules Verne (Amiens, France).

As a proof of concept, the calibration of two viscosity points is required to ensure that the simulated slurry behaves in agreement with the experimental one. A series of non-equilibrium (NE) simulations was adopted to determine multiple viscosity values against the desired shear rates. This was accomplished by altering the angle of the x-y plane with respect to the x direction and thus deforming the simulation box in a single lateral direction. The length of the simulation box multiplied by the selected shear rate in the y direction determines the deformation rate. Consistency is maintained by using the same FF parameter values as in the slurry simulation. It is worth noting that a single NE simulation calculates the shear stress for the applied shear rate, meaning each simulation produces one point of the shear-viscosity curve. Besides, it is also necessary to allow enough time for the simulation to converge on the target viscosity

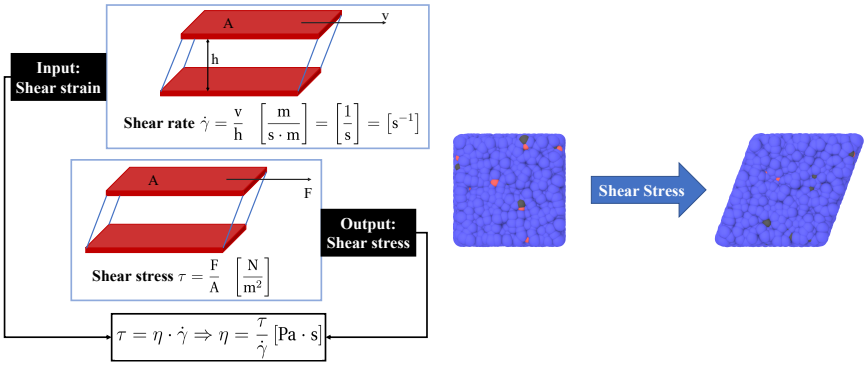

Figure 3.6. Schematic of the computational procedure to calculate the slurry viscosity corresponding to a certain shear rate through NE simulation. Adapted from Prof. Dr. Alejandro A. Franco's lecture series at Université de Picardie Jules Verne (Amiens, France).

value. In this work, the NE simulations were deployed by running 10^7 timesteps with a size of $\Delta t = 0.001$ µs. The simulated viscosity was, then, calculated by taking the mean of the instantaneous viscosity measurements following the convergence of the simulation. The viscosity calibration was performed on a small slurry microstructure (14 162 particles). After the calibration of the viscosity achieved the experimental values, the model was scaled up to 226 568 particles to meet the expected thickness.

3.2.3 Drying

In this subsection, the workflow of the simple drying model, developed within the ARTISTIC research initiative, is presented for the case of the fuel-electrode support. The model adopts a computational strategy akin to the slurry model and simulates the 3D substrate microstructure emerging from the drying process, using the 3D slurry microstructure from the preceding subsection as input (Figure 3.7). Drying is represented by the homogeneous shrinkage of BDPD particles to mimic solvent evaporation. Specifically, all solvent-containing BDPD particles were instantaneously reduced in diameter from 1.8 µm to 0.38 µm. The DEM simulation proceeded until equilibrium was reached. This means that the FFs were re-calibrated to obtain a dried microstructure satisfying the experimental porosity and density. Stronger particle connections owing to binder bridges, along with the greater mechanical properties of the green tape are explained by an increase in the attractive and elastic interactions, which is the basic difference between FFs of the slurry and drying phases. Consequently, the thickness drops from top to bottom. Throughout the simulation, the temperature remains constant at 300 K at each time step. Since the drying process only removes the solvent, the number of BDPD particles is conserved, and the amount of BDPD in the dried microstructure can therefore be directly quantified from the initial slurry composition.

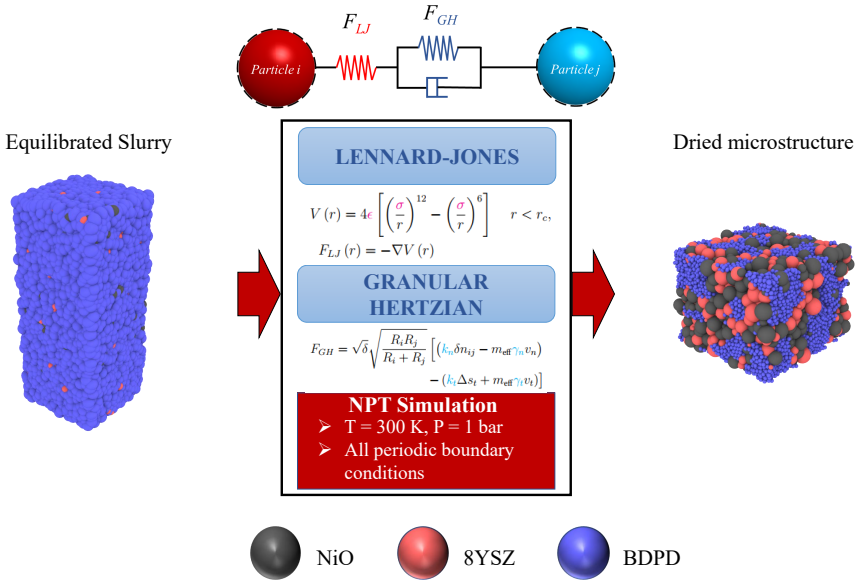

Figure 3.7. Diagram of the simulation and configuration of the homogeneous drying model. The slurry mesostructure is shown on the left-hand side. Centre, application of LJ and GH FF in all PBCs to obtain the equilibrated structure at 300 K and 1 bar, where the highlighted terms in the LJ and GH formulae indicate the parameters tuned. An example of the dried microstructure is illustrated on the right-hand side. Adapted from Prof. Dr. Alejandro A. Franco's lecture series at Université de Picardie Jules Verne (Amiens, France).

The simulation domain sizes were chosen to ensure that each system contained a sufficient number of particles to simulate the SC used in the experiment. The sizes of the simulation domain must also be consistent with the experimental physical properties of the substrate. Besides, these simulation domain sizes should represent a balance between computational cost and the physical representativeness of the substrate system. In this work, for each phase, two domain sizes were employed: a larger domain regarding the experimentally measured thickness for the slurry or the corresponding dried microstructure, providing the validation of the simulated microstructure, and a smaller domain used as a representative test case to assess finite-size effects. The small and large domains of the slurry simulation were approximately $L_x \times L_y \times L_z = 13 \times 13 \times 32\ \mu m^3$ and $L_x \times L_y \times L_z = 17 \times 17 \times 300\ \mu m^3$, respectively. The corresponding small and large domains for the dried microstructures were approximately $L_x \times L_y \times L_z = 12 \times 12 \times 9\ \mu m^3$ and $L_x \times L_y \times L_z = 16 \times 16 \times 90\ \mu m^3$, respectively. Simulations for both small and large domain sizes showed no significant differences in agreement with the experimental measurements, confirming that finite-size effects are negligible.

The DEM approach was conducted using LAMMPS software to model the slurry and drying phases of the tape-casting process of fuel-electrode substrates in SOCs. Figure 3.8a illustrates the tape-casting process for the FESC support, highlighting the two stages being simulated: the slurry preparation and its drying process. The 3D slurry microstructure and the corresponding dried microstructure obtained from the DEM simulation are shown for each stage. The computational workflow is illustrated in Figure 3.8b. In the slurry phase, NiO and 8YSZ are almost obscured by the BDPD including the solvent. Furthermore, the image also shows the dried microstructure obtained after solvent removal by shrinking the BDPD spheres in order to mimic the solvent evaporation. Several simulations were performed following this workflow to ensure proper statistical representativeness. The PSD used for the simulation can also be found in Appendix A (Figures A.1 and A.2). The FF parameter values about the slurry and drying phase are provided in Appendix A (see Table A.1). All the simulations were run on the MatriCS High Performance Computing cluster of the Université de Picardie Jules Verne, in Amiens, France, using one node with 128 GB of RAM and 2 processors (Intel® Xeon® CPU E5-2680 v4 @ 2.40 GHz, 28 cores) [117]. Simulating the large microstructure, comprising 226 568 particles, required approximately 78 hours for the slurry stage and 226 hours for the drying stage, while simulations of the smaller microstructure, containing 14 162 particles, completed in approximately 10, 14, and 29 hours for the slurry, viscosity, and drying stages, respectively.

3.3 Results and discussion

In order to further optimise the models and assess the physicochemical aspects of the slurry simulation, the BDPD diameter and its density are taken into account. The interaction among these material particles was controlled by the FF parameters, which were parameterised to imitate the experimental properties. In other words, all FF parameters were calibrated to achieve a simulated density value within the experimental uncertainty range. Specifically, the experimental casting-slurry density value of $2.23\ \mathrm{g/cm^3}$ is utilised to validate the calculated slurry microstructure with a simulated density of $2.22\ \mathrm{g/cm^3}$. Furthermore, the rheological properties of the casting slurry also have an effect on the fabrication of the substrate [118, 119]. It is, therefore, important to ensure that the simulated slurry behaves like the experimental one. The casting slurry should behave as if a shear-thinning fluid, also known as a pseudoplastic fluid, operates [120, 121], which means that the casting slurry exhibits a decreasing apparent viscosity with an increasing shear rate [122, 123]. Even though a full viscosity curve is desirable, this would be too computationally expensive and two viscosity values are determined to be sufficient for this proof-of-concept study. To meet this requirement, manually tuning the FFs to obtain two viscosity values corresponding to low and high shear rates was performed. The simulated viscosities corresponding to the chosen shear rates are shown in Table 3.2. The curves of the NE simulations for the simulated viscosities with respect to the two relevant shear rates are shown in Appendix A, Figure A.3.

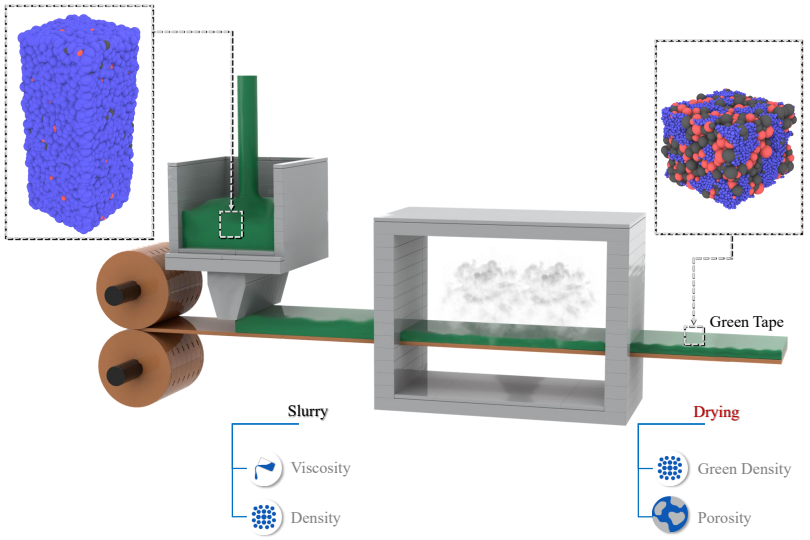

(a)

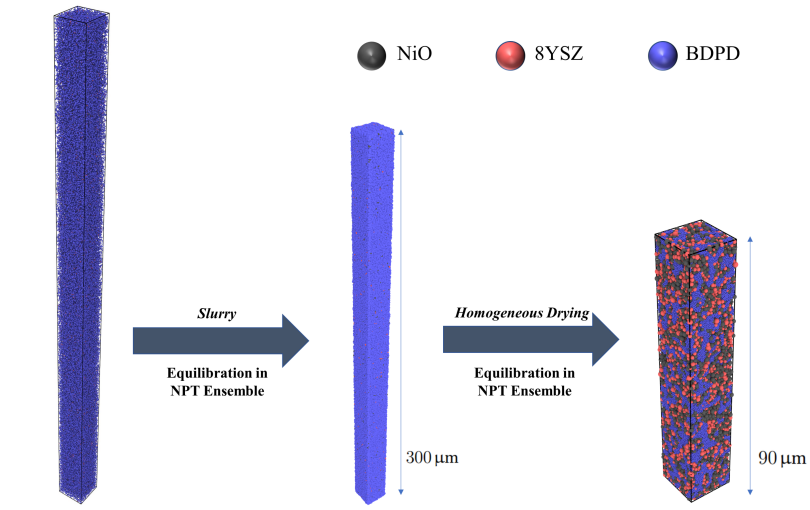

(b)

Figure 3.8. (a) A diagram illustrating the stages of the tape casting process of a SOC fuel-electrode support. (b) A schematic snapshot of the computational workflow depicting each simulation step in this work. The workflow starts with an initial configuration consisting in a random spatial distribution of particles. Afterwards, the slurry microstructure is obtained by performing the simulation until the intial structure is equilibrated in the NPT ensemble. Grey spheres represent NiO, light red particles illustrate 8YSZ, and slate-blue spheres exhibit Binder Dispersant Plasticiser Domain (BDPD).

Table 3.2. Experimental and simulated viscosity as a function of the shear rate.

Shear rate (s^{-1})	**viscosity** $(\mathrm{Pa}\cdot\mathrm{s})$	
80 ± 0.3	Experiment	1.7 ± 0.3
	Simulation	1.9 ± 0.2
100 ± 0.3	Experiment	1.5 ± 0.3
	Simulation	1.6 ± 0.1

In the drying phase, the porosity calibration is used as a means to validate the DEM model. The experimental porosity of the green sample is calculated as

$$\phi_{\text{exp}}\,(\%) = \frac{V_{\text{pore}}}{V_{\text{green tape}}} \times 100\%, \tag{3.5}$$

where V_{pore} is the pore volume of the green sample, and $V_{\text{green tape}}$ is the volume of the green sample.

It is critical to ensure the stability and reproducibility of the DEM simulations to validate the reliability of the generated data. Regarding this, six different simulations (Slurry Microstructure 1–6) were conducted for the slurry phase by varying the initial positions of the particles, number of particles in the simulation box, and the size of the simulation box, providing various microstructures for the analysis to ensure the consistency of the microstructural properties and particle arrangement of this model. Subsequently, these slurry microstructures served as inputs to generate the dried microstructures (Dried Microstructures 1–6) in the drying phase. The simulated density and porosity of these dried microstructures were calculated to ensure the stability and consistency of the DEM model, achieving the values of $3.45 \pm 0.01\ \mathrm{g/cm^3}$ for the green density, and $9.7 \pm 0.3\ \%$ for the porosity, in good agreement with those of the experiment which are $3.46\ \mathrm{g/cm^3}$ and $9.6\ \%$ for the green density and porosity, respectively. All information pertaining to these simulated microstructures can be found in Appendix A (Table A.2). Additionally, a Radial Distribution Function (RDF) was adopted to evaluate the microstructural characteritics of the slurry and dried microstructures. As a robust analytical tool, RDFs enable the evaluation of structural consistency in the microstructures across various simulation runs by implementing a quantitative measurement for comparing particle arrangements in a 3D microstructure during the simulation. Figures 3.9 and 3.10 depict the RDF analyses in the slurry and drying phases. Figure 3.9 demonstrates the RDF curves of six different slurry microstructures in terms of three different scenarios, namely NiO-8YSZ pair-correlation (Figure 3.9a), NiO-NiO pair-correlation (Figure 3.9b), and 8YSZ-8YSZ pair-correlation (Figure 3.9c). Likewise, Figure 3.10 shows the corresponding RDF curves for the dried microstructures in terms of four different scenarios: pair-correlation for all particle types (Figure 3.10a), NiO-8YSZ pair-correlation (Figure 3.10b), NiO-NiO pair-correlation (Figure 3.10c), and 8YSZ-8YSZ pair-correlation (Figure 3.10d). In the slurry stage, solid particles, such as NiO and 8YSZ, are suspended in a liquid phase. This is also

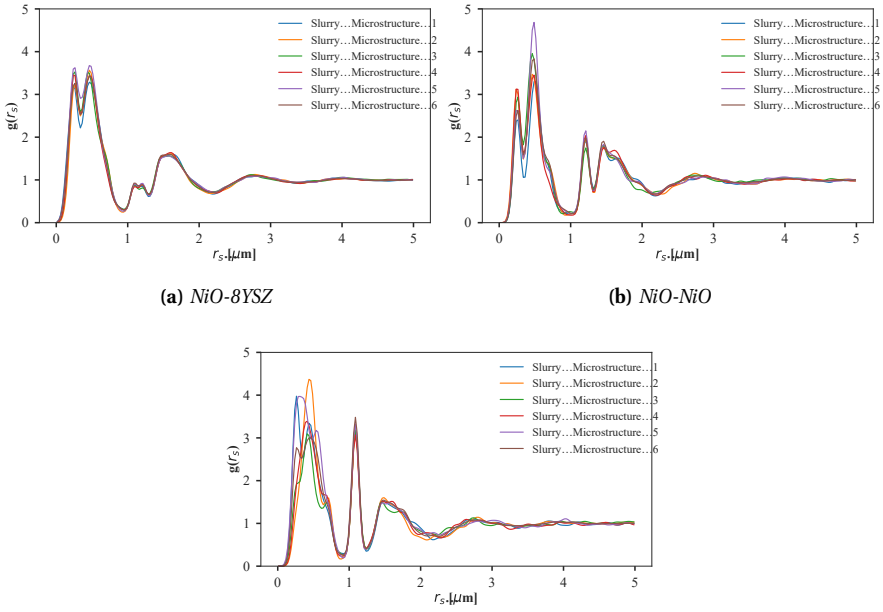

(a) *NiO-8YSZ* **(b)** *NiO-NiO*

(c) *8YSZ-8YSZ*

Figure 3.9. Pair-wise radial distribution functions (RDFs) for 6 different slurry microstructures with respect to all cases: (a) NiO-8YSZ, (b) NiO-NiO, and (c) 8YSZ-8YSZ. The first peaks in all RDFs are quite high, demonstrating that NiO and 8YSZ particles cluster at short distances within the slurry. Comparative analysis of the RDFs confirms the co-existence of both particle types in close proximity. Particularly, in the case of NiO-NiO correlations, the first peak is slightly lower than the second peak, attributable to the intervening presence of 8YSZ particles at shorter radial distances from the reference NiO particle. g(r) tends to unity at long distances indicating that the particles are well dispersed throughout the microstructure—characteristic behaviour of a stabilised casting slurry system.

explained in the simulation when most solid spheres were covered by the BDPD overlapped highly to effectively mimic the behaviour of viscous suspensions such as the slurry (Figure 3.8b). In other words, BDPD particles serve as a liquid phase surrounding the solid particles in the slurry phase, which results in the relative distribution of NiO and 8YSZ particles being the main object investigated in the slurry stage. By contrast, in the drying stage, BDPD particles tend to cluster after solvent removal to function as binder bridges, which enables stronger particle bonds as well as a higher level of stiffness. Hence, BDPD was taken into consideration along with NiO and 8YSZ particles during the drying stage. Overall, RDFs indicate consistency during the microstructural evolution in both slurry and drying steps. The RDF curves for each type of particle interaction are nearly identical regarding different microstructures within

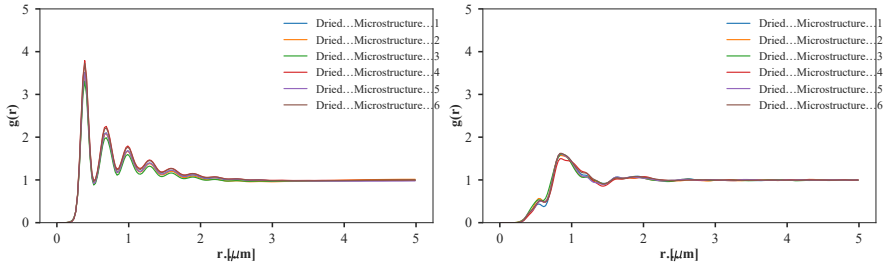

(a) *All particle pairs* **(b)** *NiO-8YSZ*

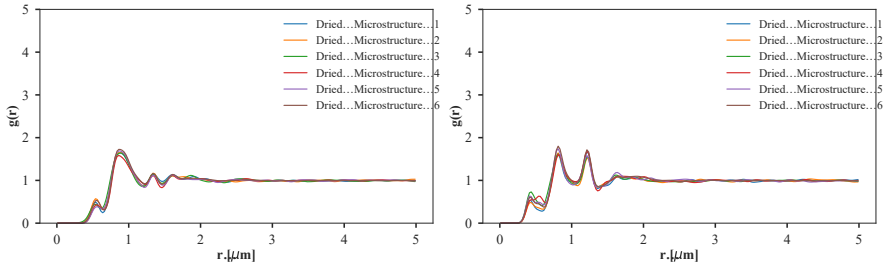

(c) *NiO-NiO* **(d)** *8YSZ-8YSZ*

Figure 3.10. Pair-wise RDFs for the dried microstructures corresponding to their slurry microstructures with respect to all cases: (a) All particle pairs, (b) NiO-8YSZ, (c) NiO-NiO, and (d) 8YSZ-8YSZ. RDFs of the dried microstructures demonstrate a stable particle configuration, characterised by distinct primary peaks that gradually decay to $g(r) = 1$ beyond radial distances of approximately 2.5 µm, which demonstrates transition to homogeneous particle distributions at longer distance. In general, RDFs reveal significant differences between the slurry and dried microstructures, highlighting structural changes in particle distribution as the system transitions from the slurry phase to the drying phase.

each phase. Nevertheless, the differences between RDFs are smaller in the drying phase. This explains the difference in NiO and 8YSZ particle distribution between the slurry and drying phases. Furthermore, the consistency shown by RDFs also ensures the confidence of the DEM model regardless of the initial particle configurations or model size, which supports the reproducibility and reliability of the DEM model.

To further characterise the dried microstructure, I analysed the simulated thick dried microstructure (90 µm in thickness, composed of $226\,568$ particles). The volume fraction for each material phase in z-axis (i.e. along the thickness) is shown in Figure 3.11. Overall, Figure 3.11 illustrates a consistent trend of the volume fraction distribution of all material phases, which is critical for fabricating the green tape. Specifically, NiO and 8YSZ occupy the majority of the volume fraction of the dried microstructure. While the volume fraction of NiO decreases, the volume fraction of 8YSZ

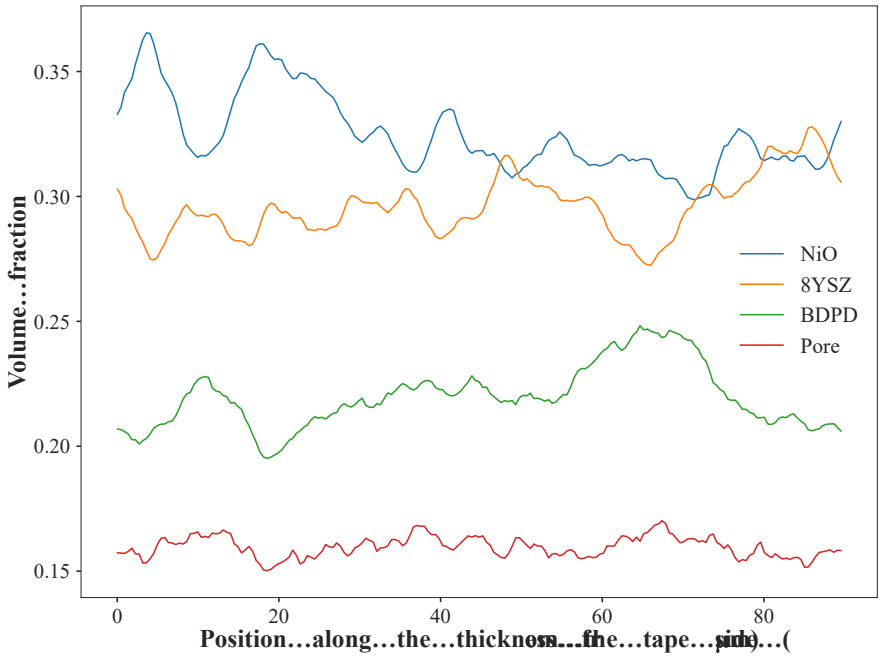

Figure 3.11. Volume fraction evolutions of NiO, 8YSZ, BDPD and pores along the thickness of the dried substrate microstructure.

increases along the thickness from bottom to top of the dried microstructure. This demonstrates the interaction between the NiO and 8YSZ particles during the formation of the dried microstructure. The trend for the volume fraction distribution of the BDPD phase reflects an homogeneous distribution of binders and additives throughout the dried microstructure. The volume fraction of the pores remains low along the thickness of the dried microstructure. Figure 3.12 demonstrates cross-sectional views of the dried microstructure of the fuel-electrode support obtained from the DEM simulation at various depths. Specifically, the cross section of the dried microstructure was extracted along the thickness direction after voxelising the 3D dried microstructure of the simulated support by using an in-house Python script. It is clear that the cross-sectional microstructures show that the phases, including NiO (green), 8YSZ (yellow), BDPD (dark purple), and pore (dark blue), are well-distributed within the examined slices, which aligns with the distribution of the volume fraction of each phase. Moreover, the cross-sectional views show the tight arrangement of the particles within the examined slices. These cross-sectional views indicates the correlations between NiO and 8YSZ particles along the thickness of the dried microstructure. The cross-sectional views also demonstrate the role of BDPD as the binder bridges for the NiO and 8YSZ particles as already discussed above. These characterisations of phases

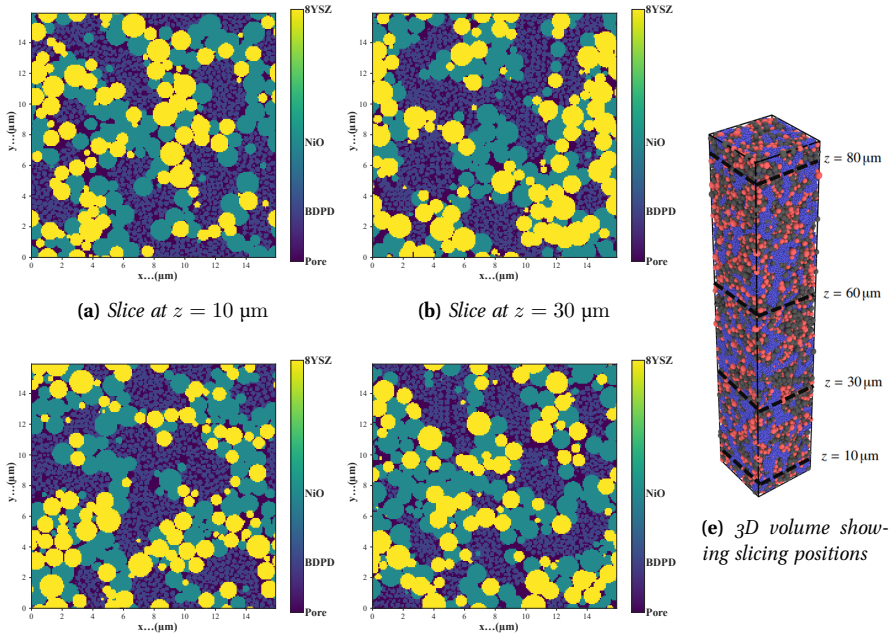

(a) *Slice at* $z = 10$ µm

(b) *Slice at* $z = 30$ µm

(c) *Slice at* $z = 60$ µm

(d) *Slice at* $z = 80$ µm

(e) *3D volume showing slicing positions*

Figure 3.12. Cross-sectional views of the dried microstructure (90 µm in thickness) resulting from the simulation, shown in the xy plane (i.e. along the thickness direction), at various depths: (a) Slice at $z = 10$ µm, (b) Slice at $z = 30$ µm, (c) Slice at $z = 60$ µm, and (d) Slice at $z = 80$ µm. Each color represents a different phase, namely NiO, 8YSZ, BDPD, and pore. (e) 3D volume showing slicing positions, providing an overview of the simulated volume and the planes where the cross-sections (a–d) were taken.

in the examined simulated dried microstructure are also affirmed by calculating the coordination number to provide an idea of particle packing and connectivity after solvent evaporation in the tape-casting process (Figure 3.13). Indeed, Figures 3.13a and 3.13b show strong spatial correlations between the coordination number of NiO and that of 8YSZ. This implies NiO and 8YSZ particles were well-mixed during the slurry preparation and remained uniformly distributed after drying, which is an important characteristic for ensuring mechanical stability as well as enhancing connectivity in the final microstructure for the next manufacturing step, the sintering process. Meanwhile, the coordination number of BDPD exhibits a uniform distribution along the microstructure (Figures 3.13c and 3.13f). The high values (i.e. orange or red) correspond to tight particle arrangement in the examined area due to the presence of the binder phase (BDPD). Furthermore, BDPD forms a network connected along the microstructure reflecting the role of BDPD in supporting the connection between particles, which is of the utmost importance in the formation of a stable microstructure.

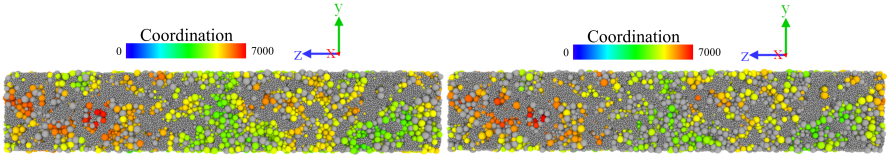

(a) *Coordination number of NiO (with all particles)* **(b)** *Coordination number of 8YSZ (with all particles)*

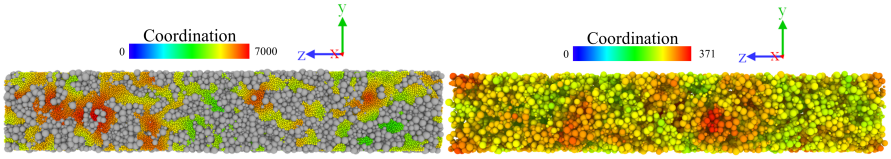

(c) *Coordination number of BDPD (with all particles)* **(d)** *Coordination number of NiO-NiO particles*

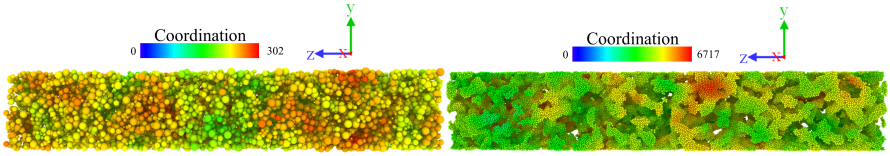

(e) *Coordination number of 8YSZ-8YSZ particles* **(f)** *Coordination number of BDPD-BDPD particles*

Figure 3.13. Coordination number of particles in the dried microstructure. The colour code exhibits the reference particles, such as (a) NiO, (b) 8YSZ, (c) BDPD. The rest of particles in contact with the reference particles are shown in grey. The colour zone exhibits only the reference particles in contact wth each other, such as (d) NiO-NiO particles, (e) 8YSZ-8YSZ particles, (f) BDPD-BDPD particles.

Besides, a Pore Network Model (PNM) is shown in Figure 3.14. To investigate the pore structures as well as their distribution, the diverse shapes of pores are approximated as spheres for simplification by using the Avizo software (Thermo Fisher Scientific) [124]. Specifically, Figure 3.14 illustrates the distribution of pores along the thickness of the calculated microstructure of the green tape. PNM shows that the size of the pores in the simulated microstructure ranges between 0 µm and 2.5 µm. Along the microstructure, there is a homogeneous distribution of pores, where each pore is approximately 2 µm in size. Meanwhile, larger pores are located closer to the central section of the simulated green tape. A well-optimised pore arrangement in the dried microstructure of the fuel-electrode support in FESCs facilitates the formation of a favourable microstructure after the sintering process. This helps to ensure efficient gas transport, a high density of triple-phase boundaries, and improved fuel utilisation. It also contributes to mechanical robustness during sintering, which is critical for long-term cell performance.

SEM and tomography characterisations can provide valuable insights into the green tape microstructure of the fuel-electrode support, yet their application at this early

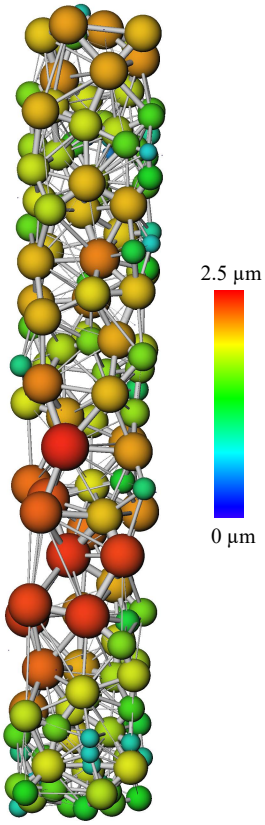

Figure 3.14. Pore Network Model of the dried microstructure for the SOC support, illustrating the pore distribution and size throughout the dried microstructure. The colour bar indicates equivalent pore diameters, while the throaths indicate the pore interconnections.

stage is often limited due to technical constraints. The model provides a valuable first step in visualising features that are difficult to observe through experimental imaging, particularly the distribution of materials with low imaging contrast. It therefore serves as a useful complement to direct imaging and supports an integrated modelling and experimental approach for gaining deeper insights into how manufacturing processes influence material distribution and final properties. Besides, the DEM-generated dried microstructure, representing the green body of the fuel-electrode support, can also serve as the starting point for multiscale modelling. Specifically, it can be used as input for a phase-field model to simulate sintering. The resulting sintered microstructures can then be employed in subsequent performance-oriented simulations (e.g., Lattice Boltzmann method, pore network modelling) or thermo-mechanical durability studies (e.g., finite element analysis).

3.4 Conclusions and perspectives

In this chapter, a physics-based computational workflow, based upon DEM framework from ARTISTIC research initiative, to simulate the tape casting process of a SOC fuel-electrode support made of NiO/8YSZ cermet is presented for the first time. The DEM model was calibrated with in-house experimental data, such as the slurry density, the viscosity of the slurry, the density and the porosity of the green tape so as to reproduce the experimental conditions as closely as possible. This model describes two main stages in the tape casting process of the fuel-electrode support, namely the slurry casting and its drying. The performed DEM simulations allow linking each step of the tape-casting process to the 3D-resolved microstructure of the support, by verifying its properties for good agreement with experimental data. This allows for an efficient and more physics-based approach than those based upon stochastic generation of microstructures. A homogeneous distribution of all materials throughout the dried microstructure was observed from the simulation, which is expected to happen in practice before the heat treatment of the green tape.

The model employs a homogeneous drying assumption for the BDPD particles, which is a simplification of the actual drying behaviour. While this represents an approximation, it is sufficient in the context of this proof-of-concept study to capture the main trends of the tape casting and drying processes. The debinding and sintering of the materials helps control the porosity and avoid undesirable pore clustering after the sintering process. These processes, not considered in this first modelling proof of concept, enhance both the mechanical performance and electrochemical properties of the support [125].

The work reported herein further exhibits that the ARTISTIC workflow can be applied not only to batteries but also to other technologies such as SOCs. Nevertheless, the ARTISTIC framework can be extended to also simulate properties involved in other processing steps of SOC supports as well as functional layers, such as the sintering process. It is useful, as a future perspective, to complement the present findings with supplementary imaging characterisation to provide better insights related to material processing/performance coupling. Even though this DEM model has some limitations due to its assumptions (e.g. consideration of spherical particles), it provides, to the best of my knowledge, the most complete computational approach to connect manufacturing with the microstructure properties. It also remains particularly well suited to investigate, from a physical perspective, the tape casting process. By using this experimentally validated computational workflow, numerous combinations of the manufacturing parameters may be researched to inspect quickly the material processability before performing the experimental fabrication. This results in a powerful computational approach for the generation, with physics background, of component microstructures utilised in a wide spectrum of energy conversion applications.

4

A HYBRID SURROGATE MODELLING OF THE SLURRY IN THE SUBSTRATE MANUFACTURING FOR SOLID OXIDE CELLS BY COUPLING PHYSICS-BASED SIMULATION AND DEEP LEARNING

This chapter discusses a hybrid surrogate modelling framework to simulate the solvent-based slurry of the fuel-electrode substrate. The study aims to develop a more computationally efficient surrogate approach for the slurry simulation pertaining to SOC manufacturing by integrating the DL and DEM modelling framework. As a proof of concept, various slurry microstructures were generated using the DEM framework in Chapter 3 with a set of FFs and a specific formulation. This work specifically employs a modified VGG16 architecture to predict slurry microstructure from DEM simulations, leveraging its deep hierarchical feature learning for complex pattern recognition in material structures.

4.1 Introduction

Building upon the DEM framework within ARTISTIC project introduced in Chapter 3, the DEM model allows the generation of the slurry microstructures at the mesoscale by using FFs to characterise the physicochemical interaction between pairs of material particles in the equilibrated casting slurry. Nonetheless, mesoscale computational simulation of the slurry still requires faster preprocessing processes to save computational cost. The rapid progress in high-performance computing and AI provides powerful tools for computational research on SOCs [126, 127, 128]. In this context, ML

and, more recently, DL techniques have been increasingly employed to complement physics-based simulations, particularly when dealing with high-dimensional and spatially correlated data [129, 130]. Among these, Convolutional Neural Networks (CNNs) have emerged as one of the most effective architectures for capturing spatial features, which makes them especially suitable for modelling complex microstructures.

A CNN, also known as a ConvNet, is a type of artificial neural network widely used in traditional computer vision tasks, for instance, video analysis, image classification [131, 132], object localisation, object detection [133, 134], and image segmentation [135]. Overall, CNNs are frequently composed of multiple convolutional layers, certain fully connected layers, and a classification softmax layer that uses, for example, a cross-entropy loss. In addition to classification, CNNs are used to cope with regression problems, resulting in a linear activation function, also known as "no activation", or "identity function" used with a last fully connected regression layer in lieu of the softmax layer [136]. Furthermore, since the 3D-slurry microstructure is typically similar to a specialised type of grid structure, CNNs are advanced approaches for analysing the slurry microstructure from the DEM model. Consequently, the equilibrated microstructure modelled by DEM is obtained faster after several timesteps in place of running the whole DEM simulation, allowing to lower computational costs.

In this chapter, a hybrid surrogate model coupling DL and DEM is proposed to accelerate the simulation of the slurry phase in the substrate fabrication of fuel-electrode supported SOCs. The workflow is shown in Figure 4.1. As a proof of concept, the study focused on a specific formulation (52 % of NiO, 35 % of 8YSZ, and 13 % of BDPD) to generate the slurry dataset used to train the DL model. The set of FFs used for data generation is provided in Table B.1 in Appendix B. The DL model is trained using physics-based data of the slurry microstructure generated from DEM simulation based upon the ARTISTIC framework [137]. Specifically, CNN model was employed with a slightly altered architecture to predict a pseudo microstructure of the slurry. This pseudo microstructure was processed to obtain a predicted microstructure. After that, the 3D predicted microstructure was run for a few timesteps using DEM to make the particle relaxation in the simulated slurry, which enables the final slurry microstructure to be more stable. Model validation was conducted using a dual-metric strategy, incorporating both a direct data-based comparison and an assessment derived from microstructure functional analysis. Significantly, this hybrid framework, DL-DEM, offers a major advantage by drastically reducing the computational time required for conventional DEM drying simulations without compromising the integrity of the results.

4.2 Methodologies

4.2.1 Data Generation

The dataset used in this study was generated using the previously reported physics-based manufacturing modelling workflow for the fuel-electrode substrate (Chapter

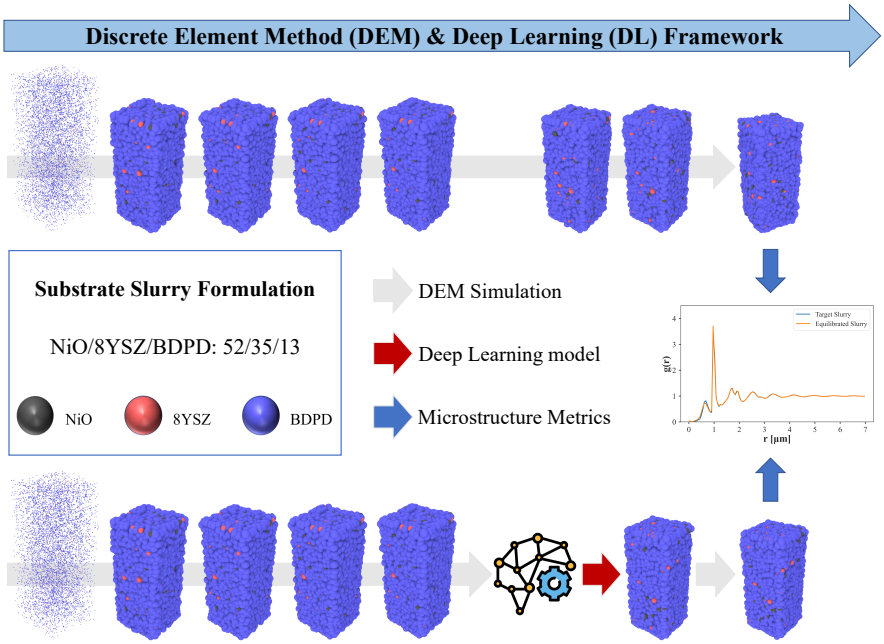

Figure 4.1. Schematic representation of the hybrid surrogate model for 3D slurry microstructure prediction of the fuel-electrode substrate. The workflow integrates DEM simulations (grey arrows) and the DL (red arrows) at the slurry preparation stage. The equilibrated slurry obtained from the hybrid model was compared with the target slurry from the pure DEM simulation.

3). This workflow employs the DEM to sequentially simulate slurry formation and subsequent drying, yielding distinct 3D mesoscale microstructures at each stage. The physicochemical properties of the casting slurry are described using a combination of LJFF and GHFF (see Equations (3.3)–(3.3)). The LJFF approximates the nonbonded interaction between particles within the simulation box, while the GHFF governs the mechanical properties of the contacting particles.

In the present study, a dataset of slurry microstructures is constructed to train the DL model for predicting the final microstructure. Synthetic slurry microstructures for DL model training were generated using the DEM framework, producing 3D microstructures of casting slurries with various thicknesses and sizes. Slurry thickness was controlled by adjusting the material quantity, resulting in a higher number of particles within the simulation box. Consequently, computational time depended upon slurry volume, with larger volumes requiring longer simulation durations.

It is worth mentioning that a single formulation (52% of NiO, 35% of 8YSZ, and 13% of BDPD) and an unique FF set were employed for data generation, allowing multiple microstructures to remain physically consistent and representative of a well-defined

system. This allows the dataset to capture intra-system variability arising from random particle packing, simulation box scaling, and process conditions, while maintaining a consistent physical framework for the slurry system. The approach is suitable for a proof-of-concept study aimed at validating the proposed hybrid workflow, quantifying its computational benefits, and evaluating its predictive capability.

A total of 15 simulations of solvent-based slurry were conducted on the MatriCS High Performance Computing platform at the Université de Picardie Jules Verne (Amiens, France), using one node per simulation equipped with 128 GB of RAM and 2 processors (Intel® Xeon® CPU E5-2680 v4 @ 2.40 GHz, 28 cores) [117]. Eight simulations were randomly used for model training and validation, while the remaining were reserved for testing. All simulations reached equilibrium after six million timesteps, with each timestep corresponding to 0.0001 microseconds. Since frames are generated every fifty thousand timesteps, each simulation produced 121 frames once the slurry microstructure equilibrated at the timesteps of 6 000 000 (Table 4.1). Further details on initial particle configurations, particle size distributions, and simulation parameters are available in the previous chapter. All information about slurry microstructures generated by the DEM framework can be found in Appendix B (Tables B.2 and B.3).

Table 4.1. Summary of the simulation configuration for data generation.

Parameters per simulation	Slurry simulation	Description
Timestep (µs)	0.0001	Δt to update the positions
Total steps	6 000 000	Total number of iterations
Simulation time (µs)	600	Total duration of the simulation
Frames storage interval	50 000	Steps at which coordinates are recorded
Total number of frames	121	Coordinates are printed at specified frame storage interval
Wall time (hrs.)	20.5	Total DEM simulation time. This depends upon computational resources available.

4.2.2 Data preprocessing

In the DEM simulation, PBCs are applied in all three Cartesian directions, allowing particles to exit the simulation box on one side and re-enter from the opposite side. This presents a significant challenge for the model to learn particle behaviour near the simulation boundaries, where interactions may occur across the periodic edges. To address this limitation, unwrapped coordinates (i.e. the raw positions of particles without

any the effect of periodic boundary conditions, showing the continuous trajectory of a particle) were used for model training instead of wrapped coordinates. This approach enabled the model to more accurately capture particle trajectories, whereas wrapped coordinates provided only relative positions within the simulation box, making it more difficult for the DL model to learn consistent particle motions. Without loss of generality, relevant particle information is extracted from LAMMPS dump files, including particle types, radii, unwrapped coordinates, and coordination numbers. These data are then structured into a matrix format for model training.

A matrix storing the data of all particles from the i-th simulation for $i = 1, \cdots, 8$ is written as

$$X_i = \begin{bmatrix} X_{i,1} \\ X_{i,2} \\ \vdots \\ X_{i,N-1} \\ X_{i,N} \end{bmatrix}, \tag{4.1}$$

where $X_{i,j}$ is matrices containing the j-th particle information corresponding to the i-th simulation for $j = 1, \cdots, N$ and expressed as

$$X_{i,j} = \begin{bmatrix} t_1^{i,j} & r_1^{i,j} & ux_1^{i,j} & uy_1^{i,j} & uz_1^{i,j} & c_1^{i,j} \\ t_2^{i,j} & r_2^{i,j} & ux_2^{i,j} & uy_2^{i,j} & uz_2^{i,j} & c_2^{i,j} \\ t_3^{i,j} & r_3^{i,j} & ux_3^{i,j} & uy_3^{i,j} & uz_3^{i,j} & c_3^{i,j} \\ t_4^{i,j} & r_4^{i,j} & ux_4^{i,j} & uy_4^{i,j} & uz_4^{i,j} & c_4^{i,j} \end{bmatrix}, \tag{4.2}$$

where $t_k^{i,j}$, $r_k^{i,j}$, $ux_k^{i,j}$, $uy_k^{i,j}$, $uz_k^{i,j}$, and $c_k^{i,j}$ represent the particle types, radii, unwrapped coordinates and coordination number values, respectively, corresponding to k-th frame for k = 1, $\cdots$, 4.

Consequently, a matrix which collects the particle information from the slurry-phase simulation is expressed as follows:

$$X = \begin{bmatrix} X_1 \\ X_2 \\ X_3 \\ X_4 \\ X_5 \\ X_6 \\ X_7 \\ X_8 \end{bmatrix}. \tag{4.3}$$

Similarly, the output is the unwrapped coordinates of the particles, which means the particle position without any periodic transformation in the equilibrated microstructures, as described earlier. These coordinates are presented as

$$Y = \begin{bmatrix} Y_1 \\ Y_2 \\ Y_3 \\ Y_4 \\ Y_5 \\ Y_6 \\ Y_7 \\ Y_8 \end{bmatrix}, \tag{4.4}$$

where

$$Y_i = \begin{bmatrix} Y_{i,1} \\ Y_{i,2} \\ \vdots \\ Y_{i,N-1} \\ Y_{i,N} \end{bmatrix}, \tag{4.5}$$

in which

$$Y_{i,1} = \begin{bmatrix} ux_{i,1} & uy_{i,1} & uz_{i,1} \\ ux_{i,2} & uy_{i,2} & uz_{i,2} \\ \vdots & \vdots & \vdots \\ ux_{i,N-1} & uy_{i,N-1} & uz_{i,N-1} \\ ux_{i,N} & uy_{i,N} & uz_{i,N} \end{bmatrix}, \tag{4.6}$$

where the subscripts, i and N, symbolise the i-th simulation and the number of particles, respectively.

The entire dataset was randomly split into training and validation subsets containing 80% and 20% of the whole dataset, respectively. The training set was used to train the model, while the validation set was utilised to fine-tune the hyperparameters and prevent overfitting. Unseen data from new simulations was used to evaluate the model's generalisation capability.

4.2.3 Modified VGG16 model

VGG16, a well-known CNN architecture proposed by Karen Simonyan and Andrew Zisserman, was originally designed for image classification tasks [138]. The model typically comprises sixteen layers, including thirteen convolutional layers and three fully connected layers. In fact, the full architecture contains twenty-one layers, including the five max-pooling layers. Nevertheless, the model is referred to as VGG16 because it contains only sixteen weight layers. Although the VGG16 architecture was primarily designed for image classification, this model can be altered for regression tasks.

In this study, the particle dataset is represented as a structured matrix of particle features, exhibiting a grid-like topology suitable for one-dimensional (1D) CNN architectures. By reshaping the original VGG16 architecture to suit a 1D regression task, the VGG16 spatial hierarchy can be effectively leveraged for the particle dataset. Specifically, 2D convolutional layers (Conv2D) are replaced with 1D convolutional layers (Conv1D), resulting in the internal modification of convolutional layers such as the number of kernel size. The pooling layer must also be adapted to maintain the consistency of the VGG16-based architecture. In particular, the max-pooling layer remains applicable, provided it operates in a manner compatible with the 1D feature sequence. Besides, the final fully connected layer is modified to perform regression instead of classification. Table 4.2 shows the architecture of the modified VGG16 model for regression tasks, adapted from the standard VGG16 implementation in Keras. The "None" in the output shape refers to a flexible batch size dimension, as per TensorFlow/Keras conventions [139, 140].

The loss function and evaluation metrics used during model training to quantify the average difference between target and predicted values were the mean squared error (MSE) and mean absolute error (MAE), respectively. The loss function was used to optimise the model's hyperparameters, while the evaluation metrics were used to assess the model's performance after training. Lower MSE and MAE values demonstrate that the model's predictions are closer to the ground truth. These metrics are defined as follows:

$$\mathrm{MSE} = \frac{1}{N}\sum_{i=1}^{N}\left(\boldsymbol{Y}_i - \hat{\boldsymbol{Y}}_i\right)^2, \tag{4.7}$$

and

$$\mathrm{MAE} = \frac{1}{N}\sum_{i=1}^{N}\left|\boldsymbol{Y}_i - \hat{\boldsymbol{Y}}_i\right|, \tag{4.8}$$

where N is the number of particles, $\boldsymbol{Y}_i$ represents the unwrapped coordinates of the ith particle, and $\hat{\boldsymbol{Y}}_i$ is the predicted unwrapped coordinates of the ith particle.

To evaluate the DL model performance, the coefficient of determination (R^2) was used on completely unseen dataset. This metric indicates the proportion of the total variance in the dependent variable that is explained by the model, with values closer

to 1 representing better predictive performance. The coefficient of determination is defined as

$$R^2 = 1 - \frac{\sum_{i=1}^{N} \left(\boldsymbol{Y}_i - \hat{\boldsymbol{Y}}_i \right)^2}{\sum_{i=1}^{N} \left(\boldsymbol{Y}_i - \bar{\boldsymbol{Y}} \right)^2}, \tag{4.9}$$

where $\bar{\boldsymbol{Y}}$ is the mean of the unwrapped coordinate.

Table 4.2. Summary of the modified 1D VGG16 architecture for the DL model, adapted from the original 2D VGG16. The network comprises sequential convolutional blocks, followed by a flattening layer and fully connected dense layers. The final fully connected dense layer produces three regression outputs. "None" denotes a placeholder, indicating that the network can process multiple samples per gradient update.

Layer	Output shape	Parameter no.
Conv1D	(None; 4; 64)	1 216
Conv1D	(None; 4; 64)	12 352
MaxPooling1D	(None; 2; 64)	0
Conv1D	(None; 2; 128)	24 704
Conv1D	(None; 2; 128)	49 280
MaxPooling1D	(None; 1; 128)	0
Conv1D	(None; 1; 256)	98 560
Conv1D	(None; 1; 256)	196 864
Conv1D	(None; 1; 256)	196 864
MaxPooling1D	(None; 1; 256)	0
Conv1D	(None; 1; 512)	393 728
Conv1D	(None; 1; 512)	786 944
Conv1D	(None; 1; 512)	786 944
MaxPooling1D	(None; 1; 512)	0
Conv1D	(None; 1; 512)	786 944
Conv1D	(None; 1; 512)	786 944
Conv1D	(None; 1; 512)	786 944
MaxPooling1D	(None; 1; 512)	0
Flatten	(None; 512)	0
Dense	(None; 4 096)	2 101 248
Dense	(None; 4 096)	16 781 312
Dense	(None; 3)	12 291
Total		**23 803 139**

The Open Visualization Tool (OVITO) package was used for the visualisation of all 3D microstructures [141], including both target and predicted structures, for visual comparison.

4.2.4 Slurry microstructure post-processing framework

The proposed framework combines the DL approach already described above with DEM simulations to model the slurry microstructures. The DL model was first trained on four initial slurry-microstructure frames corresponding to the timesteps 350 000, 400 000, 450 000, and 500 000. After training, the DL model predicted the pseudo microstructure representing the slurry frame at the timestep 6 000 000, expressed in unwrapped particle coordinates. Then, this pseudo microstructure was wrapped with PBCs to obtain the predicted one using the OVITO package and used as the initial configuration for a fixed number of DEM simulation steps. These DEM simulations enable the system to relax physically, removing unphysical particle displacements which can arise from the particle wrapping process. The resulting output from this procedure is a physically refined slurry microstructure (our final slurry microstructure) (Figure 4.1).

The incorporation of DEM steps is of the utmost importance in ensuring the resulting particle configurations better reflect realistic behaviours by enforcing physical constraints to mitigate the potential unphysical jumps of particles during the PBC wrapping process. Overall, this integration of DEM into the predictive framework not only enhances the physical consistency of the slurry microstructures but also improves the reliability and accuracy of the modelling outcomes.

4.3 Results and discussion

4.3.1 Modified VGG16 performance

The modified VGG16 model was fine-tuned with different sets of hyperparameters. The best configuration was trained for 1000 epochs with a batch size of 500, using the Adamax optimiser with a learning rate of 0.0001. Further details of the selected hyperparameters are provided in Appendix B (Table B.4). Figure 4.2 illustrates the evolution of both MSE and MAE for the training and validation sets over the epochs during the training of the modified VGG16 model. During training, both MSE (loss, Figure 4.2a) and MAE (error, Figure 4.2b) curves for the training and validation sets stabilised and converged, indicating that the CNN (the modified VGG16) learned effectively. The close alignment between the training and validation curves for both metrics further suggests that the model generalised well to unseen data and avoided overfitting.

The performance of the modified VGG16 model was evaluated by comparing the predicted and target values along the X, Y, and Z axes individually. Figure 4.3 illustrates the predicted versus target values for each axis with respect to Slurry 1 (see Table B.3 in Appendix B). In all cases, the predictions lie almost perfectly along the ideal prediction

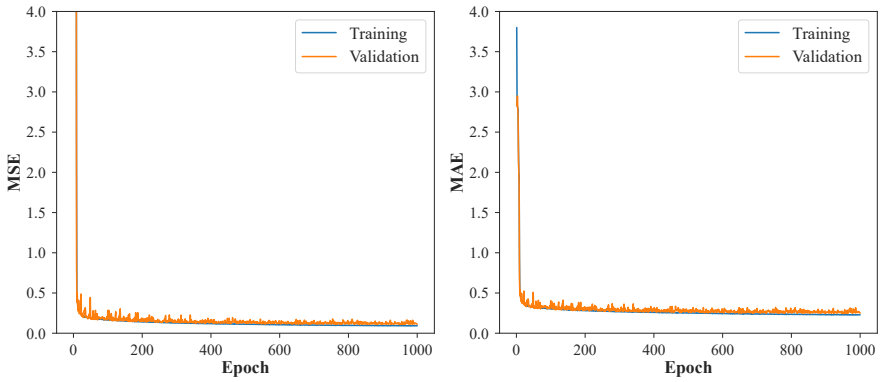

(a) *Mean squared error* **(b)** *Mean absolute error*

Figure 4.2. (a) Mean square error and (b) Mean absolute error curves showing the evolution of training and validation performance during training of the modified VGG16 CNN. The close alignment and convergence indicate effective learning and good generalisation.

line, suggesting extremely low error across all spatial directions. Furthermore, for each axis, the coefficient of determination R^2 was calculated to quantify how well the model predictions matched the ground truth. The resulting R^2 values were 0.994 for X, 0.994 for Y, and 0.999 for Z, indicating a very strong correlation between predicted and true values with an average R^2 of 0.996 for an unseen slurry dataset. These results demonstrate that the model not only predicted the overall trend of the data but also maintains high accuracy at the individual-axis level, providing confidence in its generalisation capability. The high R^2 values and the close alignment of predictions with target values indicate robust performance of the model in reconstructing multi-dimensional outputs.

4.3.2 Microstructure analysis for comparing hybrid approach

4.3.2.1 Visual comparisons

A visual comparison of the slurry microstructures was performed using OVITO. The target microstructure was generated directly using the physics-based simulation approach, while the predicted microstructure was obtained using the modified VGG16 model. For the equilibrated, the predicted microstructure was fed back into the DEM simulation framework to undergo an equilibration step, here referred as equilibrated microstructure (Figure 4.4). This step is crucial, as it uses the strengths of the physics-based model to refine and stabilise the structure [142, 143, 144]. The wall time of the whole process, including DL and DEM, is approximately 30 minutes, depending upon the simulated slurry volume. As shown in Figure 4.4, the three microstructures

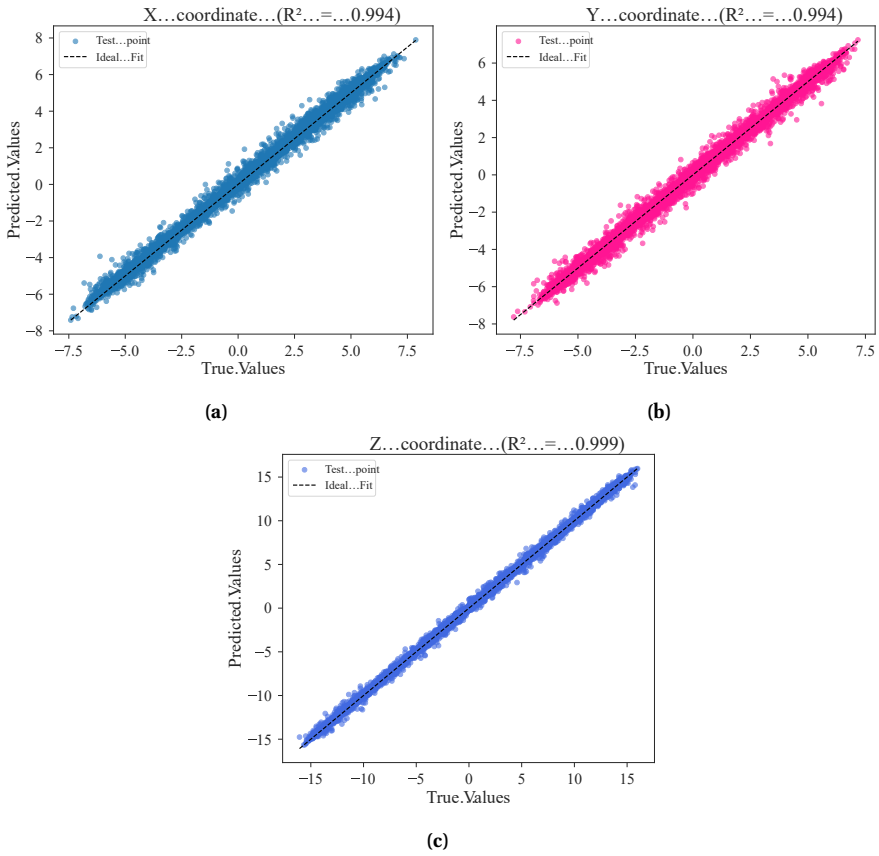

Figure 4.3. Target versus predicted plot along the X, Y, and Z axes for the modified VGG16 model validating the training performance. The high R^2 scores and the close alignment between predicted and target data points around the ideal prediction line indicate extremely low error and strong agreement between predictions and ground truth.

appear visually different, which is expected because the applied DL approach is data-driven. For this, measurements of density and volume were performed to compare the microstructure. As can be observed in Table 4.3, for microstructures 2 and 3, the DL-DEM model closely matches DEM predictions, indicating strong baseline predictive accuracy.

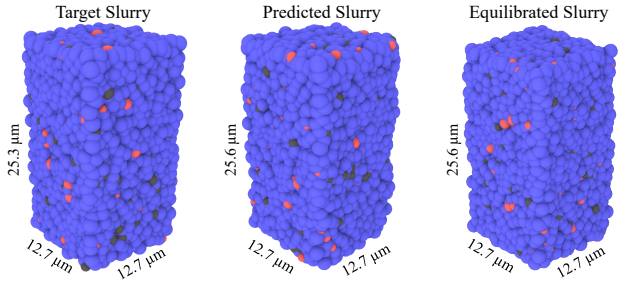

(a) *Slurry 2*

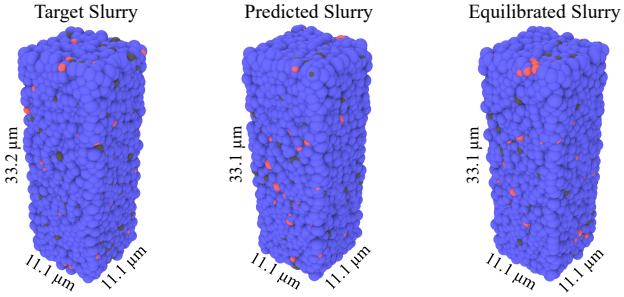

(b) *Slurry 3*

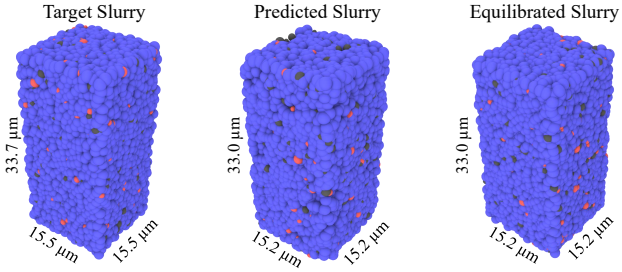

(c) *Slurry 4*

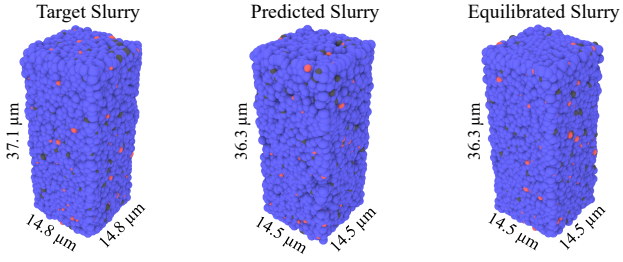

(d) *Slurry 5*

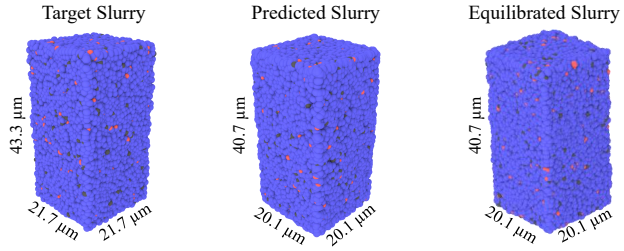

(e) *Slurry 6*

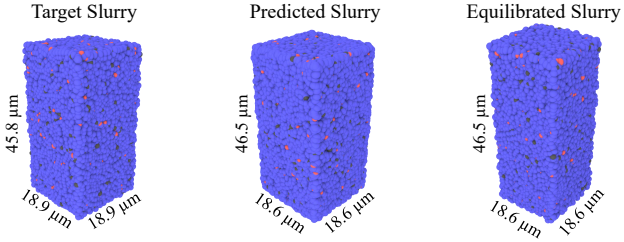

(f) *Slurry 7*

Figure 4.4. Unseen Slurry microstructure along with thickness comparison.

Table 4.3. Comparison of density and volume for different unseen slurry microstructures.

Slurry	**Model**	**Density** $[\mathrm{g/cm^3}]$	**Volume** $[\mu\mathrm{m^3}]$
Microstructure 2	DEM	2.2430	4 081
	DL-DEM	2.2169	4 129
Microstructure 3	DEM	2.2415	4 091
	DL-DEM	2.2486	4 078
Microstructure 4	DEM	2.2422	8 096
	DL-DEM	2.3810	7 624
Microstructure 5	DEM	2.2419	8 126
	DL-DEM	2.3870	7 632
Microstructure 6	DEM	2.2437	20 390
	DL-DEM	2.7822	16 443
Microstructure 7	DEM	2.2406	16 360
	DL-DEM	2.2799	16 087

As microstructural thickness increases, the hybrid model adapts its predictions but

begins to show noticeable deviations, particularly in Microstructure 6, where the density prediction increases to $2.7822\ \mathrm{g/cm^3}$ compared to the DEM estimate of $2.2437\ \mathrm{g/cm^3}$. These deviations can be attributed to the random fitting of particles during simulation, which introduces natural variation in particle counts, size distributions, and packing arrangements across microstructures. Such variability becomes more pronounced in larger and more complex systems, leading to higher prediction differences. For instance, in Microstructure 6, the hybrid model deviated by approximately 23.6% compared to other microstructures within the same complexity regime.

Despite these differences, the overall performance of the DL-DEM framework remains robust. Across all microstructures, the mean absolute difference in density was approximately $0.15\ \mathrm{g/cm^3}$, with a maximum deviation of $0.54\ \mathrm{g/cm^3}$ observed in the most complex case. Volume predictions followed similar trends, remaining within physically plausible ranges and reflecting changes in microstructural complexity. This stability indicates that the modified VGG16-based hybrid model demonstrates good generalisability across diverse microstructures without the need for modifying the NN architecture further.

4.3.2.2 Data metrics and physics-based analysis

4.3.2.2.1 Data metrics

To evaluate the predictive performance of the proposed hybrid DL-DEM model, standard regression metrics were calculated by comparing the predicted and target particle coordinates for each unseen slurry microstructure (Table 4.4). These metrics include the MSE and MAE, which quantify the magnitude of positional differences, and the coefficient of determination (R^2), which assesses how well the predicted data captures the variability present in the target data.

Table 4.4. Performance metrics (MSE, MAE, and R^2) for the hybrid DL-DEM model across unseen slurry microstructures.

Unseen Slurry Microstructure	**MSE** Target vs Predicted	**MAE** Target vs Predicted	**R^2** Target vs Predicted
Slurry 2	0.068	0.178	0.996
Slurry 3	0.060	0.165	0.996
Slurry 4	0.165	0.316	0.995
Slurry 5	0.152	0.305	0.995
Slurry 6	0.199	0.348	0.996
Slurry 7	0.094	0.226	0.998

Across all microstructures, the results show consistently low error values, with MSE ranging from 0.060 to 0.199 and MAE from 0.165 to 0.348. The lowest errors were observed for Slurry 2 and Slurry 3 (MSE = 0.060–0.068; MAE = 0.165–0.178), while

slightly higher values were noted for Slurry 4–6. These low errors indicate that the predicted particle positions are very close to the target positions. Furthermore, the R^2 values remain exceptionally high (0.995–0.998) across all cases, demonstrating that the hybrid model effectively preserves the variability and overall distribution of the target coordinates.

In addition to the quantitative metrics, the predicted particle coordinates were plotted against the target coordinates for all axes (X, Y, and Z) across each microstructure (Figure 4.5). The scatter plots demonstrate that the predicted points lie very close to the best-fitting line, indicating excellent agreement between the predicted and target coordinates. This visual confirmation supports the earlier data metric analysis, showing that the model accurately predicts particle positions across all spatial dimensions and for all microstructures. While this demonstrates numerical accuracy, the structural fidelity of the predicted microstructures will be further assessed using RDF analysis in the following part.

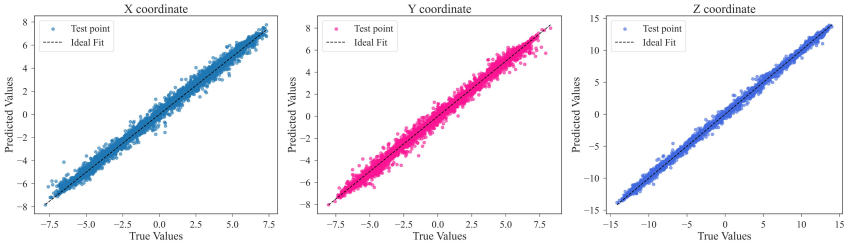

(a) *Slurry 2*

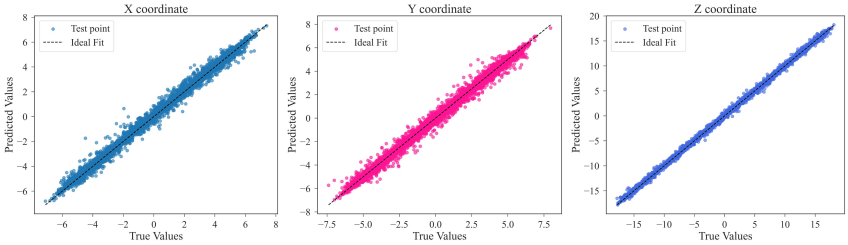

(b) *Slurry 3*

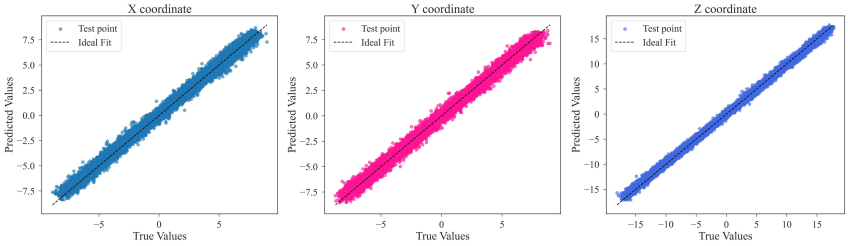

(c) *Slurry 4*

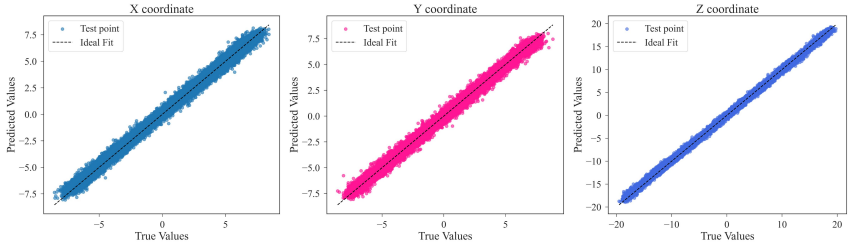

(d) *Slurry 5*

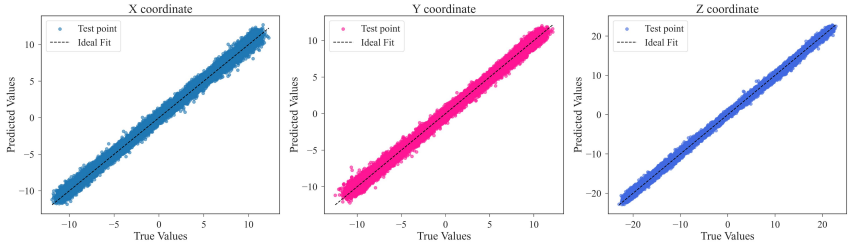

(e) *Slurry 6*

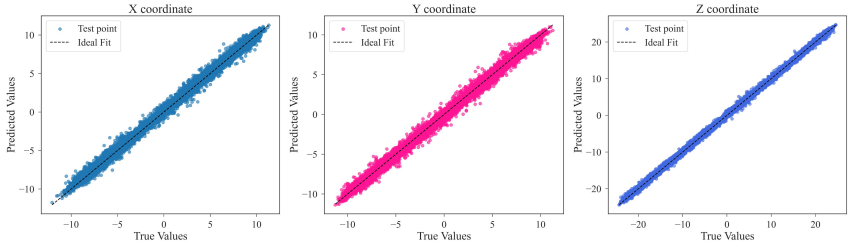

(f) *Slurry 7*

Figure 4.5. Target vs. predicted plot across different unseen slurry microstructures: (a) Slurry 2, (b) Slurry 3, (c) Slurry 4, (d) Slurry 5, (e) Slurry 6, and (f) Slurry 7 along the X, Y, and Z axes, where the ideal fit represents a perfect correlation between predicted and true values (particle coordinates).

4.3.2.2.2 Radial Distribution analysis

While the correlation plot (Figure 4.5) confirmed good agreement between predicted and target microstructural coordinates, the RDF was computed for both the equilibrated and the physics-based microstructures. The RDF was calculated separately for each particle type combination (BDPD-NiO-8YSZ and NiO-8YSZ). Because the spatial scales and interaction ranges vary between these combinations, the bin size/histogram resolution (Δr) and maximum cutoff distance (r_{max}) were adjusted to accurately capture both local and medium-range structural features. The respective RDF curves and specific parameters used are provided in the caption of Figure 4.6.

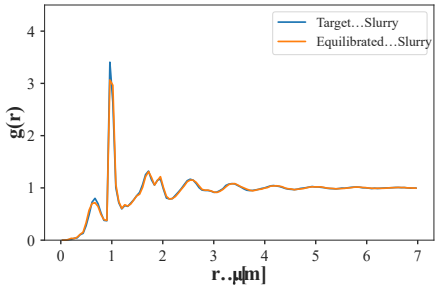

(a) *Slurry 2: All particle pairs*

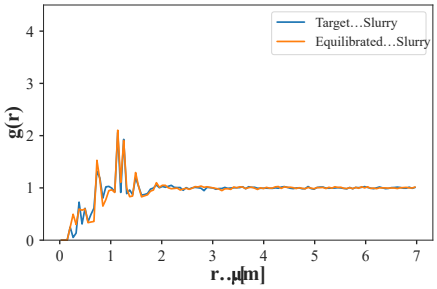

(b) *Slurry 2: NiO-8YSZ*

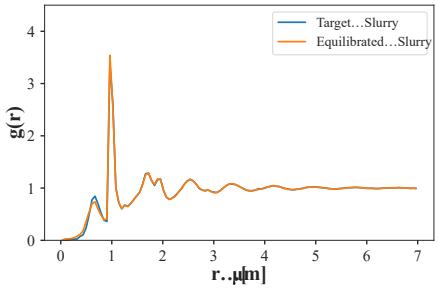

(c) *Slurry 3: All particle pairs*

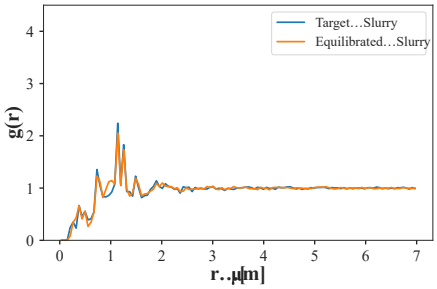

(d) *Slurry 3: NiO-8YSZ*

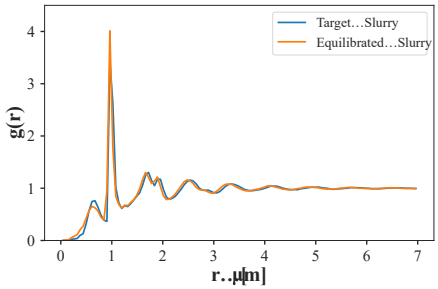

(e) *Slurry 4: All particle pairs*

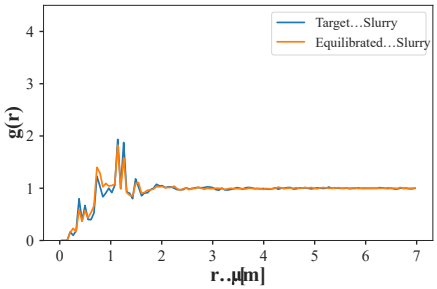

(f) *Slurry 4: NiO-8YSZ*

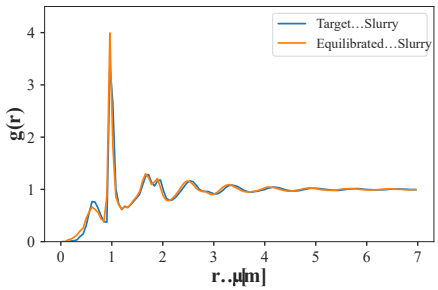

(g) *Slurry 5: All particle pairs*

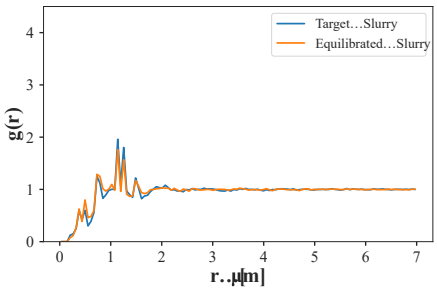

(h) *Slurry 5: NiO-8YSZ*

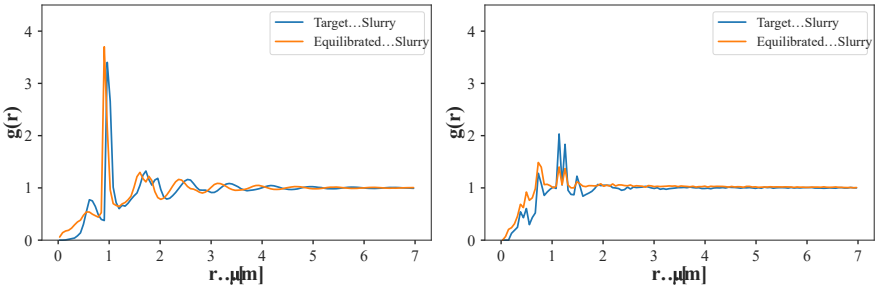

(i) *Slurry 6: All particle pairs*

(j) *Slurry 6: NiO-8YSZ*

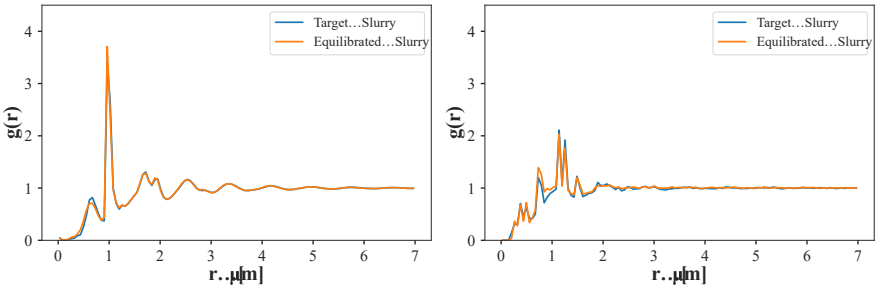

(k) *Slurry 7: All particle pairs*

(l) *Slurry 7: NiO-8YSZ*

Figure 4.6. Pair-wise RDFs comparing target and equilibrated microstructures of the unseen slurry microstructures: (a) Slurry 2: All particle pairs, (b) Slurry 2: NiO-8YSZ, (c) Slurry 3: All particle pairs, (d) Slurry 3: NiO-8YSZ, (e) Slurry 4: All particle pairs, (f) Slurry 4: NiO-8YSZ, (g) Slurry 5: All particle pairs, (h) Slurry 5: NiO-8YSZ, (i) Slurry 6: All particle pairs, (j) Slurry 6: NiO-8YSZ, (k) Slurry 7: All particle pairs, and (l) Slurry 7: NiO-8YSZ. The cutoff radius used for the RDF calculation is $r_c = 7$ µm, and the histogram resolution is $\Delta r = 0.0583$, corresponding to 120 bins.

Regarding RDF of all particle pairs (BDPD-NiO-8YSZ), (Figures 4.6a, 4.6c, 4.6e, 4.6g, 4.6i, and 4.6k), it can be observed that the equilibrated microstructure shows peaks for the first and subsequent nearest neighbors that align very well with the target in the cases of slurries 2, 3, 4, 5, and 7, suggesting that the hybrid approach (DL-DEM) accurately reproduces the local structural arrangement of these formulations. However, in the case of slurry 6, the RDF of the equilibrated microstructure follows the same overall trend but is slightly left-shifted, indicating that the average interparticle distances are smaller, which may be due to higher local packing density or differences in particle interactions for this formulation.

Since BDPD is present in abundance, it can significantly influence the overall microstructure. To isolate the effect of the remaining components, the RDF of NiO-8YSZ was also compared separately (Figures 4.6b, 4.6d, 4.6f, 4.6h, 4.6j, and 4.6l). A similar trend was observed across slurries 2, 3, 4, 5, and 7, where the peaks of the

equilibrated microstructure align well with the target. However, in the case of slurry 6, although the overall trend is maintained, the peak of the equilibrated microstructure is lower than that of the target, indicating a slightly reduced local ordering or weaker correlations between NiO and 8YSZ particles in this formulation.

Overall, the RDF analysis demonstrates that the predicted microstructures obtained using the hybrid approach (DL-DEM) reliably reproduce the local and intermediate structural arrangements of the target microstructures across most slurries. The close alignment of peaks for both BDPD-NiO-8YSZ and NiO-8YSZ, except for minor deviations in slurry 6, confirms the accuracy and robustness of the hybrid method in capturing realistic particle distributions and correlations.

4.4 Conclusions and Perspectives

This chapter developed a hybrid surrogate modelling framework that integrates DL with physics-based DEM simulations to overcome the high computational cost typically associated with repeated DEM runs and FF fitting. By training the modified VGG16 network on microstructural data from DEM simulations of the slurry preparation for the tape casting, the proposed hybrid model could predict final slurry microstructures efficiently. These predictions were subsequently equilibrated using DEM to ensure physical realism, creating a framework that leverages the strengths of both data-driven and physics-based approaches.

The hybrid approach demonstrated strong predictive accuracy across multiple slurry microstructures, as confirmed by low error metrics and RDF analyses. Minor deviations observed for certain slurry microstructures, such as thicker slurries, highlight potential areas for further refinement, but overall, the framework reliably captures local and intermediate structural arrangements. This methodology significantly accelerates validation and optimisation tasks that would otherwise rely solely on computationally intensive DEM simulations. By bridging experimental data, as presented in Chapter 3, physics-based simulations and data-driven methods, the hybrid approach provides a scalable and efficient strategy for modelling SOC slurry processing, representing a step forward toward practical, high-throughput experimentally validated digital models for future research. A natural extension of this approach will be on its application to drying, as recently demonstrated by Prof. Alejandro A. Franco's group [144].

5

Data-driven machine learning modelling for fuel electrode support manufacturing

This chapter studies a data-based approach to the manufacturing of the fuel-electrode substrate. Conventional SOC fabrication routes are resource-intensive and often rely on industry/R&D unpublished knowledge and trial-and-error practices to achieve the desired tape properties. Data-driven methods offer the potential to reveal quantitative relationships between manufacturing parameters and microstructural outcomes, thereby supporting process optimisation and scale-up. The following sections present the workflow and key results obtained in this study.

5.1 Introduction

Tape casting is a well-known fabrication technique to produce thin ceramic sheets from ceramic slurry [75, 145, 146]. Since tape casting is potentially cost-efficient for mass production, this technique is preferable to produce SOC components [72, 147, 148]. To produce a high-quality green tape of the cermet-based substrate, traditional optimisation commonly relies on trial-and-error [78, 79, 80], leading to significantly substantial resource and time expenditure. The precise control of green tape thickness is crucial for governing the properties of the final tape-cast product [149, 150]. In this regard, predicting the thickness and density of the tape obtained after drying is of the utmost importance in supporting the optimisation of the tape casting process. Nevertheless, the manufacturing process for the fuel-electrode support necessitates careful control over numerous relevant parameters such as temperature, doctor blade gap, casting speed, humidity, and exhaust air volume flow rate, as these directly influence the resulting green tape properties, indirectly impacting the tape during subsequent

heat treatment stages. Such complex relationships are difficult to reproduce by using physico-chemical models, especially when drying and sintering need to be considered.

Alternatively, machine learning (ML) offers a powerful approach for this prediction task by learning from the data describing the complex manufacturing process, including tape casting and subsequent heat treatment processes such as sintering and reduction. This data-driven machine learning surrogate approach can predict a broad spectrum of material properties without requiring a fundamental understanding of their underlying chemistry or physics [151, 152]. The application of ML-based techniques has recently achieved remarkable success in various fields of materials and energy sciences [142, 153, 154, 155, 156, 157, 158, 159, 160], including predicting material activity and properties [161, 162, 129], aiding new material discovery [163, 164, 165], driving material design [166, 167, 168], and analysing electrochemical energy device manufacturing [169, 170, 171, 172, 173]. These successes are achieved through the high quality of the dataset used in the relevant research. Effective data collection strategies are, therefore, critical for further advancing these applications, particularly within the context of data-driven manufacturing of SOCs. To ensure comprehensive and systematic data management in the present research, the ELN was utilised in this work. Specifically, eLabFTW [174], a free and open-source electronic lab notebook, was implemented with a new Application Programming Interface (API) to enhance data traceability. This integration allows manufacturing parameters, routinely recorded in the machine's log files, to be directly and systematically transferred into eLabFTW. his automated process facilitates comprehensive and structured data management for the research. By leveraging the data-driven approach combining ML, the tape properties can be predicted for each fabrication stage in this study. a modular ML approach was developed to model the complex manufacturing process of the FESC support by training and evaluating separate predictive models on experimental data. This approach enables us to independently and accurately assess the predictability of the ML models, mitigating the forecast error accumulation across each stages [175, 176].

In this work, a data-driven ML modelling framework is proposed to predict tape properties throughout the fabrication process of the fuel-electrode support, encompassing tape casting including drying, sintering, and reduction processes. To the best of my knowledge, this is the first ML-based data simulation workflow of the fuel-electrode substrate manufacturing processes so as to predict the thickness and density of the support at each fabrication stage. The workflow is shown in Figure 5.1, in which the terms green thickness/density denote the thickness and density of the sample after drying, and reduced thickness/density refer to the corresponding values measured after the NiO-to-Ni reduction stage. This study aims to develop a comprehensive understanding and predictive capability for the multi-stage fabrication process of the fuel-electrode supports. By combining rigorous semi-automated data collection with ML techniques, this novel approach using experimental data provides valuable insights about the direct influence of manufacturing parameters on the tape thickness and density throughout the tape casting stage, indirectly impacting the tape during subsequent sintering and reduction steps.

5.2 Materials and methods

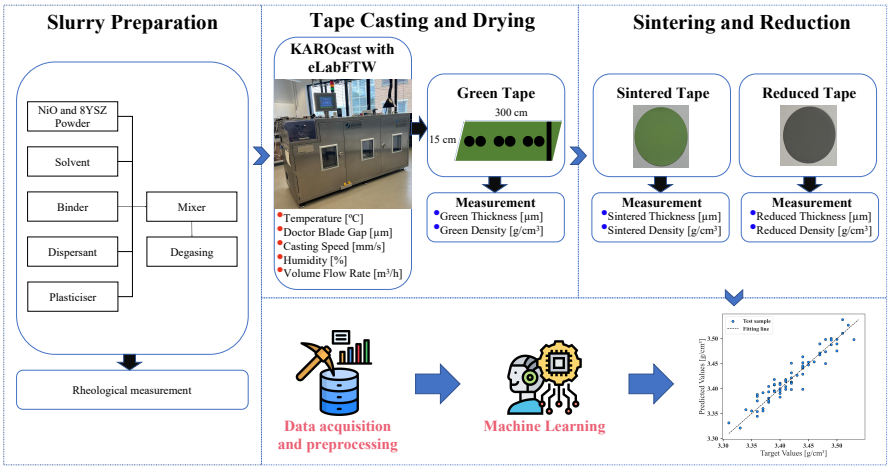

Figure 5.1. Schematic workflow of a data-driven machine learning framework for the manufacturing process of the fuel-electrode substrate. Firstly, the slurry was prepared, and its viscosity was measured. Subsequently, the tape casting was performed to collect the data. The green tape was sintered and reduced after its measurement. Data were collected experimentally and preprocessed to construct a dataset for the SOC support fabrication process. The dataset was utilised to train and test different ML models to select the best fitting model and the respective hyperparameter fine-tuning for each prediction task.

5.2.1 Slurry preparation and rheological measurements

In this study, NiO (Green Nickel Oxide) and 8YSZ (8 mol% white yttria-stabilized zirconia) were used as the starting materials for the fuel electrode substrate to prepare the solvent-based slurry. A mixture of NiO and 8YSZ ($57:43$ volume fraction) was mixed with Ethanol, Methyl ethyl ketone, binders, dispersants, and plasticisers in the mixer for 10 hours [101]. The ceramic powders, organic materials and solvents used for the slurry preparation are listed in Table 5.1. The particle size distributions of NiO and 8YSZ were indistinguishable in the final prepared slurry and determined by d_{10} = 0.35–0.45 µm, d_{50} = 0.5–0.7 µm, and d_{90} = 0.8–1.0 µm. Figure 5.2 further illustrates the detailed particle size distribution of the ceramic powder mixture in the prepared slurry.

The rheological behaviour of the slurry was investigated using a rotational rheometer (Physica MCR 301, Anton Paar GmbH, Austria) equipped with a coaxial cylinder measurement setup (CC27). To characterise the properties of tape casting slurries with different temperatures, the rheological measurements were conducted at 20 °C, 21 °C,

Table 5.1. Raw materials used to prepare the casting slurry.

Material	Function	Supplier
NiO	Powder	G. Vogler B.V.
8YSZ	Powder	Imerys
Ethanol	Solvent	Merck
Methyl ethyl ketone	Solvent	Merck
Polyvinyl butyral B-98	Binder	Solutia Inc.
Solusolv S-2075	Plasticiser	Solutia Inc.
PEG400	Plasticiser	Merck
BYK 220 S	Dispersant	BYK

25 °C, and 26 °C and fresh slurries were loaded for each experiment so as to ensure the accuracy of the measurement.

5.2.2 Data acquisition

In order to eliminate variations related to slurry quality, all green tapes were produced using the same slurry batch according to the consistent procedure on a micro tape-casting machine (KAROcast $300 - 7$, KMS Automation GmbH, Germany). The tape-casting data were collected from both an automated logging system of the casting machine through ELN and physical measurements. Specifically, 29 green tapes (300 cm length and 15 cm width) were performed with different manufacturing parameters, namely temperatures (bewteen 22 and 60 °C), doctor blade gaps (200, 300, 400 and 500 µm), casting speeds (2.5, 5, and 7.5 mm/s), humidity (recorded in %) and exhaust air volume flow rate (automatically regulated in m^3/h by the machine based upon supply and exhaust fan speeds). Nevertheless, it is worth mentioning that owing to the limitation in control and tracking, humidity was manually recorded at the time of casting implementation using a hygrometer of the tape-casting device. After the tape-casting step, at least six circular samples with a diameter of 43.85 mm, as well as one stripe sample, were punched from each tape in order to evaluate the homogeneity of the green tape's thickness disdtribution (Figure 5.3). At least nine thickness values were measured for each green sample and the respective green density was then calculated from the weight-to-volume ratio. Subsequently, the green samples were labelled with their corresponding tape ID numbers to track their evolution throughout subsequent processes and subjected to pre-sintering at 1230 °C for 3 hours to remove the binder and prepare for the subsequent sintering step. Following pre-sintering, the samples were sintered at 1400 °C for 5 hours, yielding sintered samples with

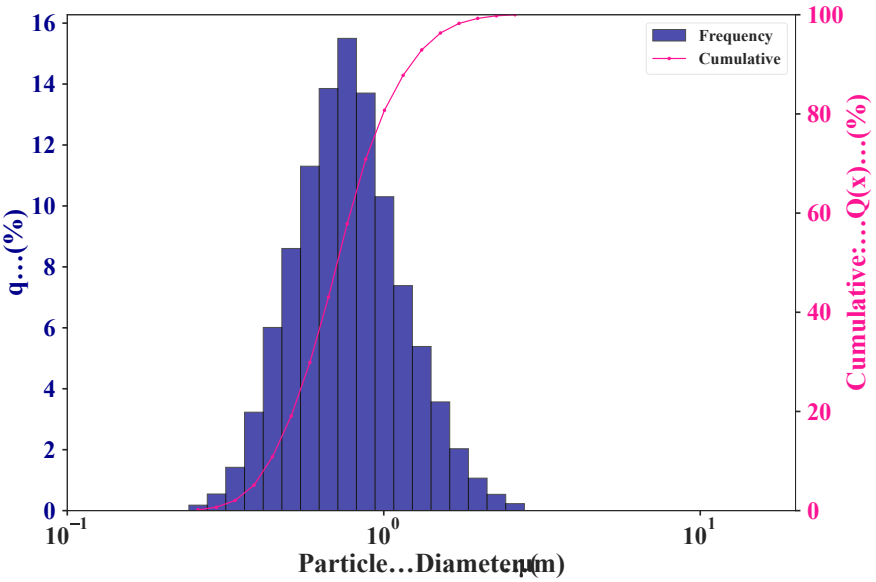

Figure 5.2. Particle size distribution of both NiO and 8YSZ in the Casting Slurry. The primary y-axis on the left displays the frequency distribution (q(%)), showing the percentage of particles within a specific range of diameters. The secondary y-axis on the right-hand side represents the cumulative distribution (Q(x) (%)), indicating the total percentage of particles with a diameter smaller than a given size. The particle diameter is plotted on a logarithmic scale (x-axis, µm).

the desired microstructure and porosity. This second sintering step mimics the co-sintering of the electrolyte together with the fuel electrode and the substrate in the typical SOC half-cell manufacturing sequence. Thereafter, the thickness and density of sintered samples were determined experimentally. Finally, a reduction step was carried out in an Ar/H_2 atmosphere at 900 °C for 3 hours to achieve metallic Ni as for the final functional properties, followed by the experimental determination of the reduced samples' thickness and density.

5.2.3 Correlation Analysis

Correlation analysis techniques have been employed to analyse the fundamental correlation, relationships and characteristics between key manufacturing parameters and the green tape properties within the dataset. The most prevalent techniques are Pearson's correlation coefficient and Spearman's correlation coefficient. Pearson's correlation coefficient measures the linearity correlation between two continuous random

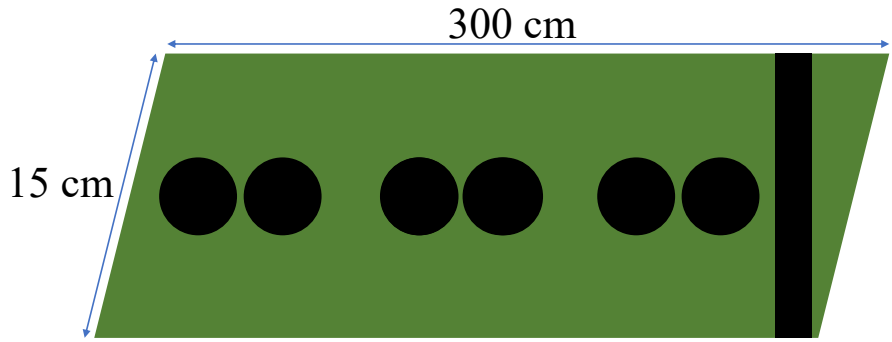

Figure 5.3. Circular samples and stripe were punched from each tape with dimensions $300\,\mathrm{cm} \times 15\,\mathrm{cm}$ (length $\times$ width).

variables and is given by

$$\rho_p = \frac{\sum_{i=1}^{n} (x_i - \bar{x})\,(y_i - \bar{y})}{\sqrt{\sum_{i=1}^{n} (x_i - \bar{x})^2 \sum_{i=1}^{n} (y_i - \bar{y})^2}}, \tag{5.1}$$

where n is sample size, x_i and y_i are the values of variables X and Y for the i-th observation, and $\bar{x}$ and $\bar{y}$ are the means of variables X and Y, respectively [177].

Spearman's correlation coefficient is utilised to capture monotonic relationship between two continuous random variables and is defined as

$$\rho_s = 1 - \frac{6 \sum_{i=1}^{n} d_i^2}{n\,(n^2 - 1)}, \tag{5.2}$$

where d_i denotes the difference between the ranks of x_i and y_i for the ith observation [177].

5.2.4 Machine learning modelling

The full dataset comprises 357 observations. Each sample is described by 5 distinct attributes, such as temperature, doctor blade gap, casting speed, humidity, and exhaust air volume flow rate, used as inputs to train independent ML models so as to predict the green thickness as well as green density for the tape-casting process. The green thickness and green density are then used as inputs for the sintering models to predict the thickness and density of the sintered tape. Similarly, the reduction stage models utilised sintered thickness and sintered density to forecast thickness and density in the reduced state. Furthermore, to track the tape's evolution as well as capture batch-specific variations of the tape after the tape-casting process, the tape ID numbers were also considered as an important feature in enhancing the performance of ML models in the sintering and reduction process.

In preparation for modelling, the raw dataset is randomly divided into an 80% training set and a 20% testing set. The training set is used to train models to make predictions, while the testing set is used to evaluate the performance of trained models on unseen data. Indeed, the testing dataset includes experimental data that models have not seen during the training yet, equivalent to testing the models against previously unperformed experiments. The modular ML approach was adopted to model a series of multi-stage manufacturing processes of the fuel electrode substrate from tape casting to sintering and to reduction, which enables the optimisation of the prediction for the physical properties of the tape at each fabrication stage. For each manufacturing process, a number of regression algorithms were evaluated for each prediction task. Repeated k-Fold Cross-Validation, with k $= 10$ and 3 repetitions, was performed for model selection and hyperparameter tuning. Specifically, the training set was randomly split into 10 equal folds. In each iteration of a 10-fold process, the model was trained using 9 folds and then validated on the remaining fold. This procedure was repeated 10 times, where each fold served as the validation fold once. Subsequently, the entire 10-Fold Cross-Validation procedure was reiterated 3 times with different randomisations each time, which resulted in the production of 30 distinct performance evaluations in total. The scores from all repetitions are finally averaged to obtain the final score for model assessment. Mean Squared Error (MSE) was used as a primary loss function for the optimisation during this cross-validation process, and MSE is defined as

$$\text{MSE} = \frac{1}{n}\sum_{i=1}^{n}\left(y_i - \hat{y}_i\right)^2, \tag{5.3}$$

where n is the number of observations, y_i represents the ith observed value, and $\hat{y}_i$ is the ith predicted value.

The algorithm with the optimal set of hyperparameters demonstrating the best performance on this cross-validation phase would be selected as the final model for each specific prediction task. The final models were then re-trained on the entire training dataset and evaluated on the testing dataset using key regression metrics, namely mean absolute error (MAE), root mean squared error (RMSE), and coefficient of determination (R^2). These are defined as follows:

$$\text{MAE} = \frac{1}{n}\sum_{i=1}^{n}\left|y_i - \hat{y}_i\right|, \tag{5.4}$$

$$\text{RMSE} = \sqrt{\text{MSE}} = \sqrt{\frac{\sum_{i=1}^{n}\left(y_i - \hat{y}_i\right)^2}{n}}, \tag{5.5}$$

and

$$R^2 = 1 - \frac{\sum_{i=1}^{n} (y_i - \hat{y}_i)^2}{\sum_{i=1}^{n} (y_i - \bar{y})^2}, \tag{5.6}$$

where $\bar{y}$ is the mean of the observed value.

5.3 Results and discussion

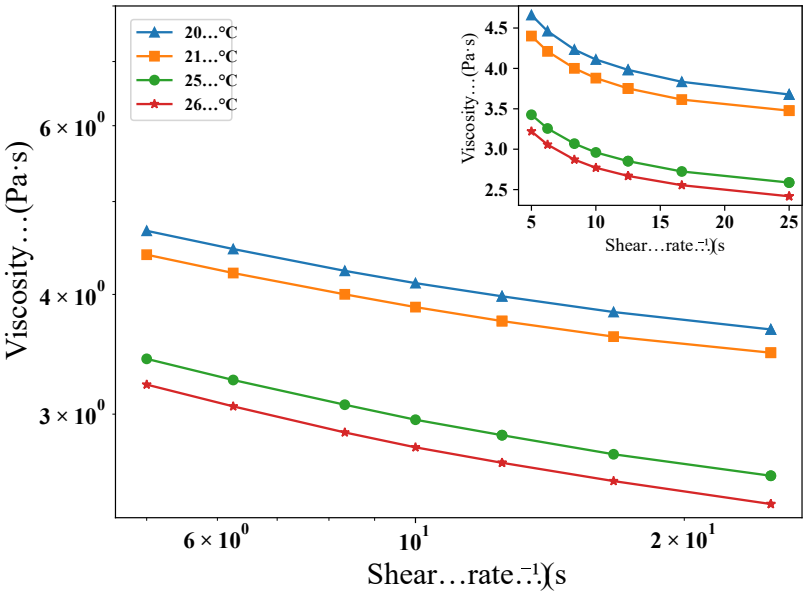

Figure 5.4. Viscosity curves of the slurry at varied temperatures: 20 °C, 21 °C, 25 °C, and 26 °C. All measurements were concentrated on the shear-rate range corresponding to my experiments during the tape-casting process. The main plot shows the viscosity curves on a double logarithmic scale, while the inset displays the curves on a linear scale.

5.3.1 Rheological characterisation

During the tape-casting process, the slurry is subjected to a shear rate. This shear rate can be approximated as the ratio of the casting speed to the doctor blade gap. Thus, for non-newtonian fluids such as casting slurries used in this study, the viscosity

changes resulting from the changes in the shear rates or doctor blade gaps will alter the fluid mechanical conditions during tape casting, eventually affecting the thickness and uniformity of the green tape. The rheological characterisation of the slurry is shown in Figure 5.4, illustrating the dependence of viscosity upon shear rate at four different temperatures: 20, 21, 25, and 26 °C. These viscosity curves give information about the shear-rate range used for the experiments throughout the tape-casting process. In general, the viscosity decreases as the shear rate increases, indicating that the slurry exhibits shear-thinning, also known as pseudoplasticity, behaviour [120, 121]. Furthermore, Figure 5.4 also highlights that temperature has an impact on the viscosity of the slurry. Specifically, the viscosity of the casting slurry decreases as the temperature increases. For instance, at the fixed shear rate, the viscosity at 20 °C is higher than that of 21, 25 and 26 °C (Figure 5.4). Since the viscosity reflects the flow behaviour of the slurry, these understandings are critical for controlling the flow characteristics of the slurry, which directly impacts the tape casting process and the quality of the resulting green tape.

5.3.2 Exploratory data analysis

5.3.2.1 Tape casting

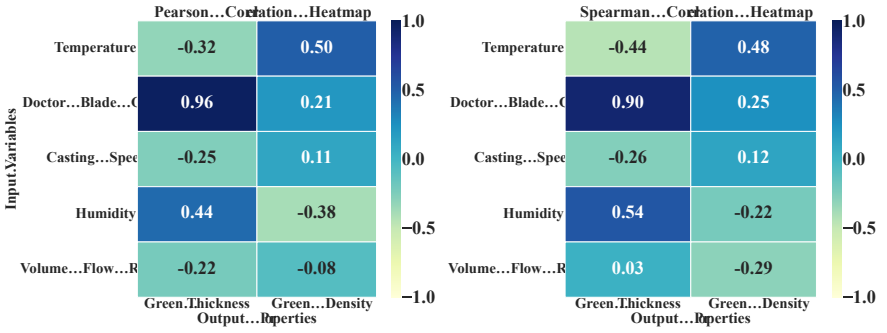

(a) *Pearson method* **(b)** *Spearman method*

Figure 5.5. Correlation heatmap between key manufacturing parameters and the relevant outputs for the tape-casting process, ranging from -1 (perfect negative correlation) to 1 (perfect positive correlation), where 0 implies no correlation: (a) Pearson correlation heatmap between manufacturing parameters and the physical properties of the green tape, and (b) Spearman correlation heatmap between manufacturing parameters and the physical properties of the green tape.

A combination of Pearson and Spearman correlation methods is commonly used to detect both types of relationships that might not be captured through a single method, enabling us to gain a more comprehensive understanding of the correlations between process parameters and the physical properties of the green tape. Figure 5.5 shows

the Pearson and Spearman correlation coefficient between the process parameters and the output properties of the green tape, revealing physical meaningful trends. In general, both correlation methods are consistent for all pairs except for pairs of volume flow rate and the outputs. Specifically, the correlation heatmap shows strong positive correlations between the doctor blade gap and the green thickness in terms of Pearson correlation ($\rho_p = 0.96$) and Spearman correlation ($\rho_s = 0.90$), indicating that the doctor blade gap directly controls the tape thickness with a near-linear physical relationship. This confirms the fundamental physical principle where the higher doctor blade gap leads to the thicker green tape [92, 178]. The impact of the doctor blade gap on the green density is much weaker than the impact on the green thickness. Casting speeds exhibit a weak influence on green thickness ($\rho_p = -0.25$ and $\rho_s = -0.26$) and a negligible impact on green density ($\rho_p = 0.11$ and $\rho_s = 0.12$). This indicates that the faster casting speed predominantly results in the thinner tape [179, 180]. Similar to casting speed, temperatures show negative correlations with green thickness ($\rho_p = -0.32$ and $\rho_s = -0.44$) and positive correlations with green density ($\rho_p = 0.50$ and $\rho_s = 0.48$). Nevertheless, the impact of the temperature on the physical properties of the green tape is stronger than the casting speeds, indicating the importance of the temperature in producing the green tape using the KAROcast tape-casting device. Additionally, humidity shows positive correlations with green thickness ($\rho_p = 0.44$ and $\rho_s = 0.54$), illustrating a nonlinear relationship. In contrast, the correlation heatmap shows that humidity is a factor in decreasing the green density of the green tape. The inconsistent correlation for exhaust air volume flow rate between Pearson and Spearman correlation coefficient implies that the impact of this factor is not straightforward and difficult to capture using standard correlation analysis. This complexity may result from its dependence upon the impact of other manufacturing conditions, particularly temperature and humidity. Indeed, the temperature, humidity, and exhaust air volume flow rate are frequently interconnected within the tape-casting process (Figure S1). Therefore, changes in temperature or humidity may result in fluctuations in the exhaust air volume flow rate inside the tape-casting machine. The correlation heatmaps among process parameters, along with scatter plots illustrating the relationship between process parameters and green tape properties, are provided in Appendix C (Figures C.1 and C.2).

5.3.2.2 Sintering and reduction

The evolution of the sample properties after the sintering and reduction process was investigated by using scatter plots (Figure 5.6). Figure 5.6a demonstrates a strong linear correlation between green thickness and sintered thickness, confirming that the green samples with higher thickness lead to the thicker sintered thickness after sintering in the same conditions. Meanwhile, although Figure 5.6b displays the increasing trend for the density of the sample after sintering, the scatter plot of green density and sintered density is more scattered. This dispersion explains differences in initial green density as well as complex material transformations throughout the sintering process.

During the reduction process, the thickness change is quite minimal, and a strong linear relationship is also observed in thickness transitions between the sintering and reduction stages (Figure 5.6c). Figure 5.6d indicates that the density after reduction is slightly lower than the sintered density due to the reduction of NiO to Ni, and the sintered samples with higher density will retain the higher density in the reduced state. These results are physically expected and show that the sintering quality is crucial for the final microstructure.

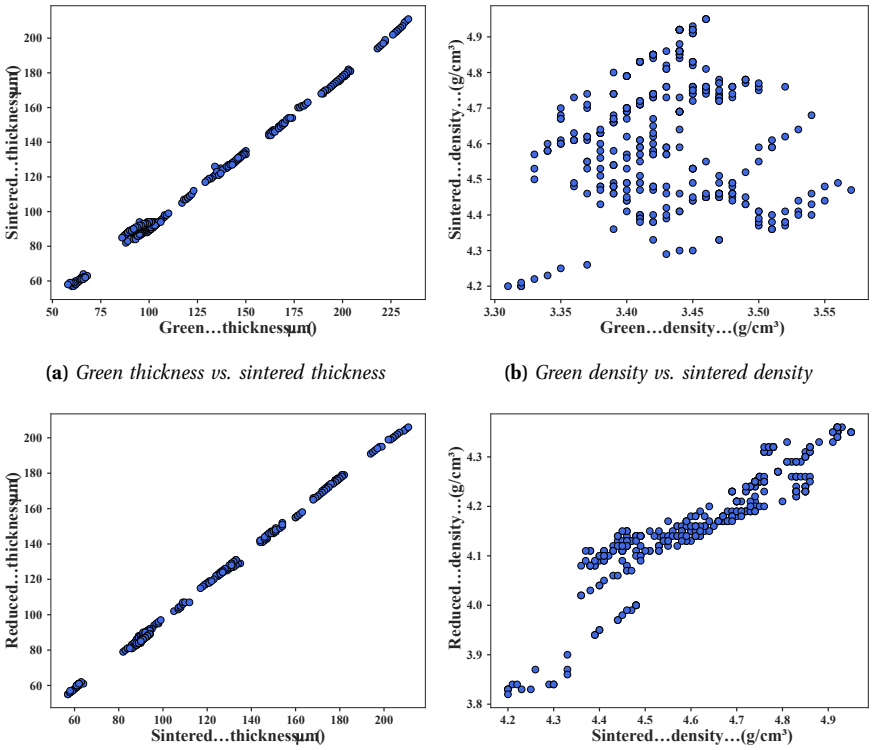

(a) *Green thickness vs. sintered thickness*

(b) *Green density vs. sintered density*

(c) *Sintered thickness vs. reduced thickness*

(d) *Sintered density vs. reduced density*

Figure 5.6. Scatter plots representing the relationship of tape properties after sintering and reduction process: (a) Green thickness and sintered thickness, (b) Green density and sintered density, (c) Sintered thickness and reduced thickness, and (d) Sintered density and reduced density.

5.3.3 Machine learning performance

Several regressors were explored and evaluated to predict the thickness and density for each manufacturing stage, namely Ridge Regression, Support Vector Regression,

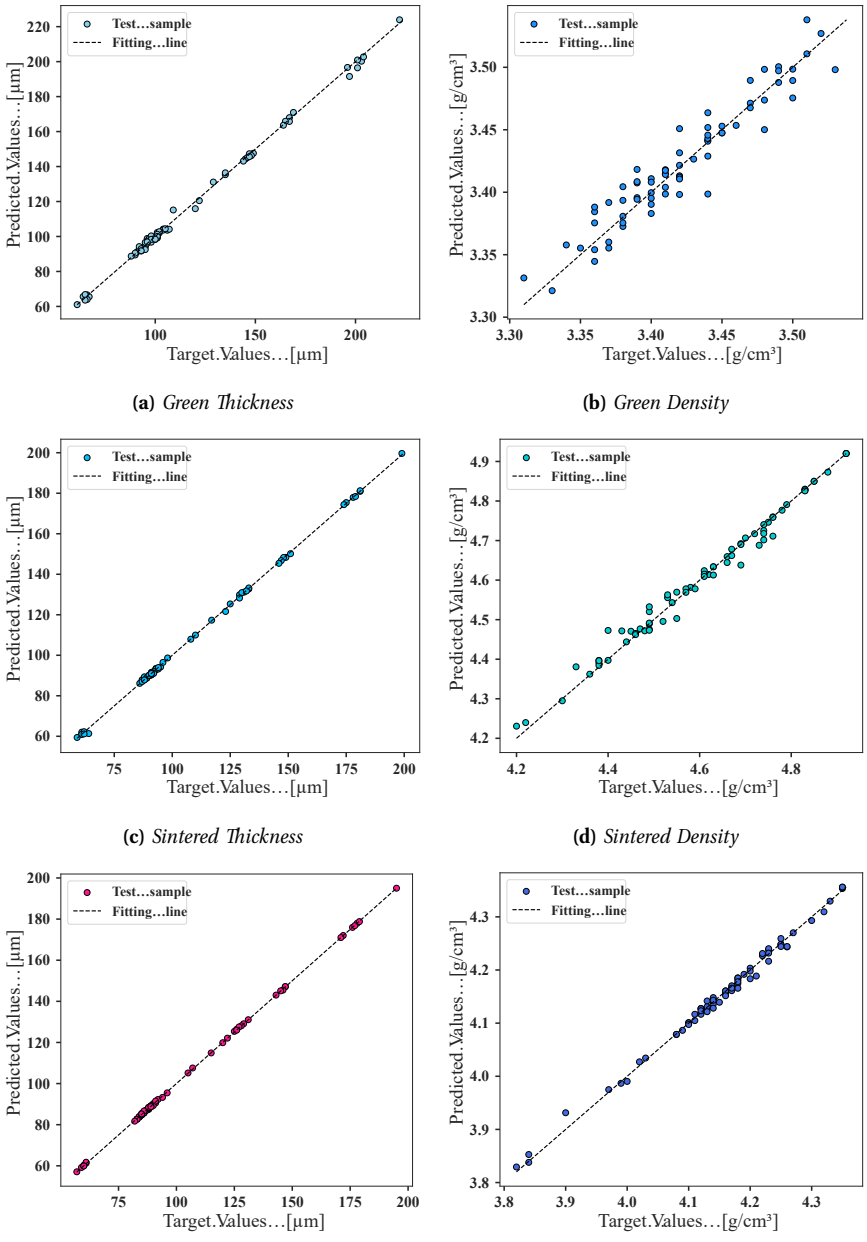

(a) *Green Thickness* **(b)** *Green Density*

(c) *Sintered Thickness* **(d)** *Sintered Density*

(e) *Reduced Thickness* **(f)** *Reduced Density*

Figure 5.7. Comparison plots of predicted values against target values for physical properties of the tape at different manufacturing stages: (a) Green Thickness, (b) Green Density, (c) Sintered Thickness, (d) Sintered Density, (e) Reduced Thickness, and (f) Reduced Density.

Random Forest, Extra Trees, and Gradient Boosting. Among them, the Extra Trees regressor exhibits robust predictive performance for both green thickness and green density with R^2 scores of 0.99 and 0.91, respectively. This explains the nature of the dataset. In fact, the correlation assessment results suggest that the tape-casting dataset exhibits both multicollinearity and non-linear relationships between process parameters and green tape properties. Tree-based models are particularly well-suited for this type of data, as they can capture complex non-linear patterns and remain robust in the presence of multicollinearity [181]. Moreover, these models are less sensitive to non-normal feature distributions and do not require feature scaling [182, 183], which is advantageous when working with raw experimental datasets. This explains why tree-based algorithms such as Extra Trees demonstrated strong predictive performance in modelling the tape-casting process.

In the sintering and reduction stages, Ridge regression with L2 regularisation demonstrated excellent performance, achieving an R^2 score of 0.99 in predicting thickness and density in the reduced state. Nonetheless, the Extra Trees Regressor remained the best-performing model for predicting sintered thickness and density with R^2 scores of 0.99 and 0.98, respectively. This is mainly due to the complexity of material behaviour throughout heat treatment. Figure 5.7 illustrates regression plots comparing the target values to the predicted values to assess the accuracy of developed ML models for each prediction task. It can be observed that most of the predicted values align well with the target data points, indicating high prediction accuracy of the models. The performance of the optimised ML models for each stage of the SOC support manufacturing process is summarised in Table 5.2. Each row represents a specific prediction task with respect to the corresponding stage, detailing the selected optimal algorithm and its performance metrics on the independent testing set.

Table 5.2. Performance of optimised machine learning models for SOC support fabrication stages on the independent testing set. All models showed strong predictive accuracy, with R^2 scores consistently exceeding 0.9 for all tasks, indicating that the majority of the variance in unseen data could be explained. The MAE and RMSE values are expressed in the unit of each output (e.g., thickness in µm, density in g/cm^3). Thus, these errors are relatively small compared to their actual measurement scales.

Process Stage	Predicted Output	Optimal Algorithm	R^2	MAE	RMSE
Tape Casting	Green Thickness	Extra Trees	0.99	1.327	1.780
	Green Density	Extra Trees	0.91	0.012	0.015
Sintering	Sintered Thickness	Extra Trees	0.99	0.397	0.588
	Sintered Density	Extra Trees	0.98	0.013	0.021
Reduction	Reduced Thickness	Ridge regression	0.99	0.237	0.306
	Reduced Density	Ridge regression	0.99	0.006	0.008

5.3.4 Impact of manufacturing parameters on material physical properties

As already mentioned above, in addition to the known influences of the doctor blade gap and casting speed, condition parameters such as temperature, humidity, and exhaust air volume flow rate also have crucial roles to play in determining the final properties of the green tape in this study. These factors often exert simultaneous effects on the tape rather than acting in isolation. To further analyse the combined impacts of these three parameters on the tape properties, I analyse the tapes produced using a consistent doctor blade gap of 300 µm, a casting speed of 5 $\mathrm{mm/s}$, the same supply and exhaust fan speeds, and a consistent initial temperature setting on the tape casting machine. Since these tapes were fabricated at different times, the humidity levels varied with each experiment. This ensures the reliability of comparisons and analysis regarding the subtle, yet often hard-to-detect, influence of humidity.

Figure 5.8 illustrates the influence of three manufacturing parameters on the tape properties across three manufacturing stages: tape casting, sintering, and reduction process. The data are visualised using boxplots alongside point plots, providing comprehensive insights about data distribution and central tendency for each condition group. Specifically, in the tape-casting stage, both thickness and density demonstrate variations according to temperature, humidity, and exhaust air volume flow rate. The "Low-High-High" condition yields the highest mean green thickness, while the "High-High-High" condition results in the lowest mean thickness. Conversely, green density generally increases across the conditions, with the "Low-Low-High" condition exhibiting the highest mean green density. Figures 5.8a and 5.8b offer valuable insights for optimising the tape casting process. For instance, if the goal is to produce tapes with higher green thickness, the "Low-High-High" condition may be preferred, despite the resultant lower green density. Conversely, for achieving the higher density, the "Low-Low-High" condition represents a suitable option. Meanwhile, to attain a balance of relatively higher mean values and less variability for both green thickness and density, it could be considered to control the condition to "High-High-High", "High-High-Low", and "High-Low-Low".

In the sintering and reduction stages, initial manufacturing conditions indirectly affected the properties of the sintered and reduced tapes through tape casting. This indirect effect suggests a strong retention of characteristics from the green tape stage into subsequent processing. Analysis of Figure 5.8c and Figure 5.8e confirms that tape thickness consistently decreased across all experimental groups after both the sintering and reduction processes. Notably, the change in thickness between sintered and reduced tapes was minor when compared to the more significant thickness transformation observed between the green and sintered tapes. Furthermore, Figures 5.8d and 5.8f illustrate a substantial increase in tape density following the sintering process, while a slight decrease in density was observed after the reduction stage. By comprehensively analysing tape properties, including thickness and density, across all three stages (green, sintered, and reduced tape) in relation to temperature, humidity, and volume flow rate, the results indicate that the "High-High-Low" condition

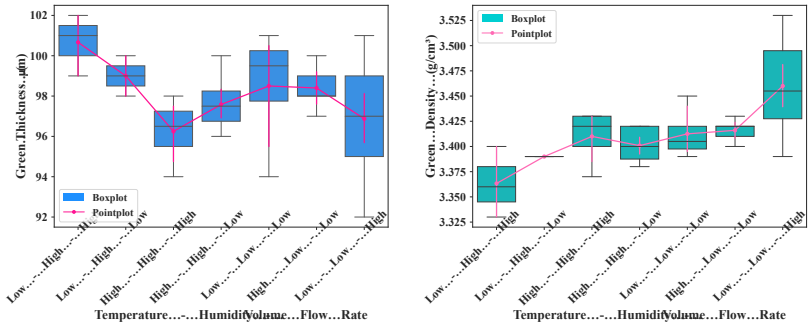

(a) *Green Thickness*

(b) *Green Density*

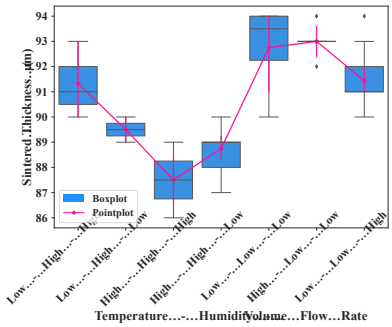

(c) *Sintered Thickness*

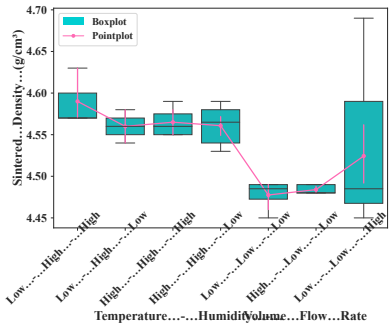

(d) *Sintered Density*

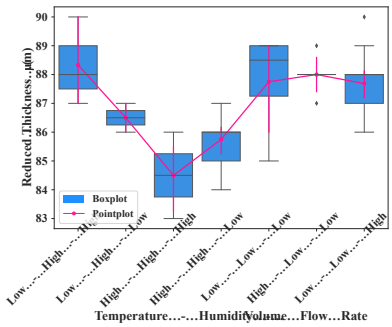

(e) *Reduced Thickness*

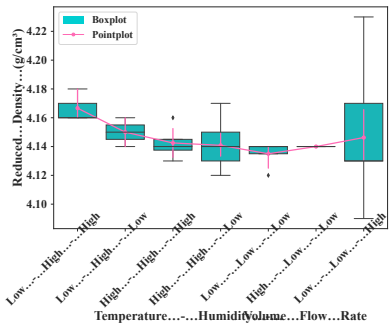

(f) *Reduced Density*

Figure 5.8. Analysis plots demonstrating the impact of three-manufacturing-parameter combinations (e.g. temperature, humidity and exhaust air volume flow rate) on (a) Green Thickness, (b) Green Density, (c) Sintered Thickness, (d) Sintered Density, (e) Reduced Thickness, and (f) Reduced Density. The boxplots compare various condition groups. Point plots represent the mean value and the tendency, accompanied by its 95% confidence interval. All analyses were implemented for the tapes produced using the same doctor blade of 300 µm and the casting speed of 5 mm/s. The investigated temperature, humidity and volume flow rate in the exhaust air varied in the ranges of 22.4–33.9 °C, 29–50 %, and 69.05–74.48 m^3/h, respectively.

consistently yields higher values and lower variability for both thickness and density. Nevertheless, if the primary objective is to achieve tapes with exceptionally high thickness and density, irrespective of their variability, the "Low-Low-High" condition merits consideration.

5.3.5 Density evolution during fuel electrode support fabrication

Figure 5.9 illustrates the evolution of the average density across various stages: slurry, green tape, sintered tape and reduced tape. Despite differences among the individual tape samples, a consistent trend was observed across all cases. Therefore, a single regression curve was fitted to represent the overall behaviour. Overall, it is obvious that the density underwent significant changes during fabrication. Specifically, the density was lowest at around $2.19\ \mathrm{g/cm^3}$ in the slurry stage. After tape casting and drying, the density achieved a value within a range of 3.33 and $3.55\ \mathrm{g/cm^3}$ depending upon the manufacturing conditions and parameters in this study. This results from the solvents evaporating and the material particles undergoing closer packing. During the sintering at 1400 °C, the binder and organic additives were completely burned off, while particles fused into a solid coherent mass. As a result, the tape experiences a significant increase in density, reaching values in the range of 4.22 and $4.87\ \mathrm{g/cm^3}$. Finally, the reduction of NiO to Ni results in a slight decrease in density caused by oxygen loss, with the final density ranging from 3.84 to $4.34\ \mathrm{g/cm^3}$. The figure provides a clear visualisation of the physical transitions in density throughout the manufacturing stages, highlighting the consistency of the process.

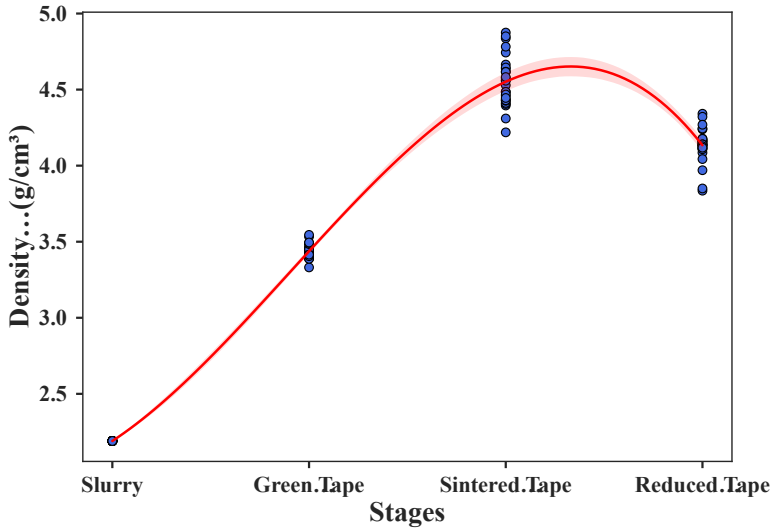

Figure 5.9. Density evolution during fuel-electrode support manufacturing stages.

5.4 Conclusions and Perspectives

This chapter presented a data-driven machine learning framework to predict the thickness and density of the fuel electrode support across various fabrication processes, namely tape casting, sintering, and reduction processes. Viscosity measurements at various temperatures were employed to investigate the impact of temperature on the rheological properties of the slurry. The dataset was collected experimentally from the automated logging system of the tape casting machine via ELN and physical measurements, enabling ML to be applied to ceramics tape casting for the first time. The experimental data were analysed to detect the relationship between the manufacturing conditions and physical properties of the green tape, especially the direct impact of temperature, humidity and exhaust air volume flow rate on green thickness and green density, which indirectly affects the thickness and density of the sintered and reduced tape. Therefore, it is worth noting that the tape casting process could be optimised if humidity and exhaust air volume flow rate inside the machine can be tracked and controlled.

The reported work further indicates that the thickness and density of the fuel-electrode support for each manufacturing process can be predicted with high accuracy by using ML models trained on high-quality data from the experiment. Although the current study utilised semi-automated data collection, which included extracting log files from the tape casting machine and manually measuring sample properties, the developed ML models still exhibited strong predictive performance. Nevertheless, the overall accuracy of ML models can be further enhanced, provided that a comprehensive automated data acquisition process is implemented to reduce potential human error in practice. Developing the automated data acquisition pipeline coupled to an ML framework will not only enhance the predictive performance but also allow the development of models to optimise the manufacturing process.

In the era of smart manufacturing, a promising direction for future research lies in the integration of data-driven ML approaches into the manufacturing pipeline of fuel-electrode supports as well as other components of SOCs. As a first step toward automation, the ELN, specifically eLabFTW, has been successfully integrated into the KAROcast tape casting system to automatically collect process data. To fully realise the benefits of ML integration, it is essential to establish a fully automated infrastructure for acquiring high-quality, diverse data from each stage of the manufacturing process. Moving forward, physical measurements should also be automated and ideally conducted using non-contact methods to improve both measurement precision and accuracy, thereby enhancing the overall data quality. Coupling automated data acquisition with ML offers significant potential for predicting material properties, and thus enables better decision-making throughout the manufacturing workflow [184]. Such an end-to-end automated pipeline would minimise human-induced error and enable large-scale collection of high-quality data with diverse input parameters. This provides a solid foundation for training robust ML models capable of optimising the fabrication process of SOC component layers more intelligently and efficiently.

6

Overall conclusions and outlook

6.1 Overall conclusions

This thesis presents the results obtained from the modelling for the SOC fuel-electrode substrate manufacturing, including coarse-grained physics-based modelling for tape casting of the substrate (Chapter 3), hybrid modelling of the slurry for the tape casting of the fuel-electrode substrate (Chapter 4), and ML modelling for the fabrication of fuel-electrode substrates from tape casting and drying to sintering and reduction (Chapter 5). These novel approaches were developed for the SOC substrate as part of the ARTISTIC and ML4SOC projects, a collaborative effort between UPJV/LRCS (France) and IMD-2, FZJ (Germany). The work has shown that physics-based and data-driven approaches address different aspects of the same challenge, and that their integration is key to achieving systematic and reproducible optimisation of the fabrication process.

Chapter 3 focuses on developing a physics-based modelling framework for SOC manufacturing, with research emphasis upon the tape casting and drying of the fuel-electrode substrate. Building upon previous work from my research group at UPJV (France), where the DEM was successfully applied to model various battery manufacturing processes, including both liquid electrolyte lithium-ion and all-solid-state batteries, this study adapts and extends the methodology to SOCs. The aim is to establish a proof-of-concept model that directly links manufacturing parameters to the resulting microstructure of the substrate.

The 3D physics-based modelling reported in Chapter 3 offers a balanced approach, bridging the gap between resource-intensive experimental imaging (e.g., X-ray CT, FIB/SEM) and stochastic methods. They provide a more fundamentally grounded predictive capability than the latter, with significantly higher throughput than the former. This capability underpins the DEM framework developed here, providing a

physically consistent representation of the substrate microstructure at relevant steps of tape casting and drying.

To achieve this, initial experimental data were collected at IMD-2, FZJ (Jülich, Germany), including slurry composition and formulation details. These data were used for the DEM modelling for the sequential manufacturing steps (e.g. slurry preparation, tape casting and drying) using the MatriCS High Performance Computing platform at UPJV (Amiens, France), closely reflecting the actual experimental procedure. This model was calibrated using in-house experimental data, such as the slurry density, the slurry viscosity, as well as the density and porosity of the resulting green tape. This ensures that the simulations matched real manufacturing conditions. The DEM simulations confirmed the uniform distribution of all materials within the dried microstructure, which is expected before thermal processing. Although the model assumes homogeneous drying of BDPD particles, a simplification of actual behaviour, it captures the key mechanisms, trends relevant for the drying stage, and the proof-of-concept objectives.

This study demonstrates that the ARTISTIC workflow is not restricted to batteries but can also be applied to SOC technologies. Incorporating additional imaging and characterisation data will further improve understanding of processing and performance relationships. Despite simplifications such as spherical particle representation, this method constitutes, to my knowledge, the most comprehensive computational framework currently available for linking manufacturing parameters with microstructural characteristics of the fuel-electrode substrate. It also provides a predictive tool for optimising the casting process and exploring production scenarios prior to experimental trials. Consequently, Chapter 3 establishes a strong foundation for physics-based modelling of SOC fabrication. It provides a flexible computational strategy that can accelerate the design and scale-up of energy conversion devices, laying the groundwork for the analyses and studies presented in the following chapters.

Building upon this foundation, Chapter 4 introduces a hybrid surrogate modelling framework to address the high computational cost associated with physics-based DEM simulations of the solvent-based slurry, particularly the repeated fitting of FF parameters for large simulation domain sizes required to ensure agreement with experimental data. By integrating data-driven DL techniques with physics-based modelling, this chapter aimed to develop a hybrid approach for the slurry simulation that maintains accuracy while significantly reducing computational requirements.

The workflow began with generating a slurry microstructural dataset using the DEM simulations of slurry preparation for tape casting reported in Chapter 3. These data were then utilised to train the DL model, particularly the modified VGG16 network, capable of predicting the final slurry microstructures of the substrate in FESCs. In order to preserve physical interpretability and ensure accuracy, the predicted microstructures were further equilibrated using DEM simulations. This created a hybrid framework that combines the strengths of both physics-based and data-driven approaches. The trained model achieved strong predictive performance, as indicated by high R^2 and low MSE as well as MAE values during training. The physical fidelity of the predicted microstructures was further verified through RDF analyses. Moreover,

the model exhibited adaptability when tested on different slurry microstructures, with good agreement between predicted and simulated microstructures. Some deviations were observed, particularly for thicker slurry layers, suggesting directions for future refinement. Despite these limitations, the modified VGG16 architecture proved to be a robust neural network for hybrid modelling of the substrate manufacturing processes, particularly the slurry preparation stage. The developed workflow highlights the potential of data-driven surrogate modelling to substantially accelerate validation and optimisation tasks that would otherwise depend upon computationally intensive physics-based simulations. This work represents an important step toward scalable and computationally efficient modelling strategies for energy conversion device manufacturing.

Chapter 5 presents a data-driven ML approach to predict the thickness and density of the fuel-electrode substrate across three key stages of the fabrication process: tape casting and drying, sintering, and NiO reduction. The focus of this chapter shifts from the physics-based modelling framework developed for the SOC substrate using the workflow of the ARTISTIC research initiative led by Prof. Dr. Alejandro A. Franco at UPJV (Amiens, France) to data-driven modelling applied to fully experimental datasets within the ML4SOC project led by Prof. Dr. Olivier Guillon at IMD-2, FZJ (Jülich, Germany).

The effect of temperature on the rheological properties of the slurry was examined through rheological measurements conducted at various temperatures, revealing that higher temperatures lead to lower slurry viscosity. This finding highlights the critical role of temperature in controlling the flow behaviour of the slurry, which directly affects the quality of the green tape after tape casting and drying.

To ensure the consistency of experiments, systematic data management, and high data quality, an enhanced data collection strategy was implemented. This included the integration of the ELN for automatic *in-situ* acquisition of process parameters during tape casting and drying, complemented by on-site characterisation of the resulting tapes.

The developed ML models exhibited strong predictive performance, with R^2 values exceeding 0.9, and small MAE as well as RMSE compared to the experimental measurement scales of each target variable. Analysis of the experimental data demonstrated the influence of otherwise difficult-to-monitor manufacturing parameters, such as temperature, humidity, and exhaust air volume flow rate inside the tape-casting machine, on the substrate properties. These findings highlight a practical pathway to reduce trial-and-error in SOC manufacturing and to enable data-guided process optimisation and scale-up.

Taken together, the physics-based and data-driven strategies developed in this thesis complement each other. The DEM simulations provide physical insight and predictive capability at both the process and microstructural levels, while also generating physically consistent synthetic data that can enrich experimental datasets. Meanwhile, the ML models offer rapid and adaptive ways to uncover hidden trends within complex manufacturing data, thereby supporting decision-making for data-driven experimental

optimisation. The combination of both approaches establishes a framework that integrates numerical modelling, experimental production, and data science. Through this integration, this thesis provides a foundation for scalable, reproducible, and energy-efficient manufacturing of SOC fuel-electrode substrates. The prime contributions of the thesis can therefore be summarised as the development of new modelling tools, the integration of simulations and experiments into coherent workflows, and the application of ML to practical manufacturing challenges. Overall, the thesis demonstrates how such a combined strategy can support more systematic, reproducible, and energy-efficient production of SOCs, and at the same time provide pathways for scaling the technology towards industrial applications.

6.2 Outlook

The studies presented in this thesis have primarily focused on the fuel-electrode substrate, yet the developed methodologies and analytical frameworks can be applied to other components of SOCs and to a variety of material layers in the field of energy storage and conversion devices. Such extensions would allow a more comprehensive understanding of how manufacturing parameters influence the structural and functional properties of the entire cell, ultimately contributing to the optimisation of SOC materials as a whole.

While physics-based models enable extrapolative predictions grounded in mechanistic understanding, they remain computationally expensive [23, 25, 26]. In contrast, data-driven models offer rapid prediction capabilities but are typically constrained to interpolation within known data spaces. The current hybrid modelling framework combines the DL model with the DEM simulation at the workflow level. This framework should continue to be refined and expanded to other fabrication processes. For instance, coupling DEM-generated microstructures directly with ML/DL surrogates, using multiple formulations and corresponding calibrated FFs, could enhance both accuracy and generality. This allows researchers to generate a great deal of synthetic microstructures used for analysis purposes or to serve as inputs for the multiscale modelling associated with subsequent manufacturing stages. Future research could advance toward a deeper coupling in which physical principles are embedded directly into the learning process. Such physics-informed ML/DL approaches would retain the interpretability and rigour of physical modelling while benefiting from the scalability and adaptability of data-driven learning. This enables physics-informed ML/DL models to reliably predict critical properties of the SOC component layers (e.g. material properties, electrochemical characterisation, and the overall cell performance) for both interpolation and extrapolation.

Meeting the challenges of SOC manufacturing requires more than advances in materials science and processing technology. It also demands the integration of data-driven methods into design and optimisation pipelines, serving as a basis for predictive control and continuous process improvement. The incorporation of active learning strategies could further allow simulations and experiments to inform each

other more efficiently, guiding the design of new experiments and accelerating model improvement [185, 186]. These developments could lead to more autonomous, intelligent systems capable of accelerating materials and manufacturing process discovery in a physically meaningful way.

To ensure the reliability of these ML/DL models across laboratory and industrial environments, it will be of utmost importance to establish robust experimental and data infrastructures that ensure the quality, traceability, and interoperability of information. Hence, it will be essential to integrate advanced *in-situ* characterisation into automated high-throughput data pipelines. This would enable continuous feedback between experiments, simulations, and model training, thereby maintaining consistency and traceability of data. Such a data-centric ecosystem would not only facilitate model validation but also enrich ML/DL datasets, strengthening the bridge between physics-based and data-driven approaches. Consequently, this provides a solid foundation for developing interpretable and efficient digital twins of SOC manufacturing processes. Prof. Dr. Alejandro A. Franco's group research led to the demonstration of a pionneering modelling platform paving the way towards digital twins of energy device manufacturing processes.

In the bigger picture of SOC manufacturing within the era of smart manufacturing, a large amount of SOC manufacturing data can be generated throughout manufacturing with the support of key technologies involved in intelligent manufacturing (e.g. Internet of Things-enabled infrastructures, advanced sensors and robotics, cyber-physical systems, cloud computing, and big data analytics) [187]. Therefore, advanced data collection and analysis in data-driven manufacturing processes are essential in Industry 4.0, where automation, digitalisation, and data integration form the foundation for intelligent process control [184, 188, 189]. In this regard, digital twins of SOC manufacturing processes link physical and virtual systems in a continuous feedback loop [26, 128], effectively bridging the gap between laboratory research and industrial production. This capability may support the acceleration of SOC industrialisation by enabling predictive control, real-time monitoring, and scalable process optimisation.

Looking forward, by integrating physics-based and data-driven modelling frameworks with advanced experimental infrastructures, the digital ecosystem can evolve to support more intelligent and adaptive manufacturing processes. Researchers and operators would be capable of interacting with data-driven systems more transparently and adaptively, paving the way toward Industry 5.0, where sustainability, resilience, and human–machine collaboration become central [189, 190]. These advances point toward a future where SOC components are produced through the manufacturing ecosystem that are intelligent, sustainable, and genuinely human-centred. Collectively, these developments represent a meaningful step toward digitally interconnected, adaptable, and resilient manufacturing ecosystems for future SOC material applications.

A

Supplementary information for chapter 3

A.1 Particle size distribution of the material particles

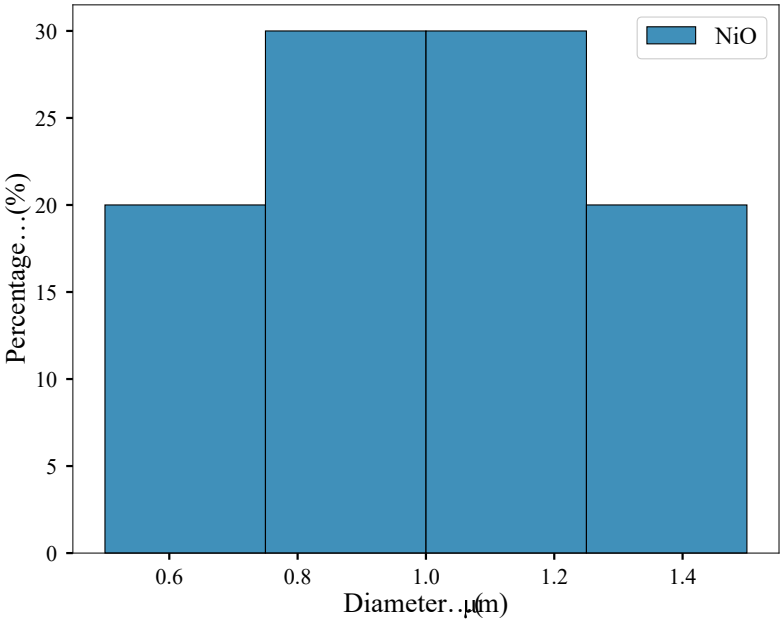

Figure A.1. Particle size distribution of NiO used for the initial simulation configuration.

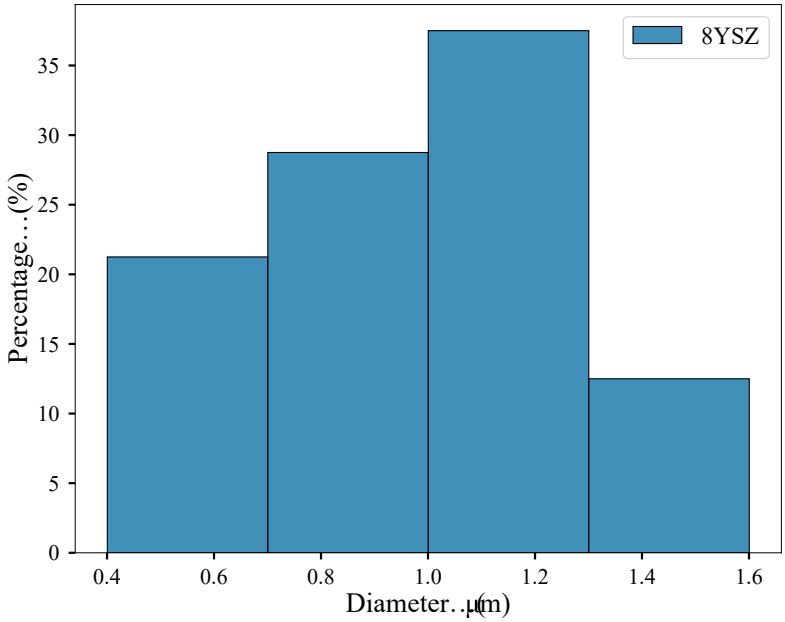

Figure A.2. Particle size distribution of 8YSZ used for the initial simulation configuration.

A.2 Force field parameters

Table A.1. Force field parameters adopted in DEM simulations.

	Parameters	Slurry phase	Drying phase
LJFF	$\epsilon_{\text{NiO}}\ [\text{pg}\,\mu\text{m}^2\,\mu\text{s}^{-2}]$	$9.5 \times d_{\text{NiO}}$	$200 \times d_{\text{NiO}}$
	$\sigma_{\text{NiO}}\ [\mu\text{m}]$	$0.85 \times d_{\text{NiO}}$	$0.89 \times d_{\text{NiO}}$
	$r_{c\ \text{NiO}}\ [\mu\text{m}]$	$1.5 \times d_{\text{NiO}}$	$1.1 \times d_{\text{NiO}}$
	$\epsilon_{\text{8YSZ}}\ [\text{pg}\,\mu\text{m}^2\,\mu\text{s}^{-2}]$	$9 \times d_{\text{8YSZ}}$	$200 \times d_{\text{8YSZ}}$
	$\sigma_{\text{8YSZ}}\ [\mu\text{m}]$	$0.8 \times d_{\text{8YSZ}}$	$0.85 \times d_{\text{8YSZ}}$
	$r_{c\ \text{8YSZ}}\ [\mu\text{m}]$	$1.5 \times d_{\text{8YSZ}}$	$1.1 \times d_{\text{8YSZ}}$
	$\epsilon_{\text{BDPD}}\ [\text{pg}\,\mu\text{m}^2\,\mu\text{s}^{-2}]$	0.01	550
	$\sigma_{\text{BDPD}}\ [\mu\text{m}]$	0.6	$0.9 \times d_{\text{BDPD}}$
	$r_{c\ \text{BDPD}}\ [\mu\text{m}]$	2.2	$1.7 \times d_{\text{BDPD}}$
GHFF	$k_n\ [\text{pg}\,\mu\text{m}^{-1}\,\mu\text{s}^{-2}]$	17.5	800
	$\gamma_n\ [\mu\text{m}^{-1}\,\mu\text{s}^{-2}]$	10	50
	μ	0.016	0.05

*d_{NiO}, d_{8YSZ}, and d_{BDPD} refer to the diameters of NiO, 8YSZ, and BDPD particles, respectively.

A.3 Simulated viscosity for two different shear-rates

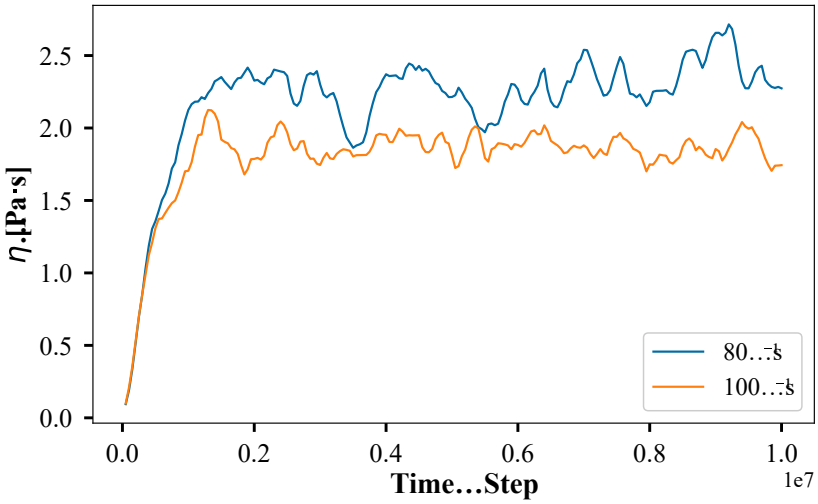

Figure A.3. Viscosity outputs through the non-quilibrium simulation for two different shear-rates, carried out for case 1 of Table A.1.

A.4 DEM microstructure generation

Table A.2. Information of the microstructures generated by the DEM model.

No.	Microstructure type	Number of particles	Volume $[\mu m^3]$	Density $[g/cm^3]$	Porosity $[\%]$
1	Slurry microstructure	14 162	5 408	2.22	N/A
	Dried microstructure		1 296	3.46	9.7
2	Slurry microstructure	14 162	5 408	2.22	N/A
	Dried microstructure		1 296	3.47	9.2
3	Slurry microstructure	14 162	5 408	2.22	N/A
	Dried microstructure		1 296	3.44	10
4	Slurry microstructure	14 162	5 408	2.22	N/A
	Dried microstructure		1 296	3.44	10
5	Slurry microstructure	14 162	5 408	2.22	N/A
	Dried microstructure		1 296	3.45	9.6
6	Slurry microstructure	226 568	77 312	2.22	N/A
	Dried microstructure		23 040	3.46	9.4

A.5 Code and data availability

Code and data will be made available upon reasonable request.

B

Supplementary information for chapter 4

B.1 Force field parameters

Table B.1. Force field parameters adopted in DEM simulations.

Parameters		Slurry phase	Drying phase
LJFF	ϵ_{NiO} $[\text{pg}\,\mu\text{m}^2\,\mu\text{s}^{-2}]$	$9.5 \times d_{\text{NiO}}$	$200 \times d_{\text{NiO}}$
	σ_{NiO} $[\mu\text{m}]$	$0.85 \times d_{\text{NiO}}$	$0.89 \times d_{\text{NiO}}$
	$r_{c\ \text{NiO}}$ $[\mu\text{m}]$	$1.5 \times d_{\text{NiO}}$	$1.1 \times d_{\text{NiO}}$
	ϵ_{8YSZ} $[\text{pg}\,\mu\text{m}^2\,\mu\text{s}^{-2}]$	$9 \times d_{\text{8YSZ}}$	$200 \times d_{\text{8YSZ}}$
	σ_{8YSZ} $[\mu\text{m}]$	$0.8 \times d_{\text{8YSZ}}$	$0.85 \times d_{\text{8YSZ}}$
	$r_{c\ \text{8YSZ}}$ $[\mu\text{m}]$	$1.5 \times d_{\text{8YSZ}}$	$1.1 \times d_{\text{8YSZ}}$
	ϵ_{BDPD} $[\text{pg}\,\mu\text{m}^2\,\mu\text{s}^{-2}]$	0.01	550
	σ_{BDPD} $[\mu\text{m}]$	0.6	$0.9 \times d_{\text{BDPD}}$
	$r_{c\ \text{BDPD}}$ $[\mu\text{m}]$	2.2	$1.7 \times d_{\text{BDPD}}$
GHFF	k_n $[\text{pg}\,\mu\text{m}^{-1}\,\mu\text{s}^{-2}]$	17.5	800
	γ_n $[\mu\text{m}^{-1}\,\mu\text{s}^{-2}]$	10	50
	μ	0.016	0.05

*d_{NiO}, d_{8YSZ}, and d_{BDPD} refer to the diameters of NiO, 8YSZ, and BDPD particles, respectively.

B.2 Information of the slurry microstructure generated for Deep Learning model training and validation

Table B.2. Information of the slurry microstructures generated for model training and validation.

Microstructure	Number of particles	Volume $[\mu m^3]$	Size $[\mu m^3]$
1	7 331	4 093.656	$11.8 \times 11.8 \times 29.4$
2	7 331	4 041.756	$11.4 \times 11.4 \times 31.1$
3	7 331	4 110.336	$9.6 \times 9.6 \times 44.6$
4	21 989	12 196.089	$15.3 \times 15.3 \times 52.1$
5	21 989	12 168.602	$16.3 \times 16.3 \times 45.8$
6	7 331	4 060.075	$11.5 \times 11.5 \times 30.7$
7	29 317	16 324.352	$17.6 \times 17.6 \times 52.7$
8	29 317	16 340.91	$17.9 \times 17.9 \times 51.0$

B.3 Information of the slurry microstructure generated for Deep Learning model test

Table B.3. Information of the slurry microstructures generated for model test.

Microstructure	Number of particles	Volume $[\mu m^3]$	Size $[\mu m^3]$
1	7 331	4 093.656	$11.8 \times 11.8 \times 29.4$
2	7 331	4 080.637	$12.7 \times 12.7 \times 25.3$
3	7 331	4 090.572	$11.1 \times 11.1 \times 33.2$
4	14 658	8 096.425	$15.5 \times 15.5 \times 33.7$
5	14 658	8 126.384	$14.8 \times 14.8 \times 37.1$
6	36 646	20 389.537	$21.7 \times 21.7 \times 43.3$
7	29 317	16 360.218	$18.9 \times 18.9 \times 45.8$

B.4 Hyperparameters

Table B.4. Hyperparameters of the CNN model used in Chapter 4.

Hyperparameter	Value
Kernel size	3
Activation (Convolutional & Dense layers)	ReLU
Activation (Output layer)	Linear (None)
Convolution padding	same
Optimizer	Adamax
Learning rate	0.0001
Adamax parameters	$\beta_1 = 0.9$, $\beta_2 = 0.999$, $\epsilon = 10^{-7}$
Batch size	500
Epochs	1 000
Loss function	MSE
Metrics	R^2, MAE

B.5 Code and data availability

Code and data will be made available upon reasonable request.

C

Supplementary information for chapter 5

C.1 Correlation heatmap of process parameters in the tape casting stage

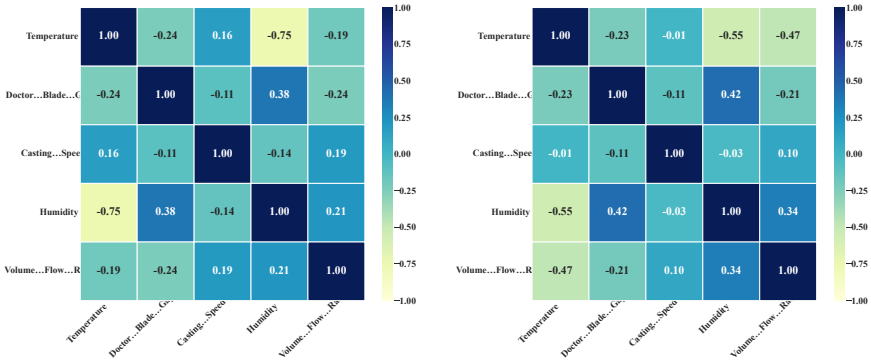

(a) *Pearson method* **(b)** *Spearman method*

Figure C.1. Correlation heatmap between process parameters of tape casting process.

C.2 Scatter plots of tape casting dataset

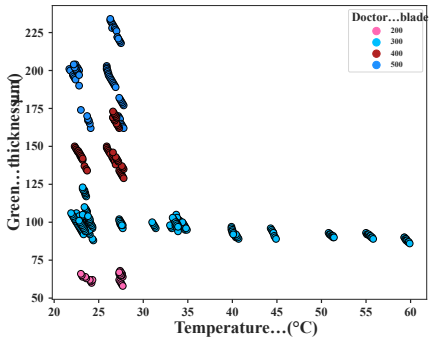

(a) *Temperature vs green thickness*

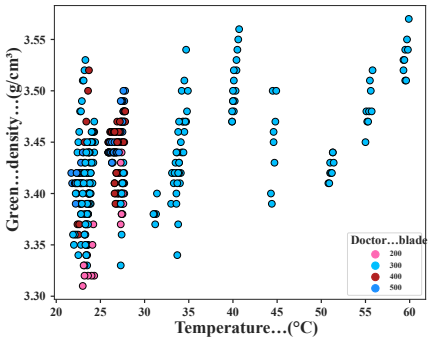

(b) *Temperature vs green density*

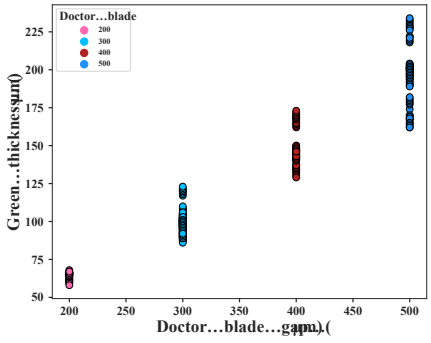

(c) *Doctor blade gap vs green thickness*

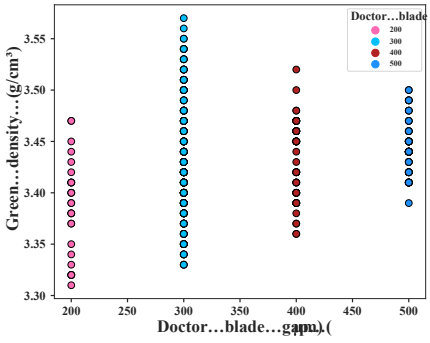

(d) *Doctor blade gap vs green density*

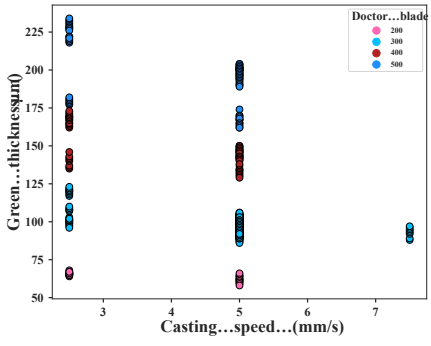

(e) *Casting speed vs green thickness*

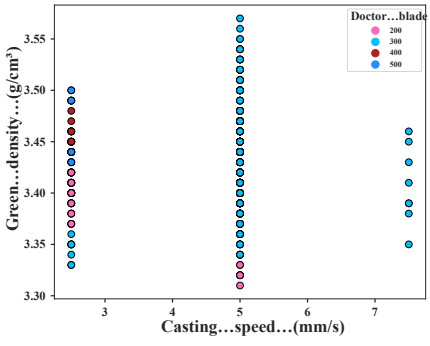

(f) *Casting speed vs green density*

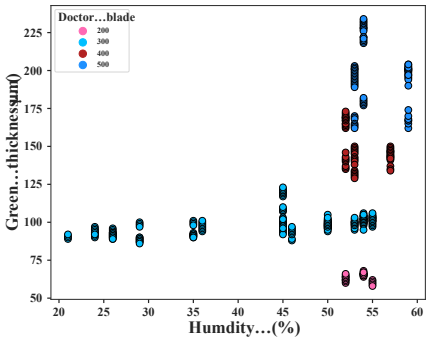

(g) *Humidity vs green thickness*

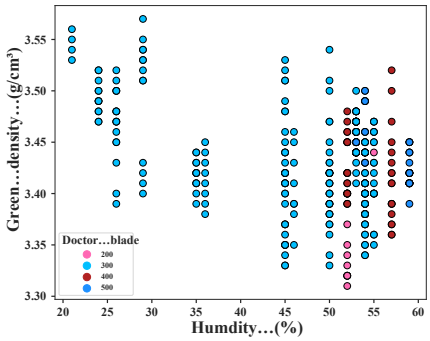

(h) *Humidity vs green density*

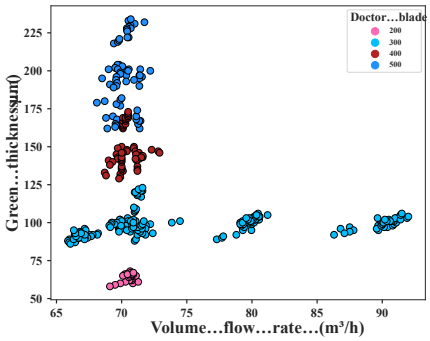

(i) *Exhaust air volume flow rate vs green thickness*

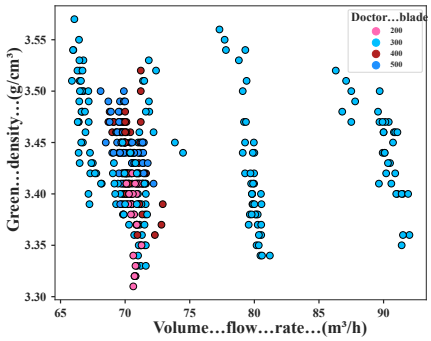

(j) *Exhaust air volume flow rate vs green density*

Figure C.2. Scatter plot of the process parameters and the tape properties showing different groups of doctor blade gap: (a) Temperature vs green thickness, (b) Temperature vs green density, (c) Doctor blade gap vs green thickness, (d) Doctor blade gap vs green density, (e) Casting speed vs green thickness, (f) Casting speed vs green density, (g) Humidity vs green thickness, (h) Humidity vs green density, (i) Exhaust air volume flow rate vs green thickness, and (j) Exhaust air volume flow rate vs green density.

C.3 Thickness evolution during fuel electrode support fabrication

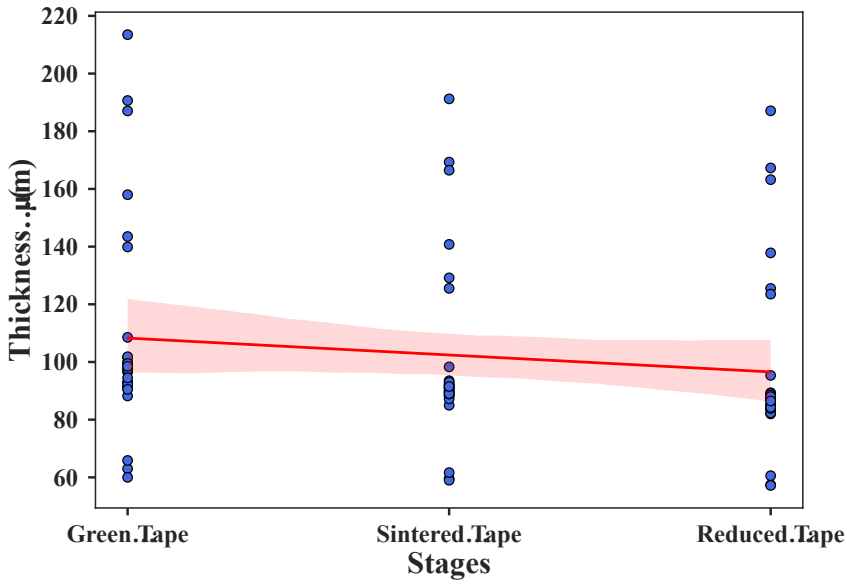

Figure C.3. Thickness evolution during fuel-electrode support manufacturing stages.

C.4 Python code

Python Listing C.1. "model_trainer.py" including utility functions and classes for preprocessing, training, saving and plotting.

```
import numpy as np
import pandas as pd
import matplotlib
import matplotlib.pyplot as plt
from sklearn.pipeline import Pipeline
from sklearn.metrics import r2_score, mean_squared_error,
    mean_absolute_error
import joblib

# ******************* Set plot style ******************
plt.style.use('seaborn-v0_8-white')
matplotlib.use("Agg")
```

```
matplotlib.rcParams.update({
    "font.size": 18,
    "axes.titlesize": 22,
    "axes.labelsize": 25,
    "font.family": "Times New Roman"
})
plt.rc('font', family='Times New Roman', weight='bold')

# ******************* Model trainer class *******************
class ModelTrainer:
    def __init__(self, pipeline: Pipeline, train_set: pd.DataFrame, test_set: pd.DataFrame,
                 target_column: str, input_columns: list, plot_config: dict):
        self.pipeline = pipeline
        self.train_set = train_set
        self.test_set = test_set
        self.target_column = target_column
        self.input_columns = input_columns
        self.plot_config = plot_config
        self.model = None

    def extract_X_y(self, df: pd.DataFrame):
        """Extracting the data for model training"""
        X = df[self.input_columns]
        y = df[self.target_column]
        return X, y

    def train_and_evaluate(self):
        """Train models on the training set and evaluate model on the testing set"""
        X_train, y_train = self.extract_X_y(self.train_set)
        X_test, y_test = self.extract_X_y(self.test_set)

        self.model = self.pipeline.fit(X_train, y_train)
        y_pred = self.model.predict(X_test)

        _r2_score = r2_score(y_test, y_pred)
        mae = mean_absolute_error(y_test, y_pred)
        rmse = np.sqrt(mean_squared_error(y_test, y_pred))
        print(f"Model for {self.target_column}")
        print(f"R2 score for {self.target_column}: {_r2_score:.5f}")
        print(f"MAE score for {self.target_column}: {mae:.5f}")
        print(f"RMSE score for {self.target_column}: {rmse:.5f}")
        self.plot_predictions(y_test, y_pred)

    def save_model(self, path: str):
        """Save model"""
        if self.model:
            joblib.dump(self.model, path)
            print(f"Model saved to {path}")

```

```
    def plot_predictions(self, y_true, y_pred):
        """Plot the regression plots """
        plt.figure(figsize=(8, 7))
        plt.scatter(y_true, y_pred, s=60,
                    color=self.plot_config["color"],
                    edgecolors='k', label="Test sample")
        min_val = min(min(y_true), min(y_pred))
        max_val = max(max(y_true), max(y_pred))
        plt.plot([min_val, max_val], [min_val, max_val],
                 linestyle='--', color='k', label="Fitting line")

        plt.xlabel(self.plot_config["xlabel"])
        plt.ylabel(self.plot_config["ylabel"])
        plt.legend(frameon=True, framealpha=0.8)
        ax = plt.gca()
        ax.tick_params(axis='both', which='major', width=2,
    length=6, pad=8, labelsize=20)
        plt.tight_layout()
        filename = f"trained_models/{self.target_column}"
        plt.savefig(f"{filename}.png", dpi=600)
        plt.savefig(f"{filename}.pdf", dpi=600)
        plt.close()
```

Python Listing C.2. Main script containing the full ML pipeline and model configuration.

```
import os
import pandas as pd
from sklearn.pipeline import Pipeline
from sklearn.ensemble import ExtraTreesRegressor
from sklearn.linear_model import RidgeCV
from sklearn.preprocessing import OneHotEncoder,
    PolynomialFeatures
from sklearn.compose import ColumnTransformer
from model_trainer import ModelTrainer

def create_preprocessor():
    return ColumnTransformer(
        transformers=[
            ('one_hot', OneHotEncoder(drop='first', sparse_output
    =False), ['tape_id'])
        ],
        remainder='passthrough'
    )

def main():
    # Create the new folder--trained_models
    os.makedirs("trained_models", exist_ok=True)

    # Load training & testing sets
    train_df = pd.read_csv("train_data.csv")
    test_df = pd.read_csv("test_data.csv")

    # ============= Pipelines for all models =============
```

```
    pipelines = {
        "green_density": Pipeline([
            ("model", ExtraTreesRegressor(bootstrap=False, max_features=0.95, min_samples_leaf=1, min_samples_split=3, n_estimators=100, random_state=42))
        ]),
        "green_thickness": Pipeline([
            ("model", ExtraTreesRegressor(bootstrap=False, max_features=0.95, min_samples_leaf=1, min_samples_split=3, n_estimators=100, random_state=42))
        ]),
        "sintered_density": Pipeline([
            ("preprocessor", create_preprocessor()),
            ("model", ExtraTreesRegressor(bootstrap=False, max_features=0.95, min_samples_leaf=1, min_samples_split=3, n_estimators=100, random_state=42))
        ]),
        "sintered_thickness": Pipeline([
            ("preprocessor", create_preprocessor()),
            ("model", ExtraTreesRegressor(bootstrap=False, max_features=0.95, min_samples_leaf=1, min_samples_split=3, n_estimators=100, random_state=42))
        ]),
        "reduced_density": Pipeline([
            ("preprocessor", create_preprocessor()),
            ("model", RidgeCV())
        ]),
        "reduced_thickness": Pipeline([
            ("preprocessor", create_preprocessor()),
            ("model", RidgeCV())
        ]),
    }

    # ============= Task-specific configuration =============
    tasks = {
        "green_density": {
            "input_columns": ["temperature", "doctor_blade", "casting_speed", "humidity", "volume_flow_rate"],
            "target_column": "green_density",
            "plot": {
                "title": "Green Density",
                "xlabel": "Target Values [g/cm$^3$]",
                "ylabel": "Predicted Values [g/cm$^3$]",
                "color": "dodgerblue"
            }
        },
        "green_thickness": {
            "input_columns": ["temperature", "doctor_blade", "casting_speed", "humidity", "volume_flow_rate"],
            "target_column": "green_thickness",
            "plot": {
                "title": "Green Thickness",
                "xlabel": "Target Values [µm]",
```

```
                "ylabel": "Predicted Values [µm]",
                "color": "skyblue"
            }
        },
        "sintered_density": {
            "input_columns": ["tape_id", "green_thickness", "
    green_density"],
            "target_column": "sintering_density",
            "plot": {
                "title": "Sintered Density",
                "xlabel": "Target Values [g/cm³]",
                "ylabel": "Predicted Values [g/cm³]",
                "color": "darkturquoise"
            }
        },
        "sintered_thickness": {
            "input_columns": ["tape_id", "green_thickness", "
    green_density"],
            "target_column": "sintering_thickness",
            "plot": {
                "title": "Sintered Thickness",
                "xlabel": "Target Values [µm]",
                "ylabel": "Predicted Values [µm]",
                "color": "deepskyblue"
            }
        },
        "reduced_density": {
            "input_columns": ["tape_id", "sintering_thickness", "
    sintering_density"],
            "target_column": "reducing_density",
            "plot": {
                "title": "Reduced Density",
                "xlabel": "Target Values [g/cm³]",
                "ylabel": "Predicted Values [g/cm³]",
                "color": "royalblue"
            }
        },
        "reduced_thickness": {
            "input_columns": ["tape_id", "sintering_thickness", "
    sintering_density"],
            "target_column": "reducing_thickness",
            "plot": {
                "title": "Reduced Thickness",
                "xlabel": "Target Values [µm]",
                "ylabel": "Predicted Values [µm]",
                "color": "deeppink"
            }
        }
    }

    # ============= Train all models =============
    for name, cfg in tasks.items():
        print(f"\n Evaluation on the testing set for {name}")
```

```
        trainer = ModelTrainer(
            pipeline=pipelines[name],
            train_set=train_df,
            test_set=test_df,
            target_column=cfg["target_column"],
            input_columns=cfg["input_columns"],
            plot_config=cfg["plot"]
        )
        trainer.train_and_evaluate()
        trainer.save_model(f"trained_models/{name}_model.pkl")

if __name__ == "__main__":
    main()
```

C.5 Data availability

Data will be made available upon reasonable request.

Résumé de la thèse en Français

Les technologies de l'hydrogène jouent un rôle central dans la transition des combustibles fossiles vers les sources d'énergie renouvelables, indispensables à la réalisation des objectifs de neutralité carbone et de développement durable. Parmi elles, les cellules à oxyde solide (SOCs) se distinguent comme l'une des technologies les plus prometteuses pour la conversion d'énergie propre, grâce à leur haute efficacité et leur grande flexibilité vis-à-vis des combustibles utilisables. En particulier, les SOCs à support d'électrode combustible (FESCs) présentent un avantage notable lié à la présence d'une couche d'électrolyte plus mince (5–20 µm), ce qui permet de réduire les pertes ohmiques, d'abaisser la température de fonctionnement (500–750 °C) et d'améliorer les performances globales. La stabilité mécanique des FESCs dépend fondamentalement du substrat poreux épais constituant l'électrode combustible. Ce substrat est généralement composé d'un cermet de NiO/zircone stabilisée à l'yttrium. L'optimisation traditionnelle des paramètres de fabrication repose principalement sur des méthodes expérimentales de type essai-erreur, coûteuses en ressources, longues et difficiles à adapter à la production industrielle.

Cette thèse présente les résultats obtenus dans le cadre de la modélisation du procédé de fabrication du substrat d'électrode combustible des SOCs, comprenant une modélisation physique à grain grossier du coulage sur bande du substrat (Chapitre 3), une modélisation hybride du coulis destiné au coulage sur bande (Chapitre 4), et une modélisation par apprentissage automatique (ML) de la fabrication des substrats d'électrode combustible, depuis le coulage et le séchage jusqu'au frittage et à la réduction (Chapitre 5). Ces approches novatrices ont été développées dans le cadre des projets ARTISTIC et ML4SOC, fruit d'une collaboration entre l'UPJV (France) et l'IMD-2, FZJ (Allemagne). Les travaux ont démontré que les approches basées sur la physique et celles fondées sur les données abordent des aspects complémentaires d'un même défi, et que leur intégration est essentielle pour parvenir à une optimisation systématique et reproductible du processus de fabrication.

Le Chapitre 2 présente les bases fondamentales des SOCs. Il décrit leurs principes de fonctionnement, les matériaux typiquement utilisés pour chaque couche fonctionnelle, les configurations de conception les plus courantes ainsi que la voie de fabrication des cellules supportées sur électrode combustible. Cet aperçu établit les fondements nécessaires à la compréhension de la technologie SOC et de ses aspects scientifiques et techniques sous-jacents.

Le Chapitre 3 est consacré au développement d'un cadre de modélisation physique du procédé de fabrication des SOCs, en mettant particulièrement l'accent sur le coulage sur bande et le séchage du substrat d'électrode combustible. Ce travail s'appuie sur les recherches antérieures de mon groupe à l'UPJV (France), où la méthode

DEM a été appliquée avec succès à la modélisation de divers procédés de fabrication de batteries, qu'il s'agisse de batteries lithium-ion à électrolyte liquide ou de batteries tout solide. Cette étude adapte et étend la méthodologie aux SOCs, avec pour objectif d'établir un modèle de preuve de concept reliant directement les paramètres de fabrication à la microstructure résultante du substrat.

La modélisation tridimensionnelle basée sur la physique présentée au Chapitre 3 propose une approche équilibrée, comblant l'écart entre les techniques expérimentales d'imagerie à forte intensité de ressources (par exemple la tomographie X ou le FIB/SEM) et les méthodes stochastiques. Elle offre une capacité prédictive plus fondée que ces dernières, tout en assurant un débit de calcul nettement supérieur aux premières. Cette capacité soutient le cadre DEM développé ici, fournissant une représentation physiquement cohérente de la microstructure du substrat aux étapes pertinentes du coulage et du séchage.

Pour atteindre cet objectif, des données expérimentales initiales ont été recueillies à l'IMD-2, FZJ (Jülich, Allemagne), comprenant la composition et la formulation du coulis. Ces données ont été utilisées pour la modélisation DEM des étapes successives de fabrication (préparation du coulis, coulage sur bande et séchage) sur la plateforme de calcul haute performance MatriCS de l'UPJV (Amiens, France), reflétant fidèlement les procédures expérimentales réelles. Le modèle a été calibré à l'aide de données expérimentales internes, telles que la densité et la viscosité du coulis, ainsi que la densité et la porosité de la bande verte obtenue. Cette calibration garantit que les simulations reproduisent les conditions réelles de fabrication. Les simulations DEM ont confirmé la distribution homogène des matériaux au sein de la microstructure séchée, comme attendu avant les traitements thermiques. Bien que le modèle suppose un séchage homogène des particules BDPD, simplification du comportement réel, il reproduit les mécanismes clés et les tendances pertinentes pour l'étape de séchage, répondant ainsi aux objectifs de la preuve de concept.

Cette étude démontre que le flux de travail ARTISTIC ne se limite pas aux batteries mais peut également être appliqué aux technologies SOC. L'intégration de données d'imagerie et de caractérisation supplémentaires permettra d'améliorer la compréhension des relations entre les procédés et les performances. Malgré certaines simplifications, telles que la représentation sphérique des particules, cette méthode constitue, à ma connaissance, le cadre computationnel le plus complet actuellement disponible pour relier les paramètres de fabrication aux caractéristiques microstructurales du substrat d'électrode combustible. Elle fournit également un outil prédictif pour optimiser le procédé de coulage et explorer différents scénarios de production avant les essais expérimentaux. Le Chapitre 3 établit ainsi une base solide pour la modélisation physique de la fabrication des SOCs. Il offre une stratégie de calcul flexible capable d'accélérer la conception et la mise à l'échelle des dispositifs de conversion d'énergie, tout en jetant les bases des analyses et études présentées dans les chapitres suivants.

Sur cette base, le Chapitre 4 introduit un cadre de modélisation hybride destiné à surmonter le coût computationnel élevé associé aux simulations DEM du coulis à base de solvant, en particulier lors des ajustements répétés des paramètres FF nécessaires pour garantir l'accord avec les données expérimentales dans de grands domaines de

simulation. En intégrant les techniques d'apprentissage profond (DL) aux modèles physiques, ce chapitre vise à développer une approche hybride pour la simulation du coulis, maintenant la précision tout en réduisant considérablement les besoins de calcul.

Le flux de travail débute par la génération d'un jeu de données microstructurales du coulis à l'aide des simulations DEM de préparation du coulis pour le coulage sur bande décrites au Chapitre 3. Ces données ont ensuite servi à entraîner le modèle de DL, basé sur un réseau VGG16 modifié, capable de prédire les microstructures finales du coulis dans les substrats de FESCs. Afin de préserver l'interprétabilité physique et d'assurer la précision, les microstructures prédites ont été rééquilibrées par des simulations DEM. Ce cadre hybride combine ainsi les forces des approches physiques et des approches fondées sur les données. Le modèle entraîné a atteint d'excellentes performances prédictives, comme l'indiquent les valeurs élevées de R^2 et les faibles MSE et MAE lors de l'entraînement. La fidélité physique des microstructures prédites a été confirmée par des analyses RDF. Le modèle a également montré une bonne adaptabilité lorsqu'il a été testé sur différentes microstructures de coulis, avec un bon accord entre les microstructures prédites et simulées. Certaines divergences ont été observées, notamment pour les couches de coulis plus épaisses, ouvrant des perspectives pour des améliorations futures. Malgré ces limites, l'architecture VGG16 modifiée s'est révélée être un réseau neuronal robuste pour la modélisation hybride des procédés de fabrication du substrat, en particulier lors de la préparation du coulis. Le flux de travail développé met en évidence le potentiel de la modélisation de substitution fondée sur les données pour accélérer considérablement les tâches de validation et d'optimisation, autrement dépendantes de simulations physiques coûteuses. Ce travail représente une étape importante vers des stratégies de modélisation évolutives et efficaces pour la fabrication des dispositifs de conversion d'énergie.

Le Chapitre 5 présente une approche basée sur l'apprentissage automatique (ML) visant à prédire l'épaisseur et la densité du substrat d'électrode combustible à travers trois étapes clés du processus de fabrication : le coulage et le séchage, le frittage et la réduction du NiO. L'attention se déplace ici du cadre de modélisation physique développé dans le projet ARTISTIC vers la modélisation fondée sur les données expérimentales dans le cadre du projet ML4SOC.

L'effet de la température sur les propriétés rhéologiques du coulis a été examiné par des mesures réalisées à différentes températures, révélant qu'une température plus élevée entraîne une viscosité plus faible. Ce résultat met en évidence le rôle critique de la température dans le contrôle du comportement d'écoulement du coulis, influençant directement la qualité de la bande verte après le coulage et le séchage.

Pour garantir la cohérence des expériences, la gestion systématique des données et la haute qualité des mesures, une stratégie de collecte de données améliorée a été mise en place. Celle-ci inclut l'intégration d'un ELN pour l'acquisition automatique *in-situ* des paramètres de procédé durant le coulage et le séchage, complétée par la caractérisation sur site des bandes obtenues.

Les modèles ML développés ont montré d'excellentes performances prédictives,

avec des valeurs de R^2 supérieures à 0.9 et des erreurs MAE et RMSE faibles comparées aux échelles de mesure expérimentales de chaque variable cible. L'analyse des données expérimentales a mis en évidence l'influence de paramètres de fabrication difficilement observables, tels que la température, l'humidité et le débit d'air d'échappement à l'intérieur de la machine de coulage, sur les propriétés du substrat. Ces résultats ouvrent la voie à une réduction significative des approches empiriques dans la fabrication des SOCs, en permettant une optimisation et une montée en échelle guidées par les données.

Dans l'ensemble, les stratégies physiques et basées sur les données développées dans cette thèse se complètent mutuellement. Les simulations DEM fournissent une compréhension physique et une capacité prédictive à l'échelle du procédé et de la microstructure, tout en générant des données synthétiques cohérentes pouvant enrichir les ensembles expérimentaux. Parallèlement, les modèles ML offrent des moyens rapides et adaptatifs de révéler des tendances cachées dans des données de fabrication complexes, soutenant ainsi la prise de décision pour l'optimisation expérimentale pilotée par les données. La combinaison de ces deux approches établit un cadre intégrant la modélisation numérique, la production expérimentale et la science des données. Grâce à cette intégration, la thèse propose une base pour une fabrication évolutive, reproductible et écoénergétique des substrats d'électrode combustible des SOCs. Les principales contributions de cette thèse résident donc dans le développement de nouveaux outils de modélisation, l'intégration cohérente des simulations et des expériences dans des flux de travail unifiés, et l'application de l'apprentissage automatique à des défis industriels concrets. Dans l'ensemble, cette thèse montre comment une telle stratégie combinée peut soutenir une production plus systématique, reproductible et efficace sur le plan énergétique des SOCs, tout en ouvrant la voie à leur passage vers des applications industrielles à grande échelle.

Publications and conferences

Publications

[P1] **Tan Le-Dinh**, Mohammed Alabdali, Franco M. Zanotto, Hartmut Schlenz, Norbert H. Menzler, Olivier Guillon, Alejandro A. Franco: Coarse-Grained Physics-Based Modelling for Tape Casting of Fuel-Electrode Supports in Solid Oxide Cells. *Journal of Power Sources*, 662 (2026) 238655.

[P2] **Tan Le-Dinh**, Hartmut Schlenz, Norbert H. Menzler, Alejandro A. Franco, Olivier Guillon: Data-Driven Machine Learning Modelling for the Manufacturing of the Fuel Electrode Support in Solid Oxide Cells. *Energy and AI*, 24 (2026) 100687.

[P3] **Tan Le-Dinh**, Utkarsh Vijay, Diego E. Galvez-Aranda, Hartmut Schlenz, Norbert H. Menzler, Olivier Guillon, Alejandro A. Franco: Deep Learning-Enhanced Physical Modelling for Tape-Casting Slurry Microstructures of Solid Oxide Cell Substrates. In preparation.

[P4] Utkarsh Vijay, Diego E. Galvez-Aranda, Franco M. Zanotto, **Tan Le-Dinh**, Mohammed Alabdali, Mark Asch, Alejandro A. Franco: A Hybrid Modelling Approach Coupling Physics-Based Simulation and Deep Learning for Battery Electrode Manufacturing Simulations. *Energy Storage Materials*, 75 (2025) 103883.

[P5] Diego E. Galvez-Aranda, **Tan Le-Dinh**, Utkarsh Vijay, Franco M. Zanotto, Alejandro A. Franco: Time-Dependent Deep Learning Manufacturing Process Model for Battery Electrode Microstructure Prediction. *Advanced Energy Materials*, 2024, 14, 2400376.

Conferences

[C1] *"Machine Learning-Based Data Modelling for the Manufacturing of the Fuel Electrode Support in Solid Oxide Cells"*, Invited Poster Presentation, **International Symposium on Ceramics for Sustainable Energy Transition**, Köln, Germany, August 27–28, 2025.

[C2] *"Machine Learning-Based Data Simulation for the Manufacturing of the Fuel Electrode Support in Solid Oxide Cells"*, Poster Presentation, **2nd Conference on Artificial Intelligence in Materials Science and Engineering (AI MSE 2025)**, Ruhr-University Bochum, Germany, November 18–19, 2025.

References

[1] Hugo Alberto Alvarez-Perez and Rolando Fuentes-Bracamontes. "Exploring energy transition through AI codification of leadership perspective and corporate strategies: The case of Mexico". In: *Business Horizons* (Oct. 2024).

[2] David L. Mccollum, Volker Krey, and Keywan Riahi. "Beyond Rio: Sustainable energy scenarios for the 21st century". In: *Natural Resources Forum* 36 (4 Nov. 2012), pp. 215–230.

[3] Jiannan Wang and Waseem Azam. "Natural resource scarcity, fossil fuel energy consumption, and total greenhouse gas emissions in top emitting countries". In: *Geoscience Frontiers* 15 (2 Mar. 2024), p. 101757.

[4] European Commission. *Renewable energy targets*. Accessed March 13, 2026. 2025.

[5] Subbarama Kousik Suraparaju, Mahendran Samykano, Jagadeeswara Reddy Vennapusa, Reji Kumar Rajamony, Dhinesh Balasubramanian, Zafar Said, and Adarsh Kumar Pandey. "Challenges and prospectives of energy storage integration in renewable energy systems for net zero transition". In: *Journal of Energy Storage* 125 (July 2025), p. 116923.

[6] David S. Renné. "Progress, opportunities and challenges of achieving net-zero emissions and 100% renewables". In: *Solar Compass* 1 (May 2022), p. 100007.

[7] Chi Wei Su, Li Dong Pang, Ran Tao, Xuefeng Shao, and Muhammad Umar. "Renewable energy and technological innovation: Which one is the winner in promoting net-zero emissions?" In: *Technological Forecasting and Social Change* 182 (Sept. 2022), p. 121798.

[8] Emma Serwaa Obobisa. "Achieving 1.5 °C and net-zero emissions target: The role of renewable energy and financial development". In: *Renewable Energy* 188 (Apr. 2022), pp. 967–985.

[9] Daqin Guan, Bowen Wang, Jiguang Zhang, Rui Shi, Kui Jiao, Lincai Li, Yang Wang, Biao Xie, Qingwen Zhang, Jie Yu, Yunfeng Zhu, Zongping Shao, and Meng Ni. "Hydrogen society: from present to future". In: *Energy Environ. Sci.* 16 (11 2023), pp. 4926–4943.

[10] Zonghao Shen, Jean-Marc Bassat, Sebastien Fourcade, Alain Demourgues, Etienne Durand, Lionel Teule-Gay, Mathieu Duttine, and Jacinthe Gamon. "Is Fluorine Incorporation in the $La_0.6Sr_0.4Co_0.2Fe_0.8O_{3-\delta}$ Improving Its Electrochemical Behavior for Solid Oxide Cells Applications?" In: *Advanced Energy Materials* 14.32 (), p. 2401518.

[11] *Primary energy consumption by source, World*. `https://ourworldindata.org/grapher/primary-sub-energy-source`. Accessed March 13, 2026.

[12] L. Blum, H.-P. Buchkremer, S. Gross, A. Gubner, L. G. J. (Bert) de Haart, H. Nabielek, W. J. Quadakkers, U. Reisgen, M. J. Smith, R. Steinberger-Wilckens, R. W. Steinbrech, F. Tietz, and I. C. Vinke. "Solid Oxide Fuel Cell Development at Forschungszentrum Juelich". In: *Fuel Cells* 7.3 (2007), pp. 204–210.

[13] Q. Shao, R. Fernández-González, J. C. Ruiz-Morales, L. Bouhala, D. Fiorelli, A. Younes, P. Núñez, S. Belouettar, and A. Makradi. "An advanced numerical model for energy conversion and crack growth predictions in Solid Oxide Fuel Cell units". In: *International Journal of Hydrogen Energy* 40 (46 Dec. 2015), pp. 16509–16520.

[14] Q. Shao, A. Makradi, D. Fiorelli, A. Mikdam, W. Huang, H. Hu, and S. Belouettar. "Material Twin for composite material microstructure generation and reconstruction". In: *Composites Part C: Open Access* 7 (Mar. 2022), p. 100216.

[15] Eric Langner, Ahmed Makradi, Mohamed El Hachemi, Salim Belouettar, and Thomas Wallmersperger. "Determination of the effective conductivities of solid oxide fuel cell electrodes using the first-order homogenization method". In: *PAMM* 23 (2 Oct. 2023), e202300105.

[16] E. Da Rosa Silva, G. Sassone, M. Prioux, M. Hubert, B. Morel, and J. Laurencin. "A multiscale model validated on local current measurements for understanding the solid oxide cells performances". In: *Journal of Power Sources* 556 (Feb. 2023), p. 232499.

[17] Paola Costamagna, Andrea De Giorgi, Gabriele Moser, Sebastiano B. Serpico, and Andrea Trucco. "Data-driven techniques for fault diagnosis in power generation plants based on solid oxide fuel cells". In: *Energy Conversion and Management* 180 (Jan. 2019), pp. 281–291.

[18] Hamidreza Dehghani and Andreas Zilian. "Finite strain poro-hyperelasticity: an asymptotic multi-scale ALE-FSI approach supported by ANNs". In: *Computational Mechanics* 71 (4 Apr. 2023), pp. 695–719.

[19] Hamidreza Dehghani and Andreas Zilian. "A hybrid MGA-MSGD ANN training approach for approximate solution of linear elliptic PDEs". In: *Mathematics and Computers in Simulation* 190 (Dec. 2021), pp. 398–417.

[20] Hamidreza Dehghani and Andreas Zilian. "Poroelastic model parameter identification using artificial neural networks: on the effects of heterogeneous porosity and solid matrix Poisson ratio". In: *Computational Mechanics* 66 (3 Sept. 2020), pp. 625–649.

[21] Qian Shao, Jian Liu, Qun Huang, Jie Yang, Heng Hu, Salim Belouettar, and Gaetano Giunta. "A data-driven analysis on bridging techniques for heterogeneous materials and structures". In: *Mechanics of Advanced Materials and Structures* 28 (1 2021), pp. 1–15.

[22] Jian Zhao, Xianguo Li, Chris Shum, and John McPhee. "A Review of physics-based and data-driven models for real-time control of polymer electrolyte membrane fuel cells". In: *Energy and AI* 6 (Dec. 2021), p. 100114.

[23] Eric Langner, Hamidreza Dehghani, Mohamed El Hachemi, Elias Belouettar–Mathis, Ahmed Makradi, Thomas Wallmersperger, Sylvain Gouttebroze, Heinz Preisig, Casper Welzel Andersen, Qian Shao, Heng Hu, and Salim Belouettar. "Physics-based and data-driven modelling and simulation of Solid Oxide Fuel Cells". In: *International Journal of Hydrogen Energy* 96 (Dec. 2024), pp. 962–983.

[24] Teo Lombardo, Fernando Caro, Alain C. Ngandjong, Jean Baptiste Hoock, Marc Duquesnoy, Jean Charles Delepine, Adrien Ponchelet, Sylvain Doison, and Alejandro A. Franco. "The ARTISTIC Online Calculator: Exploring the Impact of Lithium-Ion Battery Electrode Manufacturing Parameters Interactively Through Your Browser". In: *Batteries & Supercaps* 5 (3 Mar. 2022), e202100324.

[25] Javier F. Troncoso, Franco M. Zanotto, Diego E. Galvez-Aranda, Diana Zapata Dominguez, Lucie Denisart, and Alejandro A. Franco. "The ARTISTIC Battery Manufacturing Digitalization Initiative: From Fundamental Research to Industrialization". In: *Batteries & Supercaps* 8 (1 Jan. 2025), e202400385.

[26] Franco M. Zanotto, Diana Zapata Dominguez, Elixabete Ayerbe, Iker Boyano, Christine Burmeister, Marc Duquesnoy, Marlene Eisentraeger, Jonathan Florez Montaño, Alfonso Gallo-Bueno, Lukas Gold, Florian Hall, Nicolaj Kaden, Bernhard Muerkens, Laida Otaegui, Yvan Reynier, Simon Stier, Matthias Thomitzek, Artem Turetskyy, Nicolas Vallin, Jacob Wessel, Xukuan Xu, Jeyhun Abbasov, and Alejandro A. Franco. "Data Specifications for Battery Manufacturing Digitalization: Current Status, Challenges, and Opportunities". In: *Batteries & Supercaps* 5 (9 Sept. 2022), e202200224.

[27] Feng Han, Robert Mücke, Tim Van Gestel, André Leonide, Norbert H. Menzler, Hans Peter Buchkremer, and Detlev Stöver. "Novel high-performance solid oxide fuel cells with bulk ionic conductance dominated thin-film electrolytes". In: *Journal of Power Sources* 218 (2012).

[28] Shuai He, Yuanfeng Zou, Kongfa Chen, San P Jiang, and Correspondence P San Jiang. "A critical review of key materials and issues in solid oxide cells". In: *Interdisciplinary Materials* 2 (1 Jan. 2023), pp. 111–136.

[29] Christian Lenser, David Udomsilp, Norbert H. Menzler, Peter Holtappels, Takaya Fujisaki, Leonard Kwati, Hiroshige Matsumoto, Antonio Gianfranco Sabato, Federico Smeacetto, Andreas Chrysanthou, and Sebastian Molin. "9 - Solid oxide fuel and electrolysis cells". In: *Advanced Ceramics for Energy Conversion and Storage*. Ed. by Olivier Guillon. Elsevier Series on Advanced Ceramic Materials. Elsevier, 2020, pp. 387–547.

[30] Ming Xiao, Zuoqing Liu, Haosong Di, Yuesheng Bai, Guangming Yang, Dmitry A. Medvedev, Zhixin Luo, Wei Wang, Wei Zhou, Ran Ran, and Zongping Shao. "High-entropy materials for solid oxide cells: Synthesis, applications, and prospects". In: *Journal of Energy Chemistry* 104 (May 2025), pp. 268–296.

[31] Yongjian Ye, Xiang Sun, Mengzhen Zhou, and Yan Chen. "A Mini Review on the Application of Proton-Conducting Solid Oxide Cells for CO2 Conversion". In: *Energy & Fuels* 34.11 (2020), pp. 13427–13437.

[32] Urooj Tariq, Muhammad Zubair Khan, Osama Gohar, Zaheer Ud Din Babar, Farman Ali, Rizwan Ahmed Malik, Inna A. Starostina, Samia, Javed Rehman, Iftikhar Hussain, Mohsin Saleem, Abdul Ghaffar, Mohsin Ali Marwat, Kun Zheng, Martin Motola, and Muhammad Bilal Hanif. "Bridging the Gap between fundamentals and efficient devices: Advances in proton-conducting oxides for low-temperature solid oxide fuel cells". In: *Journal of Power Sources* 613 (Sept. 2024), p. 234910.

[33] Kevin Kendall and Michaela Kendall. *High-Temperature Solid Oxide Fuel Cells for the 21st Century: Fundamentals, Design and Applications: Second Edition*. Jan. 2015, pp. 1–508.

[34] Sheila Mae C. Ang, Eric S. Fraga, Nigel P. Brandon, Nouri J. Samsatli, and Daniel J.L. Brett. "Fuel cell systems optimisation – Methods and strategies". In: *International Journal of Hydrogen Energy* 36.22 (2011). Fuel Cell Technologies: FUCETECH 2009, pp. 14678–14703.

[35] Stephan Sarner, Andrea Schreiber, Norbert H. Menzler, and Olivier Guillon. "Recycling Strategies for Solid Oxide Cells". In: *Advanced Energy Materials* 12.35 (2022), p. 2201805.

[36] Catarina Mendonça, António Ferreira, and Diogo M. F. Santos. "Towards the Commercialization of Solid Oxide Fuel Cells: Recent Advances in Materials and Integration Strategies". In: *Fuels* 2.4 (2021), pp. 393–419.

[37] Abdalla M. Abdalla, Shahzad Hossain, Pg Mohd Iskandr Petra, Mostafa Ghasemi, and Abul K. Azad. "Achievements and trends of solid oxide fuel cells in clean energy field: a perspective review". In: *Frontiers in Energy* 14 (2 June 2020), pp. 359–382.

[38] San Ping Jiang and Siew Hwa Chan. "A review of anode materials development in solid oxide fuel cells". In: *Journal of Materials Science 2004 39:14* 39 (14 July 2004), pp. 4405–4439.

[39] Masashi Mori, Tohru Yamamoto, Hibiki Itoh, Hideaki Inaba, and Hiroaki Tagawa. "Thermal Expansion of Nickel-Zirconia Anodes in Solid Oxide Fuel Cells during Fabrication and Operation". In: *Journal of The Electrochemical Society* 145 (4 Apr. 1998), pp. 1374–1381.

[40] Quang Minh. Nguyen and Takehiko. Takahashi. *Science and technology of ceramic fuel cells*. Elsevier Science, 1995, p. 366.

[41] Shenglan Yang, Jianbao Gao, Martina Trini, Salvatore De Angelis, Peter Stanley Jørgensen, Jacob R. Bowen, Lijun Zhang, and Ming Chen. "Ni coarsening in Ni-yttria stabilized zirconia electrodes: Three-dimensional quantitative phase-field simulations supported by ex-situ ptychographic nano-tomography". In: *Acta Materialia* 246 (Mar. 2023), p. 118708.

[42] John D. Kirtley, Melissa D. McIntyre, David M. Halat, and Robert A. Walker. "(Invited) Insights into SOFC Ni/YSZ Anode Degradation Using In-Situ Spectrochronopotentiometrys". In: *ECS Transactions* 50 (44 Apr. 2013), p. 3.

[43] Kasra Nikooyeh, Ryan Clemmer, Vanesa Alzate-Restrepo, and Josephine M. Hill. "Effect of hydrogen on carbon formation on Ni/YSZ composites exposed to methane". In: *Applied Catalysis A: General* 347 (1 Sept. 2008), pp. 106–111.

[44] Jens F.B. Rasmussen and Anke Hagen. "The effect of H2S on the performance of Ni–YSZ anodes in solid oxide fuel cells". In: *Journal of Power Sources* 191 (2 June 2009), pp. 534–541.

[45] A. Hauch, A. Hagen, J. Hjelm, and T. Ramos. "Sulfur Poisoning of SOFC Anodes: Effect of Overpotential on Long-Term Degradation". In: *Journal of The Electrochemical Society* 161 (6 May 2014), F734–F743.

[46] Tomoaki Namioka, Taichi Naruse, and Ryosuke Yamane. "Behavior and mechanisms of Ni/ScSZ cermet anode deterioration by trace tar in wood gas in a solid oxide fuel cell". In: *International Journal of Hydrogen Energy* 36 (9 May 2011), pp. 5581–5588.

[47] Norbert H. Menzler, Roland Peters, Nicolas Kruse, Dominik Schäfer, and Felix Kunz. "Solid oxide cells for hydrogen generation and usage: From materials to systems". In: *Ceramic forum international* 100 (3 2023), pp. 48–56.

[48] Norbert Menzler, Frank Tietz, Sven Uhlenbruck, Hans Buchkremer, and Detlev Stöver. "Materials and Manufacturing Technologies for Solid Oxide Fuel Cells". In: *Journal of Materials Science* 45 (June 2010), pp. 3109–3135.

[49] Saddam Hussain and Li Yangping. "Review of solid oxide fuel cell materials: cathode, anode, and electrolyte". In: *Energy Transitions 2020 4:2* 4 (2 Oct. 2020), pp. 113–126.

[50] K. Sick, N. Grigorev, N.H. Menzler, and O. Guillon. "Development of Cathode Contacting for SOFC Stacks". In: (Jan. 2019), pp. 99–111.

[51] P. Piccardo, P. Gannon, S. Chevalier, M. Viviani, A. Barbucci, G. Caboche, R. Amendola, and S. Fontana. "ASR evaluation of different kinds of coatings on a ferritic stainless steel as SOFC interconnects". In: *Surface and Coatings Technology* 202 (4-7 Dec. 2007), pp. 1221–1225.

[52] Zhenguo Yang, Guan Guang Xia, Gary D. Maupin, and Jeffry W. Stevenson. "Conductive protection layers on oxidation resistant alloys for SOFC interconnect applications". In: *Surface and Coatings Technology* 201 (7 Dec. 2006), pp. 4476–4483.

[53] Ludger Blum, L. G.J. De Haart, Jürgen Malzbender, Norbert H. Menzler, Josef Remmel, and Robert Steinberger-Wilckens. "Recent results in Jülich solid oxide fuel cell technology development". In: *Journal of Power Sources* 241 (Nov. 2013), pp. 477–485.

[54] Muhammad Zubair Khan, Asim Iltaf, Hafiz Ahmad Ishfaq, Fahd Nawaz Khan, Waqas Hassan Tanveer, Rak-Hyun Song, Muhammad Taqi Mehran, Mohsin Saleem, Amjad Hussain, and Zubair Masaud and. "Flat-tubular solid oxide fuel cells and stacks: a review". In: *Journal of Asian Ceramic Societies* 9.3 (2021), pp. 745–770.

[55] Catarina Mendonça, António Ferreira, and Diogo M. F. Santos. "Towards the Commercialization of Solid Oxide Fuel Cells: Recent Advances in Materials and Integration Strategies". In: *Fuels 2021, Vol. 2, Pages 393-419* 2 (4 Oct. 2021), pp. 393–419.

[56] F. Tietz, H. P. Buchkremer, and D. Stöver. "Components manufacturing for solid oxide fuel cells". In: *Solid State Ionics* 152-153 (Dec. 2002), pp. 373–381.

[57] S. M. Majhi, S. K. Behura, S. Bhattacharjee, B. P. Singh, T. K. Chongdar, N. M. Gokhale, and L. Besra. "Anode supported solid oxide fuel cells (SOFC) by electrophoretic deposition". In: *International Journal of Hydrogen Energy* 36 (22 Nov. 2011), pp. 14930–14935.

[58] Ludger Blum, L. G.J. de Haart, Jürgen Malzbender, Nikolaos Margaritis, and Norbert H. Menzler. "Anode-Supported Solid Oxide Fuel Cell Achieves 70 000 Hours of Continuous Operation". In: *Energy Technology* 4 (8 2016).

[59] "A review of solid oxide fuel cell component fabrication methods toward lowering temperature". In: *International Journal of Energy Research* 44 (2 Feb. 2020), pp. 594–611.

[60] Aiswarya Krishnakumar Padinjarethil, Fiammetta Rita Bianchi, Barbara Bosio, and Anke Hagen. "Electrochemical Characterization and Modelling of Anode and Electrolyte Supported Solid Oxide Fuel Cells". In: *Frontiers in Energy Research* 9 (Sept. 2021), p. 668964.

[61] David Udomsilp, Christian Lenser, Olivier Guillon, and Norbert H. Menzler. *Performance Benchmark of Planar Solid Oxide Cells Based on Material Development and Designs*. 2021.

[62] Norbert H. Menzler, Wolfgang Schafbauer, Feng Han, Oliver Büchler, Robert Mücke, Hans Peter Buchkremer, and Detlev Stöver. "Development of High Power Density Solid Oxide Fuel Cells (SOFCs) for Long-Term Operation". In: *Materials Science Forum* 654-656 (2010), pp. 2875–2878.

[63] N. H. Menzler, J. Malzbender, P. Schoderböck, R. Kauert, and H. P. Buchkremer. "Sequential Tape Casting of Anode-Supported Solid Oxide Fuel Cells". In: *Fuel Cells* 14 (1 Feb. 2014), pp. 96–106.

[64] Anu Maria. "Introduction to modeling and simulation". In: *Proceedings of the 29th Conference on Winter Simulation*. WSC '97. Atlanta, Georgia, USA: IEEE Computer Society, 1997, pp. 7–13.

[65] Juan M. Durán. "What is a Simulation Model?" In: *Minds and Machines* 30 (3 Sept. 2020), pp. 301–323.

[66] Peter Truran. “Models: Useful but Not True”. In: July 2013, pp. 61–67.

[67] Eric Winsberg. *Science in the Age of Computer Simulation*. University of Chicago Press, Oct. 2010.

[68] G.E.P. Box. “Robustness in the Strategy of Scientific Model Building”. In: *Robustness in Statistics*. Ed. by ROBERT L. LAUNER and GRAHAM N. WILKINSON. Academic Press, 1979, pp. 201–236.

[69] William Menner. “Overview of modeling and simulation”. In: *24th AIPR Workshop on Tools and Techniques for Modeling and Simulation*. Ed. by Donald J. Gerson. Vol. 2645. International Society for Optics and Photonics. SPIE, 1996, pp. 3 –17.

[70] Osman Balci. “Principles of simulation model validation, verification, and testing”. In: *Transactions of The Society for Computer Simulation International* 14 (1997), pp. 3–12.

[71] Changjing Fu, Siew Hwa Chan, Qinglin Liu, Xiaoming Ge, and G. Pasciak. “Fabrication and evaluation of Ni-GDC composite anode prepared by aqueous-based tape casting method for low-temperature solid oxide fuel cell”. In: *International Journal of Hydrogen Energy* 35 (1 Jan. 2010), pp. 301–307.

[72] M. Letilly, O. Joubert, M. T. Caldes, and A. Le Gal La Salle. “Tape casting fabrication, co-sintering and optimisation of anode/electrolyte assemblies for SOFC based on BIT07-Ni/BIT07”. In: *International Journal of Hydrogen Energy* 37 (5 Mar. 2012), pp. 4346–4355.

[73] C. Pagnoux, T. Chartier, M. de F. Granja, F. Doreau, J.M. Ferreira, and J.F. Baumard. “Aqueous suspensions for tape-casting based on acrylic binders”. In: *Journal of the European Ceramic Society* 18.3 (1998), pp. 241–247.

[74] Pavel Vozdecky, Andreas Roosen, Qianli Ma, Frank Tietz, and Hans Buchkremer. “Properties of Tape-Cast Y-Substituted Strontium Titanate for Planar Anode Substrates in SOFC Applications”. In: *Journal of Materials Science* 46 (May 2011), pp. 3493–3499.

[75] Eric R. Twiname Richard E. Mistler. *Tape casting: Theory and practice*. The American Ceramic Society, Westerville, OH, 2000.

[76] Sun Dong Kim, Sang Hoon Hyun, Jooho Moon, Jong Hee Kim, and Rak Hyun Song. “Fabrication and characterization of anode-supported electrolyte thin films for intermediate temperature solid oxide fuel cells”. In: *Journal of Power Sources* 139 (1-2 Jan. 2005), pp. 67–72.

[77] M. Descamps, G. Ringuet, D. Leger, and B. Thierry. “Tape-casting: Relationship between organic constituents and the physical and mechanical properties of tapes”. In: *Journal of the European Ceramic Society* 15 (4 Jan. 1995), pp. 357–362.

[78] Jeong Hun Kim, Hyunseok Ko, Dong Hun Yeo, Zeehoon Park, Upendra Kumar, Kwan Hee Yoo, Aziz Nasridinov, and Sung Beom Cho. "A versatile strategy for hybridizing small experimental and large simulation data: A case for ceramic tape-casting process". In: *Materials and Design* 234 (2023).

[79] M. Jabbari, R. Bulatova, A. I.Y. Tok, C. R.H. Bahl, E. Mitsoulis, and J. H. Hattel. "Ceramic tape casting: A review of current methods and trends with emphasis on rheological behaviour and flow analysis". In: *Materials Science and Engineering: B* 212 (Oct. 2016), pp. 39–61.

[80] Davide Gardini, Marco Deluca, Marco Nagliati, and Carmen Galassi. "Flow properties of PLZTN aqueous suspensions for tape casting". In: *Ceramics International* 36 (5 July 2010), pp. 1687–1696.

[81] U. Doraswami, P. Shearing, N. Droushiotis, K. Li, N. P. Brandon, and G. H. Kelsall. "Modelling the effects of measured anode triple-phase boundary densities on the performance of micro-tubular hollow fiber SOFCs". In: *Solid State Ionics*. Vol. 192. 2011.

[82] L. Holzer, B. Münch, B. Iwanschitz, M. Cantoni, Th Hocker, and Th Graule. "Quantitative relationships between composition, particle size, triple phase boundary length and surface area in nickel-cermet anodes for Solid Oxide Fuel Cells". In: *Journal of Power Sources*. Vol. 196. 2011.

[83] N. Vivet, S. Chupin, E. Estrade, T. Piquero, P. L. Pommier, D. Rochais, and E. Bruneton. "3D Microstructural characterization of a solid oxide fuel cell anode reconstructed by focused ion beam tomography". In: *Journal of Power Sources* 196 (18 2011).

[84] P. R. Shearing, J. Gelb, and N. P. Brandon. "X-ray nano computerised tomography of SOFC electrodes using a focused ion beam sample-preparation technique". In: *Journal of the European Ceramic Society* 30 (8 2010).

[85] Kyle N. Grew, Aldo A. Peracchio, and Wilson K.S. Chiu. "Characterization and analysis methods for the examination of the heterogeneous solid oxide fuel cell electrode microstructure: Part 2. Quantitative measurement of the microstructure and contributions to transport losses". In: *Journal of Power Sources* 195 (24 2010).

[86] Emily M. Ryan and Partha P. Mukherjee. "Mesoscale modeling in electrochemical devices—A critical perspective". In: *Progress in Energy and Combustion Science* 71 (2019), pp. 118–142.

[87] Yoshinori Suzue, Naoki Shikazono, and Nobuhide Kasagi. "Micro modeling of solid oxide fuel cell anode based on stochastic reconstruction". In: *Journal of Power Sources* 184 (1 2008).

[88] Matthias Neumann, Jakub Staněk, Omar M. Pecho, Lorenz Holzer, Viktor Beneš, and Volker Schmidt. "Stochastic 3D modeling of complex three-phase microstructures in SOFC-electrodes with completely connected phases". In: *Computational Materials Science* 118 (2016).

[89] Yanxiang Zhang, Mufu Yan, Yanhong Wan, Zhenjun Jiao, Yu Chen, Fanglin Chen, Changrong Xia, and Meng Ni. "High-throughput 3D reconstruction of stochastic heterogeneous microstructures in energy storage materials". In: *npj Computational Materials* 5 (1 2019).

[90] H. Mohebbi, O. Sharifi, M. Golmohammad, and A. Molla Ahmad. "The Effect of Process Parameters on the Apparent Defects of Tape-Cast SOFC Half-Cell". In: *Advanced Ceramics Progress* 5.4 (2019), pp. 12–16.

[91] Bora Timurkutluk and Mahmut D. Mat. "Effects of anode fabrication parameters on the performance and redox behavior of solid oxide fuel cells". In: *Journal of Power Sources* 258 (2014).

[92] Bora Timurkutluk and Semiha Dokuyucu. "The role of tape thickness on mechanical properties and performance of electrolyte supports in solid oxide fuel cells". In: *Ceramics International* 44 (14 2018).

[93] *ERC Artistic*. `https://www.erc-artistic.eu/`. Accessed March 13, 2026.

[94] Teo Lombardo, Jean Baptiste Hoock, Emiliano N. Primo, Alain C. Ngandjong, Marc Duquesnoy, and Alejandro A. Franco. "Accelerated Optimization Methods for Force-Field Parametrization in Battery Electrode Manufacturing Modeling". In: *Batteries & Supercaps* 3 (8 Aug. 2020), pp. 721–730.

[95] Teo Lombardo, Alain C. Ngandjong, Amal Belhcen, and Alejandro A. Franco. "Carbon-Binder Migration: A Three-Dimensional Drying Model for Lithium-ion Battery Electrodes". In: *Energy Storage Materials* 43 (Dec. 2021), pp. 337–347.

[96] Alain C. Ngandjong, Teo Lombardo, Emiliano N. Primo, Mehdi Chouchane, Abbos Shodiev, Oier Arcelus, and Alejandro A. Franco. "Investigating electrode calendering and its impact on electrochemical performance by means of a new discrete element method model: Towards a digital twin of Li-Ion battery manufacturing". In: *Journal of Power Sources* 485 (Feb. 2021), p. 229320.

[97] Mohammed Alabdali, Franco M. Zanotto, Marc Duquesnoy, Anna Katharina Hatz, Duancheng Ma, Jérémie Auvergniot, Virginie Viallet, Vincent Seznec, and Alejandro A. Franco. "Three-dimensional physical modeling of the wet manufacturing process of solid-state battery electrodes". In: *Journal of Power Sources* 580 (2023).

[98] Sanaz Zarabi Golkhatmi, Muhammad Imran Asghar, and Peter D. Lund. "A review on solid oxide fuel cell durability: Latest progress, mechanisms, and study tools". In: *Renewable and Sustainable Energy Reviews* 161 (June 2022), p. 112339.

[99] Debabrata Mohanty, Ju Yu Hung, Yi Wen Chen, I. Ming Hung, and Yu Rou Lin. "Optimization and characterization of porous Ni/YSZ anode microstructure for solid oxide fuel cell". In: *Ceramics International* (Feb. 2025).

[100] M. Lira, N. Kostretsova, I. Babeli, L. Bernadet, S. Marquez, A. Morata, M. Torrell, and A. Tarancón. "Large-area 3D printed electrolyte-supported reversible solid oxide cells". In: *Electrochimica Acta* 467 (2023).

[101] Wolfgang Schafbauer, Norbert H. Menzler, and Hans P. Buchkremer. "Tape Casting of Anode Supports for Solid Oxide Fuel Cells at Forschungszentrum Jülich". In: *International Journal of Applied Ceramic Technology* 11 (1 Jan. 2014), pp. 125–135.

[102] Dennis Weitze, Franco M. Zanotto, Diana Zapata Dominguez, and Alejandro A. Franco. "Simulating solid-state battery cathode manufacturing via wet-processing with resolved active material geometries". In: *Energy Storage Materials* 73 (Nov. 2024), p. 103747.

[103] Jiahui Xu, Alain C. Ngandjong, Chaoyue Liu, Franco M. Zanotto, Oier Arcelus, Arnaud Demortière, and Alejandro A. Franco. "Lithium ion battery electrode manufacturing model accounting for 3D realistic shapes of active material particles". In: *Journal of Power Sources* 554 (2023).

[104] Salim Barbhuiya, Andrey Jivkov, and Bibhuti Bhusan Das. "A review of multiscale modelling of concrete deterioration: Fundamentals, techniques and perspectives". In: *Construction and Building Materials* 406 (2023), p. 133472.

[105] C.-W. Hong. "Computer-Aided Process Design for Forming of Pore-Gradient Membranes". In: 1997.

[106] Farhang Radjai and Vincent Richefeu. "Contact dynamics as a nonsmooth discrete element method". In: *Mechanics of Materials* 41 (6 2009).

[107] Jamshid Ghaboussi and Ricardo Barbosa. "Three-dimensional discrete element method for granular materials". In: *International Journal for Numerical and Analytical Methods in Geomechanics* 14 (7 Sept. 1990), pp. 451–472.

[108] *LAMMPS Molecular Dynamics Simulator*. `https://www.lammps.org/`. Accessed March 13, 2026.

[109] Aidan P. Thompson, H. Metin Aktulga, Richard Berger, Dan S. Bolintineanu, W. Michael Brown, Paul S. Crozier, Pieter J. in 't Veld, Axel Kohlmeyer, Stan G. Moore, Trung Dac Nguyen, Ray Shan, Mark J. Stevens, Julien Tranchida, Christian Trott, and Steven J. Plimpton. "LAMMPS - a flexible simulation tool for particle-based materials modeling at the atomic, meso, and continuum scales". In: *Computer Physics Communications* 271 (Feb. 2022), p. 108171.

[110] Alain C. Ngandjong, Alexis Rucci, Mariem Maiza, Garima Shukla, Jorge Vazquez-Arenas, and Alejandro A. Franco. "Multiscale Simulation Platform Linking Lithium Ion Battery Electrode Fabrication Process with Performance at the Cell Level". In: *Journal of Physical Chemistry Letters* 8 (23 2017).

[111] J E Lennard-Jones. "Cohesion". In: *Proceedings of the Physical Society* 43.5 (1931), p. 461.

[112] *pair_style lj/cut command — LAMMPS documentation*. `https://docs.lammps.org/pair_lj.html`. Accessed March 13, 2026.

[113] *Lennard-Jones Potential*. `https://physicsatmcl.commons.msu.edu/lennard-jones-potential/`. Accessed: March 13, 2026.

[114] K.L. Johnson, Kevin Kendall, and A.D. Roberts. "Surface Energy and Contact of Elastic Solids". In: *Proceedings of The Royal Society A: Mathematical, Physical and Engineering Sciences* 324 (Sept. 1971), pp. 301–313.

[115] *pair_style granular command — LAMMPS documentation*. `https://docs.lammps.org/pair_gran.html`. Accessed March 13, 2026.

[116] Mohammed Alabdali. "Multiscale Modeling for the Optimization of the Manufacturing and the Interfaces in Solid State Batteries". Thèse de Doctorat. Amiens, France: Université de Picardie Jules Verne, 2024.

[117] *MatriCS Plateform*. `https://www.matrics.u-picardie.fr/en/documentation-2/partitions/`. Accessed March 13, 2026.

[118] S. Sridhar and U. B. Pal. "Effect of slurry properties on anode cermets for solid oxide fuel cells". In: *Powder Technology* 88 (2 1996).

[119] C. G. Fonseca, R. M.F. Basaglia, M. C. Brant, T. Matencio, and R. Z. Domingues. "Study of the rheological behavior of an anode slurry and the microstructural properties of an anode functional film obtained by spray coating". In: *Powder Technology* 192 (3 2009).

[120] Tong Liu, Cong Ren, Yanxiang Zhang, Yao Wang, Libin Lei, and Fanglin Chen. "Solvent effects on the morphology and performance of the anode substrates for solid oxide fuel cells". In: *Journal of Power Sources* 363 (2017).

[121] Alfred I.Y. Tok, Freddy Y.C. Boey, and Y. C. Lam. "Non-Newtonian fluid flow model for ceramic tape casting". In: *Materials Science and Engineering: A* 280 (2 2000).

[122] A. Yahia, S. Mantellato, and Robert J. Flatt. "Concrete rheology: A basis for understanding chemical admixtures". In: *Science and Technology of Concrete Admixtures* (Jan. 2016), pp. 97–127.

[123] Yasuki Nakayama. "Characteristics of a Fluid". In: *Introduction to Fluid Mechanics* (Jan. 2018), pp. 9–24.

[124] *Avizo software | materials characterization software - FR, (n.d.)* `https://www.thermofisher.com/de/de/home/electron-microscopy/products/software-em-3d-vis/avizo-software.html`. Accessed March 13, 2026.

[125] Fátima Ternero, Luís Guerra Rosa, Petr Urban, Juan Manuel Montes, and Francisco G. Cuevas. "Influence of the total porosity on the properties of sintered materials—a review". In: *Metals* 11 (5 2021).

[126] R. K. Jeela, G. Tosato, M. Ahmad, M. Wieler, A. Koeppe, B. Nestler, and D. Schneider. "Enhancing Solid Oxide Fuel Cells Development through Bayesian Active Learning". In: *Advanced Energy Materials* 15 (34 Sept. 2025), p. 2501216.

[127] Z. Yan, A. He, S. Hara, and N. Shikazono. "Modeling of solid oxide fuel cell (SOFC) electrodes from fabrication to operation: Microstructure optimization via artificial neural networks and multi-objective genetic algorithms". In: *Energy Conversion and Management* 198 (Oct. 2019), p. 111916.

[128] Seungsoo Jang, Yejin Kang, Kyung Taek Bae, Seong Hyun Park, Young Je Park, Dongyeon Kim, Hyeongmin Yu, Hyunjin Kim, Siwon Yu, and Kang Taek Lee. "Digital Twin of Solid Oxide Electrochemical Cells: From 3D Microstructure Reconstruction to Multiphysics Modeling". In: *Advanced Energy Materials* (2025), e03842.

[129] Marc Duquesnoy, Teo Lombardo, Mehdi Chouchane, Emiliano N. Primo, and Alejandro A. Franco. "Data-driven assessment of electrode calendering process by combining experimental results, in silico mesostructures generation and machine learning". In: *Journal of Power Sources* 480 (Dec. 2020), p. 229103.

[130] Marc Duquesnoy, Teo Lombardo, Fernando Caro, Florent Haudiquez, Alain C. Ngandjong, Jiahui Xu, Hassan Oularbi, and Alejandro A. Franco. "Functional data-driven framework for fast forecasting of electrode slurry rheology simulated by molecular dynamics". In: *npj Computational Materials* 8 (1 Dec. 2022), pp. 1–9.

[131] Alex Krizhevsky, Ilya Sutskever, and Geoffrey E Hinton. "ImageNet Classification with Deep Convolutional Neural Networks". In: *Advances in Neural Information Processing Systems*. Ed. by F. Pereira, C.J. Burges, L. Bottou, and K.Q. Weinberger. Vol. 25. Curran Associates, Inc., 2012.

[132] Christian Szegedy, Wei Liu, Yangqing Jia, Pierre Sermanet, Scott Reed, Dragomir Anguelov, Dumitru Erhan, Vincent Vanhoucke, and Andrew Rabinovich. "Going deeper with convolutions". In: *2015 IEEE Conference on Computer Vision and Pattern Recognition (CVPR)*. 2015, pp. 1–9.

[133] Ross Girshick, Jeff Donahue, Trevor Darrell, and Jitendra Malik. "Rich feature hierarchies for accurate object detection and semantic segmentation". In: *Proceedings of the IEEE Computer Society Conference on Computer Vision and Pattern Recognition* (Nov. 2013), pp. 580–587.

[134] Pierre Sermanet, David Eigen, Xiang Zhang, Michael Mathieu, Rob Fergus, and Yann LeCun. "OverFeat: Integrated Recognition, Localization and Detection using Convolutional Networks". In: *2nd International Conference on Learning Representations, ICLR 2014 - Conference Track Proceedings* (Dec. 2013).

[135] Farhana Sultana, Abu Sufian, and Paramartha Dutta. "Evolution of Image Segmentation using Deep Convolutional Neural Network: A Survey". In: *Knowledge-Based Systems* 201–202 (Aug. 2020), p. 106062.

[136] Stéphane Lathuilière, Pablo Mesejo, Xavier Alameda-Pineda, and Radu Horaud. "A Comprehensive Analysis of Deep Regression". In: *IEEE Transactions on Pattern Analysis and Machine Intelligence* 42.9 (2020), pp. 2065–2081.

[137] Tan Le-Dinh, Mohammed Alabdali, Franco M. Zanotto, Hartmut Schlenz, Norbert H. Menzler, Olivier Guillon, and Alejandro A. Franco. "Coarse-grained physics-based modelling for tape casting of fuel-electrode supports in Solid Oxide Cells". In: *Journal of Power Sources* 662 (2026), p. 238655.

[138] Karen Simonyan and Andrew Zisserman. "Very Deep Convolutional Networks for Large-Scale Image Recognition". In: *3rd International Conference on Learning Representations, ICLR 2015 - Conference Track Proceedings* (Sept. 2014).

[139] Martín Abadi, Ashish Agarwal, Paul Barham, Eugene Brevdo, Zhifeng Chen, Craig Citro, Greg S. Corrado, Andy Davis, Jeffrey Dean, Matthieu Devin, Sanjay Ghemawat, Ian Goodfellow, Andrew Harp, Geoffrey Irving, Michael Isard, Yangqing Jia, Rafal Jozefowicz, Lukasz Kaiser, Manjunath Kudlur, Josh Levenberg, Dandelion Mané, Rajat Monga, Sherry Moore, Derek Murray, Chris Olah, Mike Schuster, Jonathon Shlens, Benoit Steiner, Ilya Sutskever, Kunal Talwar, Paul Tucker, Vincent Vanhoucke, Vijay Vasudevan, Fernanda Viégas, Oriol Vinyals, Pete Warden, Martin Wattenberg, Martin Wicke, Yuan Yu, and Xiaoqiang Zheng. *TensorFlow: Large-Scale Machine Learning on Heterogeneous Systems*. Software available from tensorflow.org. 2015.

[140] François Chollet et al. *Keras*. `https://keras.io`. 2015.

[141] Alexander Stukowski. "Visualization and analysis of atomistic simulation data with OVITO–the Open Visualization Tool". In: *Modelling and Simulation in Materials Science and Engineering* 18.1 (2009), p. 015012.

[142] Utkarsh Vijay, Diego E. Galvez-Aranda, Franco M. Zanotto, Tan Le-Dinh, Mohammed Alabdali, Mark Asch, and Alejandro A. Franco. "A hybrid modelling approach coupling physics-based simulation and deep learning for battery electrode manufacturing simulations". In: *Energy Storage Materials* 75 (Feb. 2025), p. 103883.

[143] Utkarsh Vijay, Francisco Fernandez, Siwar Ben Hadj Ali, Mark Asch, and Alejandro A. Franco. "Surrogate Modeling of Lithium-Ion Battery Electrode Manufacturing by Combining Physics-Based Simulation and Deep Learning". In: *Batteries & Supercaps* (2025), e202500433.

[144] Diego E. Galvez-Aranda, Francisco Fernandez, and Alejandro A. Franco. "Physics-Assisted Machine Learning for the Simulation of the Slurry Drying in the Manufacturing Process of Battery Electrodes: A Hybrid Time-Dependent VGG16-DEM Model". In: *ACS Applied Materials & Interfaces* 17 (22 June 2025), pp. 32150–32162.

[145] Siti Khadijah Hubadillah, Mohd Hafiz Dzarfan Othman, Takeshi Matsuura, A. F. Ismail, Mukhlis A. Rahman, Zawati Harun, Juhana Jaafar, and Mikihiro Nomura. "Fabrications and applications of low cost ceramic membrane from kaolin: A comprehensive review". In: *Ceramics International* 44 (5 Apr. 2018), pp. 4538–4560.

[146] Minoo Naebe and Kamyar Shirvanimoghaddam. "Functionally graded materials: A review of fabrication and properties". In: *Applied Materials Today* 5 (Dec. 2016), pp. 223–245.

[147] James E. Smay and Jennifer A. Lewis. "Structural and Property Evolution of Aqueous-Based Lead Zirconate Titanate Tape-Cast Layers". In: *Journal of the American Ceramic Society* 84.11 (2001), pp. 2495–2500.

[148] Y. J. Leng, S. H. Chan, K. A. Khor, and S. P. Jiang. "Performance evaluation of anode-supported solid oxide fuel cells with thin film YSZ electrolyte". In: *International Journal of Hydrogen Energy* 29 (10 Aug. 2004), pp. 1025–1033.

[149] Alfred I.Y. Tok, Freddy Y.C. Boey, and K. A. Khor. "Tape casting of high dielectric ceramic composite substrates for microelectronics application". In: *Journal of Materials Processing Technology* 89-90 (May 1999), pp. 508–512.

[150] A. Tok, F. Boey, and K. Khor. "Tape Casting of High Dielectric Ceramic Substrates for Microelectronics Packaging". In: *Journal of Materials Engineering and Performance* 8 (Aug. 1999), pp. 469–472.

[151] Kaichuang Yang, Jiapeng Liu, Yuhao Wang, Xiangcheng Shi, Jingle Wang, Qiyang Lu, Francesco Ciucci, and Zhibin Yang. "Machine-learning-assisted prediction of long-term performance degradation on solid oxide fuel cell cathodes induced by chromium poisoning". In: *Journal of Materials Chemistry A* 10 (44 Nov. 2022), pp. 23683–23690.

[152] Wenbo Sun, Yujie Zheng, Ke Yang, Qi Zhang, Akeel A. Shah, Zhou Wu, Yuyang Sun, Liang Feng, Dongyang Chen, Zeyun Xiao, Shirong Lu, Yong Li, and Kuan Sun. "Machine learning-assisted molecular design and efficiency prediction for high-performance organic photovoltaic materials". In: *Science Advances* 5.11 (2019), eaay4275.

[153] Xiaoting Zhong, Brian Gallagher, Shusen Liu, Bhavya Kailkhura, Anna Hiszpanski, and T. Yong-Jin Han. "Explainable machine learning in materials science". In: *npj Computational Materials* 8.1 (Sept. 2022).

[154] Jing Wei, Xuan Chu, Xiang-Yu Sun, Kun Xu, Hui-Xiong Deng, Jigen Chen, Zhongming Wei, and Ming Lei. "Machine learning in materials science". In: *InfoMat* 1.3 (2019), pp. 338–358.

[155] Anthony Yu-Tung Wang, Ryan J. Murdock, Steven K. Kauwe, Anton O. Oliynyk, Aleksander Gurlo, Jakoah Brgoch, Kristin A. Persson, and Taylor D. Sparks. "Machine Learning for Materials Scientists: An Introductory Guide toward Best Practices". In: *Chemistry of Materials* 32.12 (2020), pp. 4954–4965.

[156] Md Hosne Mobarak, Mariam Akter Mimona, Md Aminul Islam, Nayem Hossain, Fatema Tuz Zohura, Ibnul Imtiaz, and Md Israfil Hossain Rimon. "Scope of machine learning in materials research—A review". In: *Applied Surface Science Advances* 18 (Dec. 2023), p. 100523.

[157] Pascal Friederich, Florian Häse, Jonny Proppe, and Alán Aspuru-Guzik. "Machine-learned potentials for next-generation matter simulations". In: *Nature Materials 2021 20:6* 20 (6 May 2021), pp. 750–761.

[158] Binh Duong Nguyen, Melissa Roder, Andreas Danilewsky, Johannes Steiner, Peter Wellmann, and Stefan Sandfeld. “Automated analysis of X-ray topography of 4H-SiC wafers: Image analysis, numerical computations, and artificial intelligence approaches for locating and characterizing screw dislocations”. In: *Journal of Materials Research* 38 (Dec. 2022).

[159] Francisco Fernandez, Soorya Saravanan, Rashen Lou Omongos, Javier F. Troncoso, Diego E. Galvez-Aranda, and Alejandro A. Franco. “Transfer learning assessment of small datasets relating manufacturing parameters with electrochemical energy cell component properties”. In: *npj Advanced Manufacturing 2025 2:1* 2 (1 Apr. 2025), pp. 1–14.

[160] Diego E. Galvez-Aranda, Tan Le Dinh, Utkarsh Vijay, Franco M. Zanotto, and Alejandro A. Franco. “Time-Dependent Deep Learning Manufacturing Process Model for Battery Electrode Microstructure Prediction”. In: *Advanced Energy Materials* 14 (15 Apr. 2024), p. 2400376.

[161] G. Pilania, J. E. Gubernatis, and T. Lookman. “Multi-fidelity machine learning models for accurate bandgap predictions of solids”. In: *Computational Materials Science* 129 (Mar. 2017), pp. 156–163.

[162] Olexandr Isayev, Corey Oses, Cormac Toher, Eric Gossett, Stefano Curtarolo, and Alexander Tropsha. “Universal fragment descriptors for predicting properties of inorganic crystals”. In: *Nature Communications* 8.1 (June 2017).

[163] Rafael Gómez-Bombarelli, Jorge Aguilera-Iparraguirre, Timothy D. Hirzel, David Duvenaud, Dougal Maclaurin, Martin A. Blood-Forsythe, Hyun Sik Chae, Markus Einzinger, Dong Gwang Ha, Tony Wu, Georgios Markopoulos, Soonok Jeon, Hosuk Kang, Hiroshi Miyazaki, Masaki Numata, Sunghan Kim, Wenliang Huang, Seong Ik Hong, Marc Baldo, Ryan P. Adams, and Alán Aspuru-Guzik. “Design of efficient molecular organic light-emitting diodes by a high-throughput virtual screening and experimental approach”. In: *Nature Materials 2016 15:10* 15 (10 Aug. 2016), pp. 1120–1127.

[164] Paul Raccuglia, Katherine C. Elbert, Philip D.F. Adler, Casey Falk, Malia B. Wenny, Aurelio Mollo, Matthias Zeller, Sorelle A. Friedler, Joshua Schrier, and Alexander J. Norquist. “Machine-learning-assisted materials discovery using failed experiments”. In: *Nature 2016 533:7601* 533 (7601 May 2016), pp. 73–76.

[165] Nathan J. Szymanski, Bernardus Rendy, Yuxing Fei, Rishi E. Kumar, Tanjin He, David Milsted, Matthew J. McDermott, Max Gallant, Ekin Dogus Cubuk, Amil Merchant, Haegyeom Kim, Anubhav Jain, Christopher J. Bartel, Kristin Persson, Yan Zeng, and Gerbrand Ceder. “An autonomous laboratory for the accelerated synthesis of novel materials”. In: *Nature 2023 624:7990* 624 (7990 Nov. 2023), pp. 86–91.

[166] Hartmut Schlenz, Stefan Baumann, Wilhelm Albert Meulenberg, and Olivier Guillon. “The Development of New Perovskite-Type Oxygen Transport Membranes Using Machine Learning”. In: *Crystals* 12.7 (2022).

[167] Shuaihua Lu, Qionghua Zhou, Yixin Ouyang, Yilv Guo, Qiang Li, and Jinlan Wang. "Accelerated discovery of stable lead-free hybrid organic-inorganic perovskites via machine learning". In: *Nature Communications* 9 (Aug. 2018).

[168] Keith T. Butler, Daniel W. Davies, Hugh Cartwright, Olexandr Isayev, and Aron Walsh. "Machine learning for molecular and materials science". In: *Nature 2018 559:7715* 559 (7715 July 2018), pp. 547–555.

[169] Marc Duquesnoy, Iker Boyano, Larraitz Ganborena, Pablo Cereijo, Elixabete Ayerbe, and Alejandro A. Franco. "Machine learning-based assessment of the impact of the manufacturing process on battery electrode heterogeneity". In: *Energy and AI* 5 (Sept. 2021), p. 100090.

[170] Amina El Malki, Mark Asch, Oier Arcelus, Abbos Shodiev, Jia Yu, and Alejandro A. Franco. "Machine learning for optimal electrode wettability in lithium ion batteries". In: *Journal of Power Sources Advances* 20 (Mar. 2023), p. 100114.

[171] Amina El Malki, Mohamed Ati, Mark Asch, and Alejandro A. Franco. "A machine learning tool to investigate lithium-ion battery degradation under real automotive conditions". In: *Journal of Power Sources* 630 (Feb. 2025), p. 236048.

[172] Rashen Lou Omongos, Diego E. Galvez-Aranda, Francisco Fernandez, András Vernes, and Alejandro A. Franco. "Digital correlation analysis and optimization of microporous layer through a machine learning workflow for PEMFC applications". In: *Journal of Power Sources* 652 (Oct. 2025), p. 237522.

[173] Rashen Lou Omongos, Diego E. Galvez-Aranda, Franco M. Zanotto, András Vernes, and Alejandro A. Franco. "Machine learning-driven optimization of gas diffusion layer microstructure for PEM fuel cells". In: *Journal of Power Sources* 625 (Jan. 2025), p. 235583.

[174] Nicolas CARPi, Alexander Minges, and Matthieu Piel. "eLabFTW: An open source laboratory notebook for research labs". In: *Journal of Open Source Software* 2.12 (2017), p. 146.

[175] Raghul Parthipan, Mohit Anand, Hannah M. Christensen, J. Scott Hosking, and Damon J. Wischik. "Defining error accumulation in ML atmospheric simulators". In: (May 2024).

[176] Samiyuru Menik and Lakshmish Ramaswamy. "Towards Modular Machine Learning Solution Development: Benefits and Trade-offs". In: (Jan. 2023).

[177] Robert V. Hogg, Joseph W. McKean, and Allen T. Craig. *Introduction to mathematical statistics*. eng. 6th ed. Upper Saddle River, N.J: Pearson Prentice Hall, 2005.

[178] Bora Timurkutluk, Selahattin Celik, and Emre Ucar. "Influence of doctor blade gap on the properties of tape cast NiO/YSZ anode supports for solid oxide fuel cells". In: *Ceramics International* 45 (3 Feb. 2019), pp. 3192–3198.

[179] C. A. Gutiérrez and R. Moreno. "Tape casting of non-aqueous silicon nitride slips". In: *Journal of the European Ceramic Society* 20 (10 Sept. 2000), pp. 1527–1537.

[180] Rangarajan Pitchumani and Vistasp M. Karbhari. "Generalized Fluid Flow Model for Ceramic Tape Casting". In: *Journal of the American Ceramic Society* 78 (9 Sept. 1995), pp. 2497–2503.

[181] Shovan Chowdhury, Yuxiao Lin, Boryann Liaw, and Leslie Kerby. "Evaluation of Tree Based Regression over Multiple Linear Regression for Non-normally Distributed Data in Battery Performance". In: *2022 International Conference on Intelligent Data Science Technologies and Applications, IDSTA 2022* (2022), pp. 17–25.

[182] *Importance of Feature Scaling*. `https://scikit-learn.org/stable/auto_examples/preprocessing/plot_scaling_importance.html`. Accessed March 13, 2026.

[183] Aurelien Geron. *Hands-On Machine Learning with Scikit-Learn, Keras, and TensorFlow: Concepts, Tools, and Techniques to Build Intelligent Systems*. 2nd. O'Reilly Media, Inc., 2019.

[184] Ke Xu, Yingguang Li, Changqing Liu, Xu Liu, Xiaozhong Hao, James Gao, and Paul G. Maropoulos. "Advanced Data Collection and Analysis in Data-Driven Manufacturing Process". In: *Chinese Journal of Mechanical Engineering 2020 33:1* 33 (1 May 2020), pp. 1–21.

[185] Patrik Zajec, Jože Martin Rožanec, Inna Novalija, Blaž Fortuna, Dunja Mladenić, and Klemen Kenda. "Towards Active Learning Based Smart Assistant for Manufacturing". In: *IFIP Advances in Information and Communication Technology* 633 IFIP (Mar. 2021), pp. 295–302.

[186] Jože M. Rožanec, Inna Novalija, Patrik Zajec, Klemen Kenda, and Dunja Mladenić. "Knowledge Modelling and Active Learning in Manufacturing". In: *Trusted Artificial Intelligence in Manufacturing: A Review of the Emerging Wave of Ethical and Human Centric AI Technologies for Smart Production* (July 2021), pp. 52–72.

[187] Thanasis Kotsiopoulos, Panagiotis Sarigiannidis, Dimosthenis Ioannidis, and Dimitrios Tzovaras. "Machine Learning and Deep Learning in smart manufacturing: The Smart Grid paradigm". In: *Computer Science Review* 40 (May 2021), p. 100341.

[188] Heiner Lasi, Peter Fettke, Hans Georg Kemper, Thomas Feld, and Michael Hoffmann. "Industry 4.0". In: *Business and Information Systems Engineering* 6 (4 Aug. 2014), pp. 239–242.

[189] Mariia Golovianko, Vagan Terziyan, Vladyslav Branytskyi, and Diana Malyk. "Industry 4.0 vs. Industry 5.0: Co-existence, Transition, or a Hybrid". In: *Procedia Computer Science* 217 (Jan. 2023), pp. 102–113.

[190] Praveen Kumar Reddy Maddikunta, Quoc Viet Pham, Prabadevi B, N. Deepa, Kapal Dev, Thippa Reddy Gadekallu, Rukhsana Ruby, and Madhusanka Liyanage. "Industry 5.0: A survey on enabling technologies and potential applications". In: *Journal of Industrial Information Integration* 26 (Mar. 2022), p. 100257.

Band / Volume 692
Entwicklung von Reparaturmethoden für einkristalline Bauteile mittels thermischer Spritzverfahren
M. L. Létang (2026), X, 211 pp
ISBN: 978-3-95806-883-4

Band / Volume 693
Assessing the Environmental Implications of Offshore Wind Energy Advancements on the Future German Electricity Sector
A. Benitez (2026), xi, 176 pp
ISBN: 978-3-95806-885-8

Band / Volume 694
Entwicklung von Korrosionsschutzschichten für Protonen-Austausch-Membran-Wasserelektrolyseure
T. Sievert (2026), 201 pp
ISBN: 978-3-95806-888-9

Band / Volume 695
Hierarchical Modeling of Electrocatalytic Reactions from a Local Perspective
X. Zhu (2026), ix, 121 pp
ISBN: 978-3-95806-889-6

Band / Volume 696
Nanocrystalline Silicon Carbide in Transparent Passivating Contact Solar Cells
A. Eberst (2026), xiii, 225 pp
ISBN: 978-3-95806-891-9

Band / Volume 697
Theory of Electronic and Ionic Perturbations at Supported Electrocatalyst Nanoparticles
Y. Zhang (2026), XI, 131 pp
ISBN: 978-3-95806-896-4

Band / Volume 698
Aufbau und Einsatz eines on-board Messsystems zur Untersuchung der Abgaszusammensetzung von Fahrzeugen betrieben mit konventionellen und alternativen Kraftstoffen
V. Polinowski (2026), VIII, 269 pp
ISBN: 978-3-95806-897-1

Band / Volume 699
Ab Initio-based large-scale Atomistic Simulations of Cathode Materials for Secondary Batteries: From Computational Methodologies to Applications towards improved Structural and Chemical Stability
K. Köster (2026), x, 204, x pp
ISBN: 978-3-95806-898-8

Band / Volume 700
Materials Design, Processing and Application of Proton-Conducting Oxides for Electrochemical Energy Conversion
Y. Zeng (2026), vii, 117 pp
ISBN: 978-3-95806-899-5

Band / Volume 701
Accelerating the discovery of alkaline-stable anion exchange membrane materials via computational exploration
F. P. Tipp (2026), xii, 135 pp
ISBN: 978-3-95806-900-8

Band / Volume 702
Methods for Investigating the Structure-Performance Correlation in Membrane Electrode Assemblies
N. Utsch (2026), XIII, 138, LXVII pp
ISBN: 978-3-95806-901-5

Band / Volume 703
Hot-Spot Formation in Cu(In,Ga)Se_2 Thin Film Solar Cells
S. Nofal (2026), xvii, 131 pp
ISBN: 978-3-95806-903-9

Band / Volume 704
Machine Learning Guidance of Manufacturing Process of Solid Oxide Cells
T. LE DINH (2026), xxi, 122 pp
ISBN: 978-3-95806-904-6

Energie & Umwelt / Energy & Environment
Band / Volume 704
ISBN 978-3-95806-904-6

Mitglied der Helmholtz-Gemeinschaft

JÜLICH
Forschungszentrum